

Fracture mechanism of an aluminium cast alloy locally reinforced by SiC particles and Al₂O₃ whiskers under monotonic and cyclic load: boundary and whisker orientation effect.

(一部分が SiC 粒子と Al₂O₃ ウィスカーで強化された Al 鋳造合金の単調および繰返し荷重下における破壊機構の評価:境界およびウィスカー方位の効果)

2008年3月

埼玉大学大学院理工学研究科 (博士後期課程)

生産科学専攻(主指導教員 荒居 善雄)

RAFIQUZZAMAN MD.

Fracture mechanism of an aluminium cast alloy locally
reinforced by SiC particles and Al₂O₃ whiskers under
monotonic and cyclic load: boundary and whisker
orientation effect.

A Dissertation submitted to the Saitama University in partial
fulfillment of the requirements for the degree of Doctor of
Philosophy
In
Production Science

By
Rafiquzzaman MD.

Examining Committee:

Prof. Yoshio ARAI
Prof. Hiroshi KATO
Prof. Kenichiro HORIO
Prof. Kensuke KAGEYAMA

Doctor Course in Production Science
Graduate School of Science and Engineering
Saitama University
Japan

March 2008

TABLE OF CONTENTS

ABSTRACT	i
ACONOWLEDGEMENTS	iv
List of Figures	vii
List of Tables	xv
List of Symbols	xvii
Chapter 1 Introduction.....	1
1.1 Background.....	1
1.2 Application of MMCs.....	3
1.3 Concept of locally reinforced material	5
1.4 Literature review	8
1.5 Scope and objectives	14
1.6 Outline of present research.....	15
References	17
Chapter 2: Materials and Experimental Procedures.....	23
2.1 Materials fabrication	23
2.2 Materials preparation.....	25
2.3 Microstructural features	25
2.4 Experimental setup and procedures	30
References	33
Chapter 3: Experimental Results	34
3.1 Introduction	34
3.2 Boundary effect on fracture mechanism under monotonic loading	35

3.3 Boundary effect on fracture mechanism under cyclic loading	40
3.4 Whisker orientation effect on monotonic and fatigue strength	45
3.5 Summary.....	53
References	56

Chapter 4 Numerical Study of Fracture Mechanism, Boundary effect and Whisker Orientation Effect.....57

4.1 Introduction	57
4.2 Numerical model	60
4.3. Prediction of stress distributions and fracture mechanism.....	72
4.4. Prediction of whisker orientation effect on strength.....	81
4.5 Summary.....	86
References	87

Chapter 5 Conclusion.....90

5.1 General conclusions.....	90
------------------------------	----

APPENDIX

Appendix I	93
Appendix II.....	94
Appendix III.....	95
Appendix IV.....	98
Appendix V	101
Appendix VI.....	103
Appendix VII.....	105
References.....	117

ABSTRACT

This dissertation presents the research work done for the degree of Doctor of philosophy. The research project is on Fracture mechanism of an aluminium cast alloy locally reinforced by SiC particles and Al₂O₃ whiskers under monotonic and cyclic load: boundary and whisker orientation effect.

Metal matrix composites (MMCs) have been widely considered as possible substitute of traditional materials (such as metals, plastics, ceramics etc.) for structural applications because of their high strength and stiffness, low density, high temperature properties and excellent wear resistance. These advantages made this material more and more potential and alternative in the engineering application. However, the high productive cost, poor ductility and low fracture toughness of MMCs are the major barriers for their structural application.

In this dissertation, fracture mechanisms and corresponding stress distributions in an aluminium cast alloy locally reinforced by SiC particles and Al₂O₃ whiskers, under monotonic and cyclic load, are investigated experimentally and numerically. The effect of whisker orientation on monotonic and fatigue strength has also been investigated. The material is monotonically and cyclically deformed to failure at room temperature. The fracture origin and the fracture path are investigated on the fracture surfaces. The stress distributions around the boundary between the reinforced part and the unreinforced part are calculated based on an inclusion array model considering the microscopic inhomogeneous effects. A three-dimensional single whisker unit cell model of cylindrical shape whisker in the periodic boundary condition is conducted using finite element method (FEM) to describe the overall behavior of the composite

Chapter 1 is an introduction of the research, which describes the back ground, the

motivation, proposed concepts, the objectives and the scopes of this research. In this chapter also reviews the past research on the MMC.

In chapter 2, Materials fabrication and its microstructure, the experimental set up and the experimental procedures are discussed. Materials are successfully fabricated by squeeze casting method. The polishing surface observations are treated by optical microscope and the fracture surface observations are treated by the scanning electron microscope (SEM) and energy dispersive X-ray (EDX) analysis.

In chapter 3, the experimental results are discussed, which describes the fracture mechanisms, boundary effect and whisker orientation effect. The fracture origin and fracture path are investigated by SEM on the fracture surfaces. The fracture occurs in the reinforced part under both monotonic and cyclic loads. SEM analysis of the fracture surfaces shows that the fatigue fracture is controlled by the fracture of coarse Al_2O_3 whiskers. The static fracture (monotonic loading) shows that the fracture mechanism is the combination of reinforcing particle fracture and interfacial debonding between reinforcing ceramics and matrix metal. A significant effect of reinforcement orientation on the monotonic strength and fatigue strength are observed experimentally and numerically. With respect to the stress direction the whisker orientation gives significant difference in strength of this material. SEM analysis shows almost all whiskers are transversely debonded when whisker direction is perpendicular to the stress direction and almost all whiskers are broken when the whisker direction is random to the stress direction.

In chapter 4, a numerical analysis is discussed. The stress distributions around the boundary between reinforced part and unreinforced part are calculated based on an inclusion array model considering the microscopic inhomogeneous effects. A

three-dimensional single whisker unit cell model of cylindrical shape whisker in the periodic boundary condition is conducted using FEM to describe the overall behavior of the composite. The prediction results based on FEM analysis are found to be in reasonable agreement with the experimental observations.

In chapter 5, the general conclusions and directions for future investigation are given.

ACKNOWLEDGEMENTS

All the credits, for which the dissertation put forward for submission, are due to my supervisor Prof. Yoshio ARAI. I, therefore, sincerely express my cordial sense of gratitude to him for his cooperative and constructive suggestions throughout the period of this research work. His intelligent supervision with continuous and overflowing enthusiasm, unrelenting efforts, great patience and invaluable inputs helped me to put the research ideas in the form that this dissertation presents. His insightful meticulous and persistent supervision helps me complete the work successfully.

I would like to express my sincere thanks and gratitude to Prof. Eiichiro TSUCHIDA, the emeritus professor of Saitama University, Japan for his valuable suggestion, constructive criticism and continuous encouragement throughout the period of this research work.

It is certainly a great pleasure for me as well to express my profound gratitude to my dissertation committee members, Prof. Hiroshi KATO, Prof. Kenichiro HORIO and Prof. Kensuke KAGEYAMA for graciously agreeing to review this dissertation, and their helpful comments.

My special appreciation is extended to Mr. Tatsuo Tamagawa and Mr. Toyomi Uchiyama and for their help during the study. Sincere thanks to all the members of strength of materials laboratory, with whom I spent a colorful life in Japan.

I also gratefully acknowledge the scholarship during the study from the Ministry of

Education, Science, Sports and Culture, Government of Japan.

Finally, the patience, adoration, sympathy and empathy extend to me by my family members including my parents, my beloved wife Monima Alam and beloved brother MD. Shafiquzzaman were also a source of inspiration for completing the dissertation in final form.

Dedicated to

Late MD. MOZAMMEL HAQUE

&

MS. NURJAHAN BEGUM

My beloved parents whose inspiration boosted me up to a position I am here now

List of Figures

No.	Captions	Page
Fig.1.1	Brake disc structure.	6
Fig.1.2	Example illustration of application of locally reinforced material.	7
Fig. 2.1	Squeeze casting method.	24
Fig. 2.2	Specimen cut out from a disc (unit: mm).	26
Fig. 2.3	Optical micrograph of the composite on the tensile side face, representing the SiC particle and Al ₂ O ₃ whisker distribution and Al ₂ O ₃ whisker orientation angle: (a) and (b) Locally reinforced material ($\alpha = 90^\circ$) and (c) Homogeneous MMC ($\alpha = 0^\circ \sim 90^\circ$) (d) Definition of whisker orientation angle α .	27
Fig. 2.4	Optical micrograph of the composite on the tensile side face, representing the coarse Al ₂ O ₃ whiskers which were formed during the materials fabrication.	28
Fig. 2.5	Measurement of inter particle/whisker distance with respect to the boundary between reinforced and unreinforced part.	28
Fig. 2.6	Inter particle/whisker distance with respect to the boundary (a) particle to particle (b) whisker to whisker (c) particle to whisker.	29
Fig. 2.7	Experimental setup.	31
Fig. 2.8	Schematic illustration of four-point bending test.	32

Fig. 3.1	Nominal bending stress versus deflection curves under monotonic loading of locally reinforced material ($\alpha = 90^\circ$).	36
Fig. 3.2	Matching surface view of fractured specimen ($\alpha = 90^\circ$) under monotonic loading, $\sigma_f = 272$ MPa.	38
Fig.3.3	Matching surface view of fractured specimen ($\alpha = 90^\circ$) under monotonic loading, $\sigma_f = 318$ MPa.	38
Fig 3.4	Matching fracture surface of locally reinforced material ($\alpha = 90^\circ$) under monotonic loading, $\sigma_f = 272$ MPa.	39
Fig.3.5	Stress versus fatigue life behavior locally reinforced material ($\alpha = 90^\circ$) (stress ratio, $R = 0.1$).	42
Fig. 3.6	Matching surface view of fatigue fractured specimen under cyclic loading, maximum stress $\sigma_{\max} = 156$ MPa, $N_f = 5.73 \times 10^5$.	43
Fig. 3.7	Matching fracture surface after fatigue fracture, maximum stress $\sigma_{\max} = 156$ MPa, $N_f = 5.73 \times 10^5$.	43
Fig. 3.8	Matching surface view of fatigue fractured specimen under cyclic loading, maximum stress $\sigma_{\max} = 156$ MPa, $N_f = 716$.	44
Fig.3.9	Matching fracture surface after fatigue fracture, maximum stress $\sigma_{\max} = 156$ MPa, $N_f = 716$.	44

Fig. 3.10	Nominal bending stress versus deflection curves under monotonic loading.	47
Fig. 3.11	Stress versus fatigue life behavior (stress ratio, $R=0.1$), the plots on $N_f = 0$ show average strength under monotonic load.	48
Fig. 3.12	Comparison of two types of fracture surface (a) locally reinforced material ($\alpha = 90^\circ$) [CTP5] (b) Homogeneous MMC ($\alpha = 0^\circ \sim 90^\circ$) [HCTP4], under cyclic loading condition (Observed locations are near the tensile side).	50
Fig. 3.13	Comparison of two types of fracture surface (a) locally reinforced material ($\alpha = 90^\circ$) [TP1] (b) Homogeneous MMC ($\alpha = 0^\circ \sim 90^\circ$) [HTP1]; under monotonic loading condition (Observed locations are near the tensile side).	50
Fig. 3.14	Matching fatigue fracture surface of homogeneous MMC ($\alpha = 0^\circ \sim 90^\circ$) after fatigue fracture $\sigma_{\max} = 191 \text{ MPa}$, $N_f = 6.67 \times 10^4$.	53
Fig. 4.1	Global model of homogeneous materials joint (a) model illustration (b) finite-element mesh.	62
Fig. 4.2	Infinite periodic unit cell model.	63
Fig. 4.3	Inclusion array model (a) model illustration (b) finite-element mesh.	64
Fig. 4.4	Illustration of loading and unloading process during fatigue analysis.	65
Fig. 4.5	Fig.4.5 3-D single whisker model representing the whisker reinforced Al alloy (a) and (b) schematic illustration of the	67

periodic fiber arrangement (c) finite-element mesh.

- Fig. 4.6 Fig.4.6 3-D hybrid model representing the whisker/particle reinforced Al alloy (a) schematic illustration of the periodic whisker and particle arrangement (b) 1/8 model analyzed based on symmetry and (c) finite element mesh (9 Vol.% Alumina whisker and 21 Vol.% SiC particle) (Model-2, Model-3) 69
- Fig.4.7 3-D hybrid model representing the whisker/particle reinforced Al alloy (a) schematic illustration of the periodic whisker and particle arrangement (b) 1/8 model analyzed based on symmetry and (c) finite element mesh (9 Vol.% Alumina whisker and 21 Vol.% SiC particle) (Model-4, Model-5). 70
- Fig. 4.8 Stress distribution along y direction of global model of homogeneous joint. 72
- Fig. 4.9 Stress distributions along y direction of inclusion array model under nominal bending stress (a) 300 MPa (b) 156 MPa. 73
- Fig. 4.10 Stress distributions along y direction of inclusion array model under nominal bending stress 300 MPa. 74
- Fig. 4.11 Stress distributions along y direction of inclusion array model under nominal bending stress 300 MPa. 76
- Fig. 4.12 Stress distributions along y direction of inclusion array model under nominal bending stress 156 MPa. 77

Fig. 4.13	Distributions of total strain in matrix along normal to the boundary of inclusion array model under cyclic loading at maximum stress 156 MPa.	78
Fig. 4.14	Equivalent plastic strain distribution along y direction of inclusion array model under nominal bending stress 300 MPa.	79
Fig. 4.15	Equivalent plastic strain distribution along y direction of inclusion array model under nominal bending stress 156 MPa.	80
Fig. 4.15	Stress distribution along z direction for longitudinal loading (parallel to the stress direction).	79
Fig. 4.16	Compares the stress distribution and magnitude of σ_{zz} along z direction of whisker composite and hybrid composite.	82
Fig. 4.17	Compares the stress distribution and magnitude of σ_{yy} along z direction of whisker composite and hybrid composite.	83
Fig. 4.18	Predicted stress calculated from different nominal stress.	84
Fig. A1-1	Microscopic photograph of locally reinforced material ($\alpha = 90^\circ$) representing the coarse Al_2O_3 whisker (a) Before bending test (b) After bending test.	93
Fig. A1-2	Microscopic photograph of locally reinforced material ($\alpha = 90^\circ$) representing the coarse Al_2O_3 whisker (a) Before	93

	bending test (b) After bending test.	
Fig. A2-1	Fracture path of locally reinforced material ($\alpha = 90^\circ$) under monotonic loading.	94
Fig. A2-2	Fracture path of homogeneous MMC ($\alpha = 0^\circ \sim 90^\circ$) under monotonic loading.	94
Fig. A3-1	Sample configuration of locally reinforced material ($\alpha = 90^\circ$) (boundary location at the center between reinforced and unreinforced part) (unit: mm).	95
Fig. A3-2	Sample configuration of locally reinforced material ($\alpha = 90^\circ$) (boundary location not at the center between reinforced and unreinforced part) (unit: mm).	95
Fig. A3-3	Nominal bending stress versus deflection curves under monotonic loading (boundary location effect on strength).	96
Fig. A3-4	Stress versus fatigue life behavior (stress ratio, $R=0.1$) (boundary location effect on fatigue strength).	97
Fig. A3-5	Matching fatigue fracture surface of homogeneous MMC ($\alpha = 0^\circ \sim 90^\circ$) after fatigue fracture $\sigma_{\max} = 191 \text{ MPa}$, $N_f = 5.6 \times 10^5$.	98
Fig. A4-1	Inclusion array model illustration to evaluate average elastic constant for homogeneous material joint model.	99
Fig. A4-2	Stress distribution along y direction of inclusion array model.	100
Fig. A5-1	Schematic description of moiré interferometry	101
Fig. A5-2	Comparison results of experimental (moiré interferometry)	102

and numerical displacement fields.

Fig.A6-1	Stress distribution along y direction of inclusion array model for two meshing system.	103
Fig. A6-2	Stress distribution around the boundary of homogeneous material joint model and inclusion array model under nominal bending stress (a) 300 MPa (b) 156 MPa.	104
Fig. A7-1	3-D single whisker model representing the whisker reinforced Al alloy (a) schematic illustration of the periodic fiber arrangement (b) 1/8 model analyzed based on symmetry and (c) finite-element mesh.	107
Fig. A 7-2	3-D single whisker model representing the hybrid whisker/particle reinforced Al alloy (a) schematic illustration of the periodic fiber and particle arrangement (b) 1/8 model analyzed based on symmetry and (c) finite-element mesh.	109
Fig. A7-3	Stress distribution along z direction for longitudinal loading (parallel to the stress direction).	111
Fig. A7-4	Stress distribution along z direction for transverse loading (perpendicular to the stress direction).	112
Fig. A7-5	Stress distribution along z direction for longitudinal loading (parallel to the stress direction).	114

Fig. A7-6	Stress distribution along z direction for transverse loading (perpendicular to the stress direction).	115
Fig. A7-7	Stress distribution along z direction for transverse loading (perpendicular to the stress direction).	116

List of Tables

No.	Captions	Page
Table 1	Chemical compositions of AC4CH alloy (wt. %).	24
Table 2	Volume fraction and mechanical properties.	24
Table 3	Fracture stresses and minimum distance from the fracture location to macroscopic boundary between reinforced part and unreinforced part under monotonic loading of locally reinforced material ($\alpha = 90^\circ$).	36
Table 4	Area fractions of SiC particle and Al ₂ O ₃ whisker fracture and interface debonding between SiC particle-matrix and Al ₂ O ₃ whisker-matrix under monotonic and cyclic loading condition.	37
Table 5	Fatigue life and distance from fatigue fracture location to macroscopic boundary of locally reinforced material ($\alpha = 90^\circ$).	41
Table 6	Fracture stresses under monotonic loading of homogeneous MMC ($\alpha = 0^\circ \sim 90^\circ$).	46
Table 7	Fatigue life of homogeneous MMC ($\alpha = 0^\circ \sim 90^\circ$).	47
Table 8	Area fractions of SiC particle and Al ₂ O ₃ whisker fracture and interface debonding between SiC particle-matrix and Al ₂ O ₃ whisker-matrix under cyclic loading conditions.	50
Table 9	Area fractions of SiC particle and Al ₂ O ₃ whisker fracture and interface debonding between SiC particle-matrix and	51

Al_2O_3 whisker-matrix under monotonic loading
conditions.

Table 10	Mechanical properties of materials.	60
Table 11	Flow stresses predicted by the model.	61
Table 12	Geometry of numerical model (unit: mm).	62
Table 13	Model chart	71
Table A4-1	Elastic constant predicted by inclusion array model.	97

List of Symbols

Symbol	Definition
α	Whisker orientation angle with respect to the externally applied stress direction
σ_b	Bending stress
N_f	Fatigue life
P	Load
d_f	Minimum distance from boundary to fracture site
σ_f	Fracture stress
σ_{\max}	Maximum stress
ε_p	Plastic strain
ε_y	Total normal strain along y direction
$\Delta\varepsilon_y$	Strain amplitude
E	Young's modulus
E_i	Young's modulus of material i
u_i	Displacement component
σ_y	Normal stress along y direction
σ_z	Normal stress along z direction

List of Publications

Reviewed journal paper:

1. **Rafiquzzaman MD.**, Yoshio ARAI “Fracture mechanisms under monotonic and cyclic load of aluminium cast alloy locally reinforced by SiC particles and Al₂O₃ whiskers”, *Materials Science and Technology* (Accepted, July 18th, 2007).
2. **Rafiquzzaman MD.**, Yoshio ARAI, Eiichiro TSUCHIDA “一部分が SiC 粒子と Al₂O₃ ウィスカで強化された Al 鋳造合金の強度評価とフラクトグラフィ (Strength Evaluation of Aluminium Cast Alloy Locally Reinforced by SiC Particles and Al₂O₃ whiskers and Its Fractography)”, *Japan Society of Material Science, 材料*, Vol. 56, No. 11, pp. 1016-1021, 2007.
3. **Rafiquzzaman MD.**, Yoshio ARAI. “Effect of Whisker Orientation on Monotonic and Fatigue Strength of Aluminium Cast Alloy Locally Reinforced by SiC Particles and Al₂O₃ Whiskers under Monotonic and Cyclic load” *Journal of Solid Mechanics and Materials Engineering, JSME*, Vol.2, No. 1, pp 47-57,2008.

Conference presentation:

1. **Rafiquzzaman MD.**, Yoshio ARAI “一部分が SiC 粒子と Al₂O₃ ウィスカで強化された Al 鋳造合金の単調および繰返し荷重下における破壊機構の評価 (Fracture mechanism under monotonic and cyclic load of aluminium cast alloy locally reinforced by SiC particles and Al₂O₃ whiskers)” *Mechanical Engineering Congress, 2007 Japan (MECJ-07)*, No.07-1, Vol. 6, pp. 197-19, 2007.
2. **Rafiquzzaman MD.**, Yoshio ARAI, Eiichiro TSUCHIDA, Atsushi SUZUKI, Seiya MURAYAMA., “Evaluation of stress fields around macroscopic interface edge of a metal locally reinforced by ceramic particles”. (局所的にセラミック粒子で強化された金属の巨視的界面端部応力場の評価,) *日本機械学会 M&M2006 講演論*

文集, No. 06-4, pp. 515 - 516 (2006 8).

3. **Rafiquzzaman MD.**, Yoshio ARAI, Eiichiro TSUCHIDA, atsushi SUZUKI. Seiya MURAYAMA. , “Effect of Stress Field around interface Edge on Fatigue Strength of Aluminium Cast Alloy Locally Reinforced by SiC and Al₂O₃” (局所的にセラミック粒子で強化された金属の疲労強度に及ぼす端部応力場の影響)、Mechanical Engineering Congress, 2006 Japan (MECJ-06), 日本機械学会 2006 年度年次大会講演論文集, No. 06-1, Vol. 6, pp. 547 - 548 (2006 9).
4. **Riquzzaman MD.**, Yoshio ARAI, Eiichiro TSUCHIDA, atsushi SUZUKI. Seiya MURAYAMA. , “SiC/Al₂O₃ハイブリッドMMC/Al 鑄造合金接合部の強度評価とフラクトグラフィ.” 日本材料学会第 11 回フラクトグラフィシンポジウム前刷集, pp. 43 - 47 (2006 11).
5. **Rafiquzzaman MD.**, 荒居善雄, 土田栄一郎, 村山誠哉,局所的にセラミック粒子で強化された金属の巨視的界面端部応力場の評価,日本機械学会 M&M2006 講演論文集, No. 06-4, pp. 515 - 516 (2006 8).
6. **Rafiquzzaman Md.**, 荒居善雄, 土田栄一郎, 鈴木敦志, 村山誠哉,SiC/Al₂O₃ハイブリッド MMC/Al 鑄造合金接合部の応力解析と強度評価,日本機械学会 第 1 回埼玉ブロック大会(講演会)講演論文集, No. 050-5, pp. 107 - 108 (2005 11).
7. **Rafiquzzaman MD.**, Yoshio ARAI, Eiichiro TSUCHIDA, atsushi SUZUKI. Seiya MURAYAMA. , “Strength evaluation of aluminium cast alloy locally reinforced by SiCp/Al₂O₃ Hybrid MMC.” Mechanical Engineering Congress, 2005 Japan (MECJ-05), Vol.1, No. 05-1, pp. 261-262, 2005.
8. Yoshio ARAI, Eiichiro TSUCHIDA, **Rafiquzzaman MD.** Seiya MURAYAMA. , “Evaluation of fracture mechanism of aluminium cast alloy locally reinforced by SiCp/ Al₂O₃ Hybrid MMC.” Mechanical Engineering Congress, 2004 Japan (MECJ-04), Vol.1, No. 04-1, pp. 361-362, 2004.

Chapter 1: Introduction

1.1 Background

The mechanical components made by traditional materials (e.g. metals, plastics and ceramics) do not always give all the properties they require under their service conditions. In this way, different industries, such as the automotive and railway ones, are looking for low cost methods to improve the final performance of components made of steel, cast iron or even conventional aluminum alloys (e.g. for components such as automotive pistons, brakes, brake drums, brake discs). In order to obtain more efficient product for structural application, it is necessary to improve wear and fatigue behavior, weight reduction, high thermal conductivity, low coefficient of thermal expansion of the materials. Therefore, metal matrix composites (MMCs) have been widely considered as possible substitute which could comply with those characteristics.

MMCs consist of at least two chemically and physically distinct phases, e.g. a fibrous or particulate phase, distributed in a metallic matrix. For three decades, metal matrix composite materials have been popular subjects of applied engineering research [1, 2]. Recently MMCs have become attractive materials for structural applications such as aerospace, automotive industry and wear applications, especially in the frictional area of braking systems because of their great advantages and mechanical performance. The major advantages of MMCs compared to unreinforced material are as follows:

- Greater strength
- Improved stiffness
- Reduced density (weight)

- Improved high temperature properties
- Controlled thermal expansion coefficient
- Improved abrasion and wear resistance
- Improved damping capabilities

The above advantages made this material (MMCs) more and more attractive and alternative in the engineering applications. Despite their great advantages, the high productive cost, poor ductility and low fracture toughness of MMCs are the major barriers for their structural applications. For minimizing these limitations, a clear understanding of the micromechanisms of damage characteristics of MMCs is necessary to design the microstructure of these materials. During past few decades many researchers have investigated such kind of research [1-42]. Strength and stiffness are the two most important characteristics for structural applications. Fracture properties, such as ductility, toughness and fatigue response, are often of primary importance for structural applications.

Consideration of type and contribution of reinforcement component MMCs can be classified as

1. Particle reinforced MMCs.
2. Short fiber/whisker reinforced MMCs
3. Continuous fiber/whisker reinforced MMCs .
4. Laminated or layered MMCs.

The reinforcement and the matrix system for the MMCs are mainly determined by the intended application of the composites. For example, the MMCs used in the frictional area e.g. brake rotor, there is needed the high thermal conductivity with improved

ductility therefore ceramics and high toughness aluminum should be chosen. By using hybrid techniques, the combined application of two or more reinforcements is possible. Fabrication step of the composite is an important part to minimize their limitation (high cost, low toughness) in the structural applications. Metal matrix composite materials can be manufactured by many different techniques [1, 2]. The fabrication techniques divided into two categories: (1) solid state includes powder metallurgy and diffusion bonding and (2) liquid state includes infiltration, dispersion and spraying. MMCs of commercial applications are now produced by the liquid state process because of the following advantages over the solid state process;

- Less expensive
- Liquid metal is easier to handle than are powders
- Complex shape can be produced by liquid state process

Among the various types of the liquid state fabrication techniques, squeeze casting have now become one of the most feasible techniques for the production of low cost MMCs and complex shape components [2]. Additionally, compared to other casting method e.g. gravity or die casting, a wide range of alloy can be cast using squeeze casting. Preparation of the whisker/particle preform is an important step in the fabrication of MMCs by squeeze casting method. Reinforcement breakage, porosity, inhomogeneous reinforcement orientation, bad interfacial bonding in the composites is the barrier to obtain adequate strength and mechanical properties of MMCs.

1.2 Application of MMCs

In the past 15- 20 years, MMCs have emerged as a class of materials capable of advanced structural, aerospace, automotive and wear applications. These alternative

materials (substitute of conventional materials) provide the specific mechanical properties necessary for elevated and ambient temperature applications. Up to now the major applications served by the MMCs in the automotive industries include selectively or partially reinforced pistons for diesel engine, selectively reinforced cylinder bores in Al engine blocks, intake and exhaust valves, driveshafts and propshafts, brake components (discs, rotors and calipers) and power module components for hybrid and electric cars. The first major MMC application in the commercial automotive market was a selectively reinforced piston produced for a diesel engine in 1983[1]. The success of this application was followed by the use of selectively reinforced engine cylinder bores in 1990. Reduction of overall vehicle weight is important for improving fuel economy. Therefore, the application of MMCs for disc brake rotor has been receiving considerable world wide attention. A brake rotor weight saving approximately 52% may be possible if MMCs can be substituted for the cast iron [5]. The high thermal conductivity of aluminum reinforced with SiC provides additional advantages for the thermal management of brake system. Metal matrix composites are finding a wide range of applications in aerospace. Aeronautical MMC applications have been established in the aero structural, aero propulsion, and subsystem categories. Aero structural components include ventral fins, fuel access door covers and rotor blade sleeves. Also few MMC applications have been established in the space systems. Particulate reinforced are in use as recreational products including golf club shafts and heads, skating shoes, base ball shafts and bicycle frames. They are also in use as microprocessor lids and integrated heat sinks in electronic packaging.

1.3 Concept of locally reinforced material

Due to excellent mechanical performances (higher thermal properties, great strength and stiffness) and considerable weight reduction, SiC particulates aluminum based MMCs was capable of being used an axle mounted brake discs in automotive industry [5]. Despite their great advantages, lower ductility and higher cost is the major limitation of this composite. Therefore, there is a critical need to develop and design a new idea and concept in this material for structural applications. The use of the combine advantages of brittle MMCs and a ductile carrier body can be promising alternative [5]. The ductile matrix material (e.g. Al, Mg etc.) partially or locally reinforced by brittle particles or whiskers is called locally or partially reinforced material. The application of reinforced part of this material to the most important functional area of the mechanical component especially which are the frictional surfaces may reduce the cost and improve the mechanical performances. For example, in the brake disc application, ductile aluminium alloy which has high fracture toughness supports the whole disc and the reinforced part by ceramic particles/whiskers is used in the area required (e.g. frictional area) (Fig. 1.1 and 1.2). To produce locally or partially reinforced materials squeeze casting is the most common and feasible techniques. Some of manufacturing processes of locally reinforced (A365 Al alloy locally reinforced by SiC particles) friction ring with a ductile carrier body and their mechanical performance have been investigated by Zeuner et al. in 1998 [5] where, they found that the friction ring of an Al alloy locally reinforced by SiC particles can capable to use as a brake disc application.

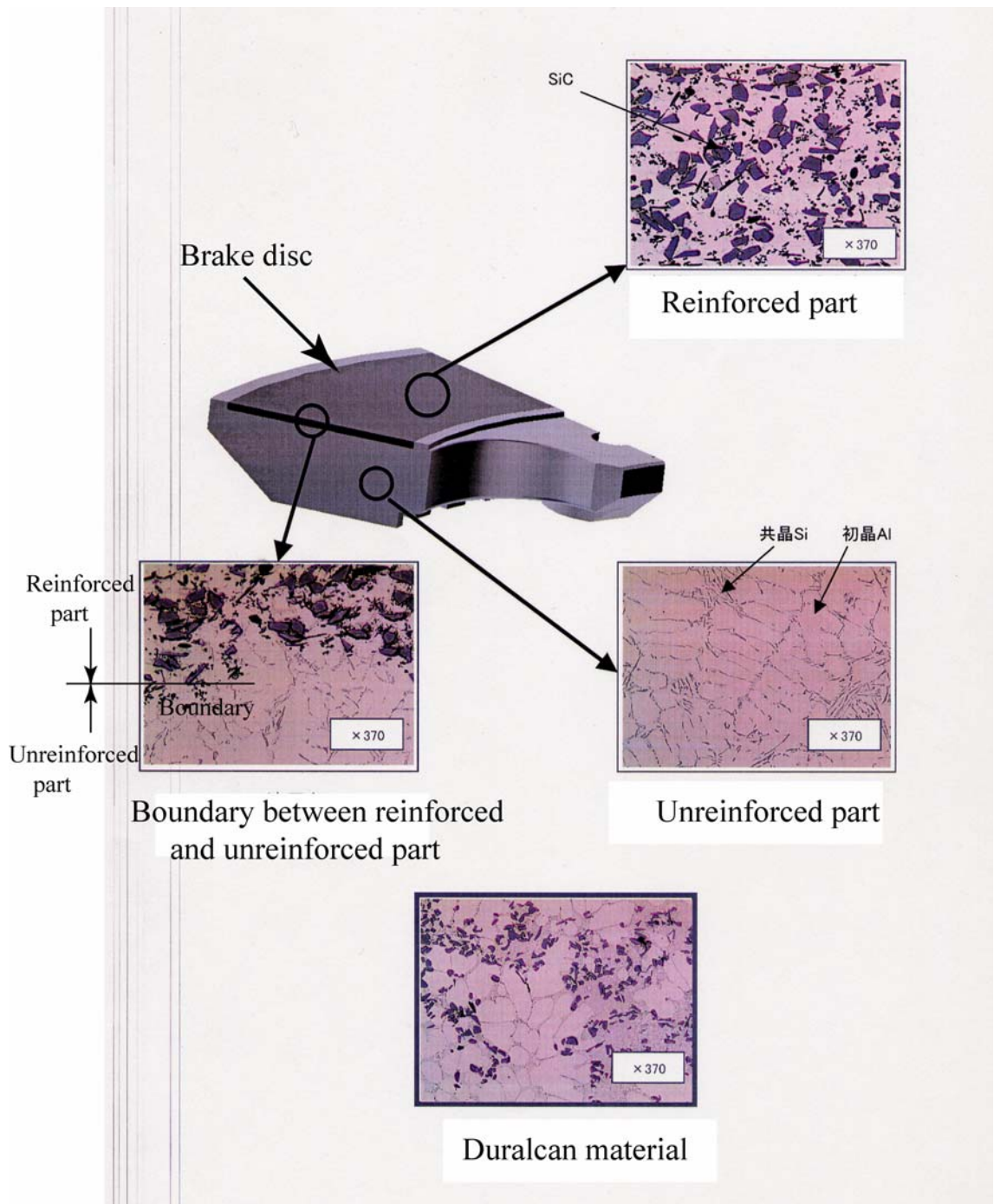


Fig.1.1 Brake disc structure

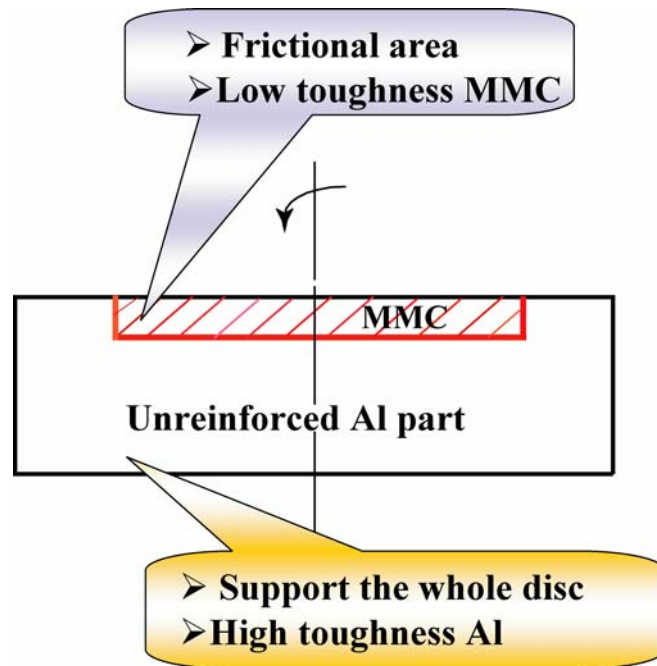


Fig.1.2 Example illustration of application of locally reinforced material

A locally reinforced material has a boundary between the reinforced part and the unreinforced part. The resulting strength of the boundary between locally reinforced and unreinforced parts will undoubtedly play an important role in many structural applications. The fracture location and the fracture mechanism give critical information for the design or placement of the mechanical component having the locally reinforced part. Therefore, various experimental and numerical investigations are needed to clarify the role of boundary on fracture mechanism of locally reinforced material. By using hybridization techniques, the combined application of particles and whiskers to the reinforced part in a locally reinforced material may improve the mechanical performance for the structural applications. So, the effect of boundary and fracture mechanism of hybrid MMCs would be studied for the safety of engineering application.

1.4 Literature review

During the past decades, many investigations have been carried out on the mechanical performance of MMCs relating to aspects such as strength, damage, and failure mechanism [5-22]. MMCs have high strength and stiffness, low density, high temperature properties and excellent wear resistance compared to unreinforced materials [1-4]. Despite their excellent mechanical properties, low ductility is the limitation for this material. In order to improve ductility of MMCs, it is needed to study the factor which resulting the low ductility. In generally, presence of second phase brittle reinforcement and their fracture are considered as the main factor of decreasing the ductility of MMCs. But the presence of reinforcements is also the main strengthening mechanism of MMCs [6]. Many researchers were investigated the effect of the reinforcement volume fraction, size and shape and distribution on mechanical performance [7, 8]. Particle clustering effect may reduce the ductility of composite [8]. Increase the volume fraction of reinforcement promotes the higher tensile stress in the reinforcement causing higher degree of particle fracture [17]. Reinforcement shape also has a strong influence of failure mechanism in the metal matrix composites. In 1991, Lorca et al. showed that rounded corner reinforcement increase ductility and delay the void growth significantly compared with the sharp corner reinforced metal matrix composites [18].

Many researchers have investigated the monotonic and cyclic fracture behavior and the fracture mechanisms of ceramic particulates/aluminium based MMCs [9-25]. Large difference in strain carrying capability of elastically deforming reinforcement and plastically deforming matrix alloy determines the key mechanism of fracture of MMCs

[11-18]. Thus, stress is concentrated near the interface edge between reinforcement and matrix or concentrated in the reinforcement, which causes interfacial debonding or reinforcement fracture. This reinforcement fracture or interfacial debonding may decrease the ductility of MMCs [11].

Plastic constraint developed in the matrix has strong effect on cyclic and monotonic deformation of MMCs. Deformation and failure of MMCs by the nucleation and growth of voids and within the ductile matrix were studied by Lorca et al. [17, 18, 20]. They demonstrated that due to constrained plastic flow of the matrix between the reinforcement particles in the MMCs, hydrostatic stresses develop in the matrix which plays an important role in the failure mechanism during monotonic and cyclic deformations [17-19]. This hydrostatic stress enhances the nucleation of the voids in the matrix alloy. Different constraint levels on the matrix flow may control the local failure process (e.g. particle fracture, interfacial debonding and dimple fracture of matrix alloy). In the particulate composites the plastic strain and voids around the inclusions spread throughout the matrix whereas, in the whisker reinforced composite they are localized in the vicinity of the reinforcement [17].

The failure mechanism is greatly influenced by different loading condition (e.g. monotonic and cyclic load). Poza et al. demonstrated the difference of fracture mechanism of a metal matrix composite under monotonic and cyclic loading condition [19]. The tension loaded reinforcements in the matrix are subjected to higher tensile stress than those loaded in fatigue results in high degree of reinforcement fracture. During the loading and unloading process in the cyclic deformation cyclic hardening is

occur due to the accumulation of plastic strain. During the monotonic deformation the plastic strain also develop, especially at the interface between reinforcement and matrix, but significantly lower than in cyclic deformation [19].

The presence of interfaces is the common feature of MMCs which has an important role in mechanical behaviors of these materials such as strength and stiffness. Strong interface between matrix and reinforcement, the triaxiality of stress generated during tensile deformation causes the void growth within the matrix [20]. The failure of a composite often arises at the interface. Therefore the mechanical behavior of interfaces has a strong influence on the mechanical properties of composites, including their strength and toughness. Good interfacial bonding yields high dislocation density in the matrix which increases the strength of MMCs, while low fracture toughness due to cracking of the reinforcing particles is given by the good interfacial bonding [21]. Moreover, interfacial bonding between reinforcing particles and matrix alloy also tends to be a dominating factor in local failure processes and the strengthening of MMCs.

Due to thermal load and external load such as brake force acting on the component, the locally reinforced materials are subjected to in-plane load of the reinforced face in which the whiskers are distributed randomly and also out-of-plane load which is perpendicular to the whisker orientation. The mechanical properties of whisker/ particle composites are strongly dependent on their compositions and the volume fraction as well as the arrangement of reinforcement such as random orientation and distributions. In the whisker/fiber composites, the whisker/fiber orientation with respect to the load is very important. Due to the large influence of whisker/fiber orientation on mechanical

properties (e.g. fracture behavior and overall strength) many researchers have investigated the whisker/fiber composites [26-36]. Some studies have shown that the composite strength highly depends on its reinforcement orientation [26-31]. Kang et al. Showed that the elastic modulus and fiber axial stress is strongly dependent on the fiber orientation angle (α) [26, 27]. The strength of whisker/particle composites is greatly influenced by load transfer from matrix to reinforcement [27]. Whisker-matrix stress transfer in whisker/fiber composite have been generally accepted as a predominant parameter in controlling the micro-failure modes and the most important influencing factor in macroscopic mechanical behavior. The load transfer between whisker and matrix in a metal matrix composite (MMC) depends on the properties and conditions of the whisker/matrix interfacial region. The interfacial bond has a remarkable effect on the stress transfer from matrix to whisker. Good interfacial bonding enhances the stress transfer between matrix and fiber which results in increase of overall strength [27]. Elastic modulus and axial strength of composites are increased with decreasing the orientation angle ($\alpha = 0^\circ$ is parallel to the externally applied stress direction). Other literatures show that the stress in whisker parallel to the loading direction ($\alpha = 0^\circ$) is largest compared with other orientation angle [28, 29]. Trojanova et al. [30] demonstrated that the tensile strength is significantly increased in the parallel orientation ($\alpha = 0^\circ$) of whisker composite compared with the perpendicular orientation ($\alpha = 90^\circ$) of Al_2O_3 whisker MMC. However Nutt et al. demonstrated that, in the whisker reinforced MMCs a hydrostatic stresses develop in the vicinity of the whisker ends which lead to debonding the whisker from the matrix and also low ductility and premature failure [34-36].

A few investigations have been made recently [37–42] in which the influence of hybrid reinforcements such as silicon carbide + graphite, Al_2O_3 + silicon carbide and carbon fiber + alumina on the wear/tribological behavior of aluminum were investigated. Moreover, some studies have focused on the hybrid effect on the mechanical properties of whisker/particle hybrid metal matrix composites [37-39]. In 2000, wear behavior of Al/ Al_2O_3 /C hybrid metal matrix composites were investigated by Song et al. [37]. The wear resistance was remarkably increased compare with Al/ Al_2O_3 composite due to hybrid effect. Other literature shows that wear resistance of hybrid MMCs are higher under dry sliding condition but lower under lubricated sliding condition compared with the non-hybrid MMCs [38]. An analytical analysis considering tensile strength and stiffness enhancement in particle/fiber reinforced aluminum hybrid metal matrix composites were investigated by Jung et al. in 2000 [39]. They have demonstrated that the strength and stiffness of hybrid composites are much larger than the fiber composite due to the cluster structure which increased the bending rigidity and change the fracture mechanism.

A locally reinforced material consists of reinforced part and unreinforced part. The resulting strength of the boundary between locally reinforced and unreinforced parts will undoubtedly play an important role in many structural applications. The fracture location and the fracture mechanism give critical information for the design or placement of the mechanical component having the locally reinforced part. Under a mechanical loading or temperature change, high stresses occur near the interface edge in the joint of two homogeneous dissimilar materials due to the mismatch of material properties (e.g. thermal and elastic mismatch, plastic flow stress etc.) of the joined

components [43-45]. These high stresses (stress singularity) may influence the fracture of the joint.

The stress concentration and its influence on the fracture behavior around the boundary of locally reinforced materials is an unsolved problem. The best of our knowledge, there is no experimental and numerical investigations of locally of partially reinforced materials have been conducted, especially those reinforced by SiC particles and Al₂O₃ whiskers and having a macroscopic boundary between reinforced and unreinforced part. Studies of the fracture mechanism, under monotonic and cyclic load, of aluminium cast alloy, locally reinforced by SiC particulates and Al₂O₃ whiskers, are rare. We believe that knowledge of monotonic and cyclic fracture behaviors of the locally reinforced aluminium alloy would have an essential role for many structural applications such as in the brake disc of a high speed railway coach.

In order to describe the whisker orientation effect on overall strength of composites, a large number of experimental and numerical investigations have been carried out successfully [26-36]. However, the whisker orientation and the hybrid (reinforced by whisker and particle) effect on overall strength in the hybrid composites are still unsolved problem. The effect of whisker orientation on the strength of hybrid composites (reinforced by whisker and particle) is very complicated due to the presence of whiskers and particles. Due to the complicated microstructure, various experimental and numerical investigations are needed to be explained to clarify the fracture mechanism of the composite. Therefore, in this research, an experimental and numerical investigation was carried out to describe the whisker orientation effect on overall strength of hybrid composites.

1.5 Scope and objectives

The best knowledge on the research of locally or partially reinforced MMCs is strongly required to secure the structural application. The aim of the present research is to clarify the effects of the boundary between the reinforced part and the unreinforced part on the fracture mechanism, under monotonic and cyclic load, of aluminium cast alloy locally reinforced by SiC particles and Al₂O₃ whiskers. Also the effect of the whisker orientation on the monotonic strength and fatigue strength and its effect on fracture mechanism of aluminium cast alloy locally reinforced by SiC particles and Al₂O₃ whiskers under monotonic and cyclic load are investigated. Fractographic analysis is used to explain the failure location and the fracture mechanism. The stress and strain distributions predicted by simulations, using a microscopic mechanical model for the locally reinforced materials, are compared to the experimental observations. A three-dimensional single whisker unit cell model of cylindrical shape whisker in the periodic boundary condition is conducted using finite element method (FEM) to describe the overall behavior of the composite.

The specific objectives of the present research are as follows:

- To investigate the effect of the boundary between the reinforced part and the unreinforced part on the fracture mechanism under monotonic and cyclic load.
- To investigate the effect of monotonic and cyclic load on the fracture mechanism of MMCs.
- To investigate the effect of the whisker orientation on the monotonic strength and fatigue strength and on the fracture mechanisms.
- The stress and strain distributions predicted by simulations, using a microscopic

mechanical model for the locally reinforced materials, are discussed with the experimental observations.

- The whisker orientation effects predicted by using a three-dimensional single whisker model are compared to the experimental observations.

1.6 Outline of present research

The research work conducted for this project is completely presented in this dissertation, which is organized as follows:

Chapter 1 is an introduction of the research, which describes the back ground, the motivation, proposed concepts, the objectives and the scopes of this research.

In chapter 2, Materials fabrication and its microstructure, the experimental set up and the experimental procedures were discussed. Materials were successfully fabricated by squeeze casting method. The polishing surface observations were treated by optical microscope. The fracture surface observations of the composites were treated by the scanning electron microscope (SEM). The failure mechanisms of the composites were investigated by the composition analysis of energy dispersive X-ray (EDX). The measured areas of dimple, interfacial debonding and particle/whisker fractures on the fracture surface were also examined by area fraction techniques.

In chapter 3, the experimental results were discussed, which describes the fracture mechanisms, boundary effect and whisker orientation effect. The fracture path and fracture origin were investigated by SEM on the fracture surfaces. With respect to the load, the whisker orientation effect was investigated by SEM and EDX analysis.

In chapter 4, a numerical analysis was discussed. The stress distribution around the boundary between reinforced part and unreinforced part were calculated based on an inclusion array model considering the microscopic inhomogeneous effects. A three-dimensional single whisker unit cell model of cylindrical shape whisker in the periodic boundary condition was conducted using finite element method (FEM) to describe the overall behavior of the composite.

In chapter 5, the general conclusions and directions for future investigation were given.

References

- [1] Suresh, S., Mortensen, A. and Needleman, A. Fundamentals of metal matrix composites. London: Butterworth/Heinemann; 1993.
- [2] K. U. Kainer., Basic of Metal Matrix Composite, in Custom-made Materials for Automotive and Aerospace Engineering., 2006, WILEY-VCH Verlag GmbH and Co. KGaA, Weinheim.
- [3] D.B. Miracle., Metal matrix composite- From science to technological significance, *Composite Science and Technology*, Vol. 65 (2005), pp. 2526-2540
- [4] Xicong, Liu. and Claude, Bathias., Defects in squeeze-cast Al₂O₃/Al alloy composites and their effects on mechanical properties, *Composite Science and Technology*, Vol. 46(1993), pp. 245-252.
- [5] Zeuner, T., Stojanov, P., Sahm, P.R., Ruppert. H., and Engels A., Developing trends in disc brake technology for rail application, *Material Science and Technology*, Vol. 14 (1998), pp. 857-863.
- [6] N. Shi and R. J. Arsenault: Plastic flow in SiC/Al composites-strengthening and ductility. *Annual Review Material Science*, Vol. 24 (1994), pp. 321-357.
- [7] Y. Ochi, K. Masaki, T. Matsumura and M. Wadasako: Effects of volume fraction of alumina short fibers on high cycle fatigue properties of Al and Mg alloy composites. *Material Science and Engineering A*, Vol. 468-470 (2007), pp. 230-236.
- [8] T. C. Tszeng: The effects of particle clustering on the mechanical behavior of particle reinforced composites. *Composite Part B*, Vol. 29B (1998), pp. 299-308.
- [9] M. Levin and B. Karlsson: Influence of SiC particle distribution and prestraining on fatigue crack growth rates in aluminum AA 6061-SiC composite *Material*

- Science and Technology*, Vol. 7 (1991), pp. 596-607.
- [10] D. L. Davidson: Fatigue and fracture toughness of aluminum alloys reinforced with SiC and alumina particles *Composite*. Vol. 24 (1993), pp. 248-255.
- [11] AL. Chen, Y. Arai and E. Tsuchida: An experimental study on effect of thermal cycling on monotonic and cyclic response of cast aluminum alloy-SiC particulate composites. *Composites Part B.*, Vol. 36 (2005), pp. 319-330.
- [12] AL. Chen, Y. Arai and E. Tsuchida: A numerical study on effect of thermal cycling on monotonic and cyclic response of cast aluminum alloy-SiC particulate composites. *Theoretical Applied Mechanics*, Vol. 53 (2004), pp. 63-73
- [13] T.S. Srivatsan and M. Al-Hajiri: The fatigue and final fracture behavior of SiC particle reinforced 7034 aluminum matrix composites., *Composite Part B.*, Vol. 33 (2002), pp. 391-404.
- [14] Q. Zhang, H. Zhang, Gu. Mingyuan and J. Yanping: Studies on the fracture and flexural strength of Al/Si_p composite. *Materials Letters*. Vol. 58 (2004), pp. 3545-3550.
- [15] X. Q. Xu and D. F. Watt: A finite element analysis of plastic relaxation and plastic accumulation at second phase particles. *Acta Materilia.*, Vol. 44 (1996), pp. 801-811.
- [16] X. Q. Xu and D. F. Watt: A numerical analysis of the effects of reinforcement content on strength and ductility in Al/(SiC)_p MMCs. *Acta Materilia.*, Vol. 44 (1996), pp 4501-4511.
- [17] L. Llorca, S. Suresh and A. Needleman: An experimental and numerical study of cyclic deformation in metal-matrix composites. *Metallurgical Transaction A*: Vol. 23A (1992), pp. 919-934.

- [18] L. Llorca, A. Needleman and S. Suresh: An analysis of the effects of matrix void growth on deformation and ductility in metal-ceramic composites. *Acta Metall. Mater.*, Vol. 39, No. 10 (1991), pp. 2317-2335.
- [19] P. Poza and J. Llorca: Mechanical behavior and failure micromechanisms of Al/Al₂O₃ composites under cyclic deformation. *Metallurgical and materials Transaction A*: Vol. 26A, pp. 3131-3141, 1995.
- [20] T. Christman, A. Needleman and S. Suresh: An experimental and numerical study of deformation in metal-ceramic composites. *Acta Materialia.*, Vol. 37, No. 11, pp. 3029-3050, 1989.
- [21]. R.J. Arsenault and Y. Flom: Proc. Symp. Phase Boundary Effects on Deformation, *TMS, AIME, Toronto, Canada*, pp. 261 – 279, 1985.
- [22] H. Lilholt: Aspects of deformation of metal matrix composites. *Material Science and Engineering A*, Vol. 135, pp. 161-171, 1991.
- [23] T. S. Srivatsan, M. Al-Hajiri and V. K. Vasudevan: Cyclic plastic strain response and fracture behavior of 2009 aluminum alloy metal-matrix composite. *International Journal of Fatigue*, Vol. 27, pp. 357-371, 2005.
- [24] R. J. Zhang, Z. Wang and C. Simpson: Fatigue fractography of particulate-SiC reinforced Al (A356) cast alloy. *Material Science and Engineering*, Vol. A148, pp. 53-66, 1991.
- [25] J. Llorca and P. Poza: Influence of matrix strength on reinforcement fracture and ductility in Al-Al₂O₃ composites. *Material Science and Engineering*, Vol. A185, pp. 25-37, 1994.
- [26] Guo-Zheng, Kang. and Quing, Gao., Tensile properties of randomly oriented short δ -Al₂O₃ fiber reinforced aluminium alloy composites: 1. Microstructure

- characteristics, fracture mechanisms and strength prediction, *Composites part A*, Vol. 33 (2002), pp. 647-656.
- [27] Guo-Zheng, Kang. and Quing, Gao., Tensile properties of randomly oriented short δ -Al₂O₃ fiber reinforced aluminium alloy composites: 2. Finite element analysis for stress transfer, elastic modulus and stress-strain curve, *Composites part A*, Vol. 33 (2002), pp. 657-667.
- [28] Bing, Jiang., Charlie, Liu., Chuck, Zhang., Ben, Wang. and Zhi, Wang., The effect of nono-symmetric Distribution of fiber orientation and aspect ratio on elastic properties of composites, *Composites part B*, Vol. 38 (2007), pp. 24-34
- [29] Li, A.B., Geng, L., Meng, Q.Y. and Zhang, J., Simulation of the large compressive deformation of the metal matrix composites with misaligned whiskers, *Material Science. and Engineering A*, Vol. 358 (2003), pp. 324-333.
- [30] Trojanova, Z., Szaraz, Z., Labar, J. and Lukac, P., Deformation behaviour of an AS21 alloy reinforced by short Saffil fibers and SiC particles, *Journal of Material Processing Technology*, Vol. 162-163 (2005), pp. 131-138.
- [31] Xicong, Liu. and Claude, Bathias., Defects in squeeze-cast Al₂O₃/Al alloy composites and their effects on mechanical properties, *Composite Science and Technology*, Vol. 46(1993), pp. 245-252.
- [32] Rafiqzaman, MD. and Arai, Y., Fracture mechanism of aluminium cast alloy locally reinforced by SiC particles and Al₂O₃ whiskers under monotonic and cyclic load, *Material Science and Technology*, 2007(to be published).
- [33] Levy, A. and Papazian, J. M., Tensile properties of short fiber-reinforced SiC/Al composites: part 2. Finite-Element analysis, *Metallurgica Transection A*, Vol. 21 (1990), pp. 411-420

- [34] T. Christman, A. Needleman, S. Nutt and S. Suresh: On microstructural evolution and micromechanical modeling of deformation of a whisker-reinforced metal-matrix composite. *Material Science and Engineering A*, Vol. 107, pp. 49-61, 1989.
- [35] S. R. Nutt and J. M. Duva: A failure mechanism in Al-SiC composites. *Scripta Metallurgica*, Vol. 20, pp. 1055-1058, 1986.
- [36] S. R. Nutt and A. Needleman: Void nucleation at fiber ends in Al-SiC composites. *Scripta Metallurgica*, Vol. 21, pp. 705-710, 1987.
- [37]. J. I. Song, S. I. Bae, K. C. Ham and K. S. Han: Abrasive wear behavior of hybrid metal matrix composites. *Key Engineering Materials*, Vols. 183-187, pp. 1267-1272, 2000.
- [38] H. Fu, K. Han and J. Song: Wear properties of saffil/Al, saffil/Al₂O₃/Al and saffil/SiC/Al hybrid metal matrix composites. *Wear*, Vol. 256, pp. 705-713, 2004.
- [39]. S.W. Jung, J. H. Lee, J. B. Nam, H. W. Nam and K. S. Han: Analysis of strengthening mechanism in hybrid short fiber/particle reinforced metal matrix composites. *Key Engineering Materials*, Vols. 183-187, pp. 1297-1302, 2000.
- [40] X. N. Zhang, L. Geng and G. S. Wang: Fabrication of Al-based hybrid composites reinforced with SiC whiskers and SiC nanoparticles by squeeze casting. *Journal of Material Processing Technology*, Vol. 176, pp. 146-151, 2006.
- [41] J. Q. Jiang, H. N. Liu, A. P. Ma and R.S. Tan: The structure and tensile properties of Al-Si alloy hybrid reinforced with alumina-aluminosilicate short fiber. *Journal of Material Science*, Vol. 29, pp. 3767-3773, 1994.
- [42] A. B. Gurcan and T. N. Baker: Wear behaviour of AA6061 aluminium alloy and its composites. *Wear*, Vol. 188, pp. 185-191, 1995.

- [43]. D. B. Bogy: Edge-bonded dissimilar orthogonal elastic wedge under normal and shear loading. *ASME Journal of Applied Mechanics*. Vol. 35, pp. 460-466, 1968.
- [44] B. J. Dalgleish, M. C. Lu and A. G. Evans: The strength of ceramics bonded with metals. *Acta Metallurgical*. Vol. 36, pp. 2029-2035, 1988.
- [45] M.A. Sckuhr, A. Brueckner-fott, D. Munz and Y. Y. Yang: Stress singularities at a joint formed by dissimilar elastic-plastic materials under mechanical loading. *International Journal of Fracture*. Vol. 77, pp. 263-279, 1996.

Chapter 2: Materials and Experimental Procedures

The aim of this chapter is to describe the material fabrication and preparation for the bending test and then described the experimental procedures and methodology of this research. For minimizing the limitation of MMCs (low ductility and higher cost), in our research we introduced the new conception locally reinforced material for structural applications especially in the brake disc application. The locally reinforced brake discs were fabricated successfully by squeeze casting method. Monotonic and cyclic bending tests were conducted by MTS machine with a special bending fixture. The fracture surface observations of the composites were made by the SEM. The failure mechanisms of the composites were investigated by the composition analysis of EDX.

2.1 Materials fabrication

Metal matrix composites are generally produced either by liquid metallurgy or powder metallurgy techniques [1-3]. In the liquid metallurgy, the reinforcement phase is mechanically dispersed in the liquid before solidification of melt. For the production of low cost and complex shaped MMCs, squeeze casting technology have now become most feasible techniques. In the present work, materials were fabricated by squeeze casting method. Commercial aluminum alloy of JIS-AC4CH was used as a based material [6]. The chemical composition of the aluminum alloy is given in Table 1.

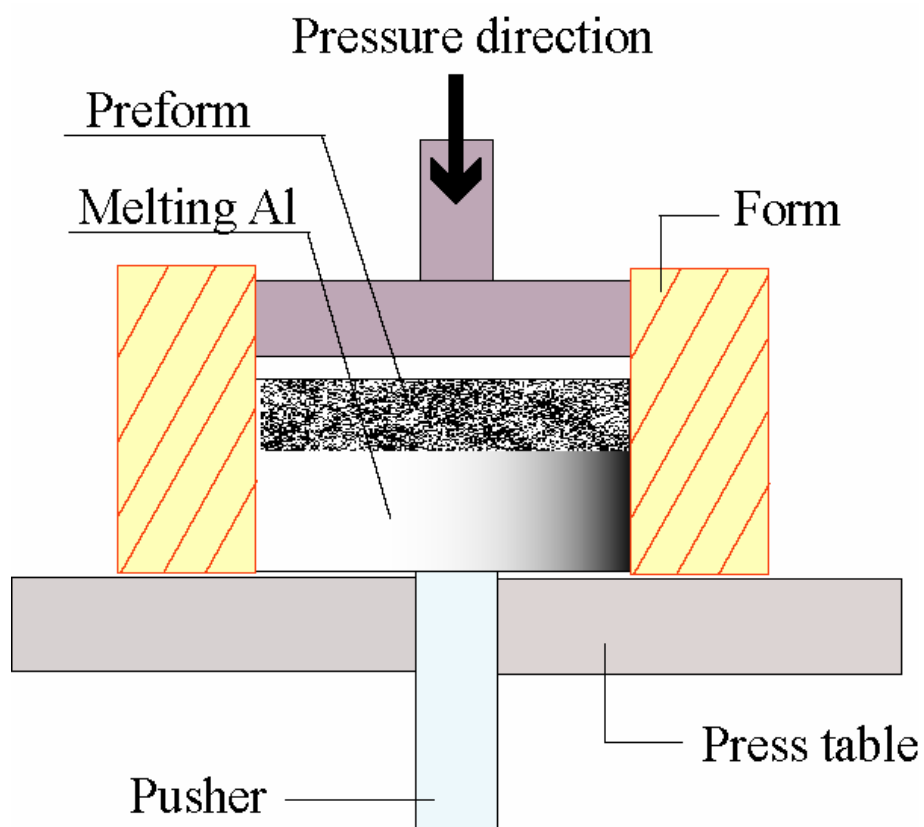


Fig 2.1 Squeeze casting method

Table 1 Chemical compositions of AC4CH alloy (wt. %)

Si	Fe	Mg	Ti	Al
7.99	0.2 max	0.57	0.07	Bal.

Table 2 Volume fraction and mechanical properties

Parameters	Al ₂ O ₃	SiC	AC4CH alloy	MMC
Volume contents (%)	9	21	70	-
Young's Modulus (GPa)	380	450	70.0	142
Poisson's ratio	0.27	0.20	0.33	0.28
Yield strength (MPa)	-	-	131	166

The reinforced phase consisted of 21 volume% SiC particles and 9 volume% Al₂O₃ whiskers. The locally reinforced part was fabricated with the squeeze casting method shown in Fig. 2.1. Hybrid preforms which are made of SiC particles and Al₂O₃ whiskers are placed in the die cavity and therefore the molten Al alloy was poured in to the mold. Subsequently, 100 MPa pressure was applied on the mixture using a hydraulic press. The squeeze casting pressure of 100 MPa is adequate to overcome the resistance against flow and to press the melt into all the open pores of the hybrid preform. Volume fractions and mechanical properties are listed in Table 2.

2.2 Materials preparation

The test specimens were cut out from a locally reinforced aluminium disc shown in Fig. 2.2. The bend specimen size (width, depth and length) is limited by the limited MMC layer thickness. To investigate the boundary effect, whisker orientation effect and the fracture mechanism, two types of specimens were prepared for the bending test shown in Fig. 2.2. The longitudinal orientation is normal to or parallel to the boundary ($r - \theta$ plane in Fig. 2.2) between reinforced part and unreinforced part. The former is called as “locally reinforced material ($\alpha = 90^\circ$)”. The latter is called as “homogeneous MMC ($\alpha = 0^\circ \sim 90^\circ$)”.

2.3 Microstructural features

The machined surfaces of the specimens were hand polished using progressively finer grade (2000 and 3000 grit) of silicon carbide impregnated emery paper and then finished with a polishing machine using 1 μm diamond particles until all scratches and surface machining marks were removed. The typical microstructure of locally

reinforced material ($\alpha = 90^\circ$) and the homogeneous MMC ($\alpha = 0^\circ \sim 90^\circ$) is shown in Fig 2.3 which representing the SiC particles and Al₂O₃ whiskers distribution, boundary between reinforced part and unreinforced part and Al₂O₃ whisker orientation angle α . Most of the SiC particles are rectangular-shaped with sharp corners and most of the Al₂O₃ whiskers are roller-shaped as shown in Fig. 2.3(a) and Fig. 2.3 (c). The SiC particles have an average length of $23 \mu m$. The average length of the Al₂O₃ whiskers is $33 \mu m$ and the average diameter is $2 \mu m$. In the Al alloy side, the Al has an average grain size of $48 \mu m$.

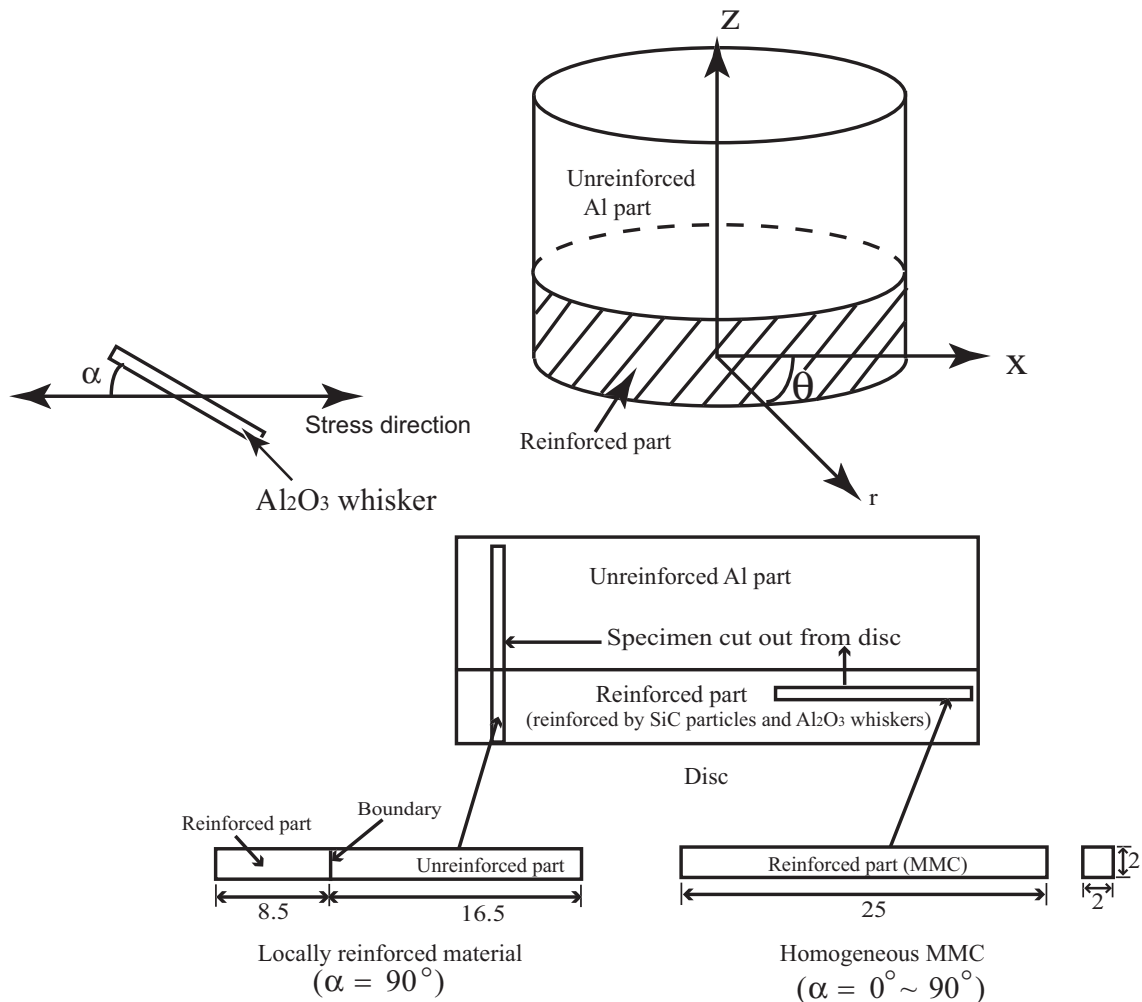


Fig 2.2 Specimen cut out from a disc (unit: mm)

At frequent intervals a clustering of SiC particles and Al₂O₃ whiskers were observed in the low magnification photograph as shown by the dashed line in Fig.2.3 (b). The cluster has an average size of 90 μm . Fig. 2.3 (d) represent the Al₂O₃ whisker orientation angle α . Generally, the Al₂O₃ whisker orientation in the disc is random in $r - \theta$ plane in Fig.2.2. In the “homogeneous MMC” specimen whiskers are oriented randomly ($\alpha = 0^\circ \sim 90^\circ$) to the load direction (Fig. 2.3(c)) and in the “locally reinforced material” almost all whiskers are perpendicular ($\alpha = 90^\circ$) to the load direction as shown in Fig. 2.3(a) and the cross-section shape is almost circle.

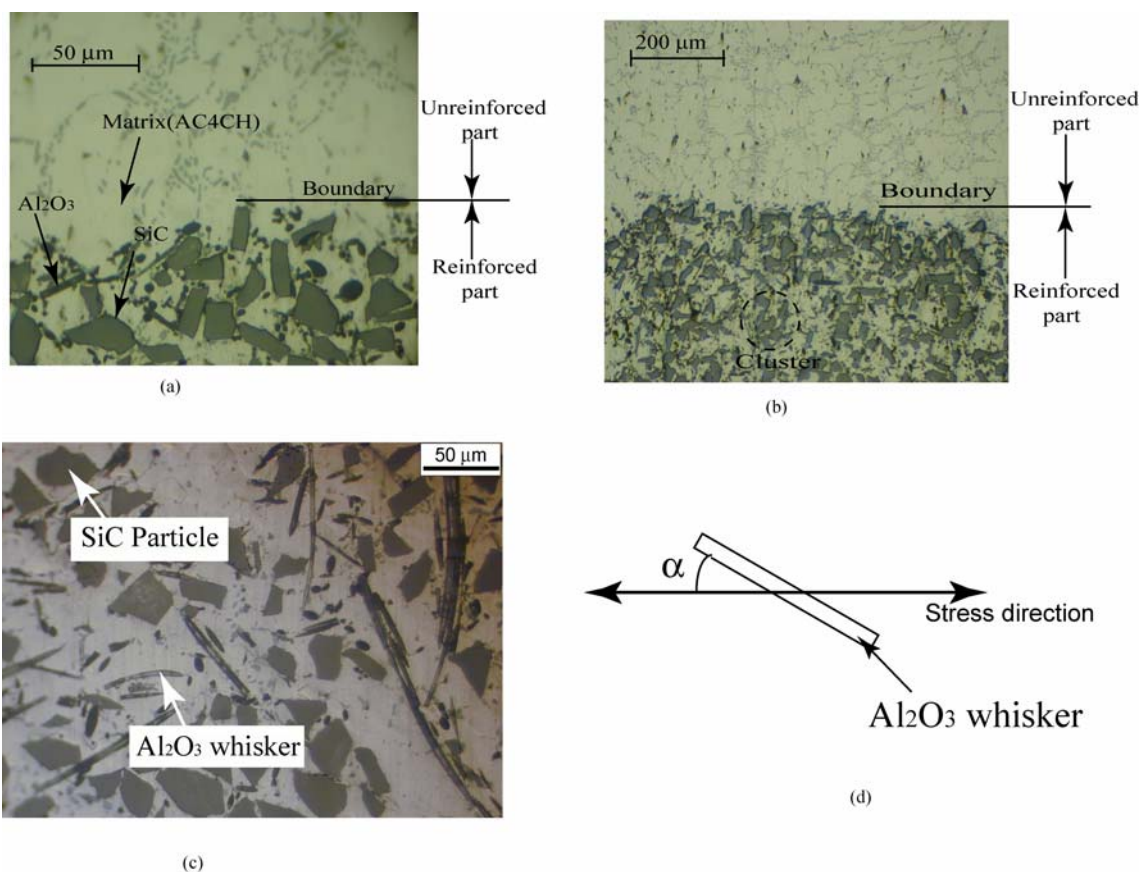


Fig. 2.3 Optical micrograph of the composite on the tensile side face, representing the SiC particle and Al₂O₃ whisker distribution and Al₂O₃ whisker orientation angle: (a) and (b) Locally reinforced material ($\alpha = 90^\circ$) and (c) Homogeneous MMC ($\alpha = 0^\circ \sim 90^\circ$) (d) Definition of whisker orientation angle α .

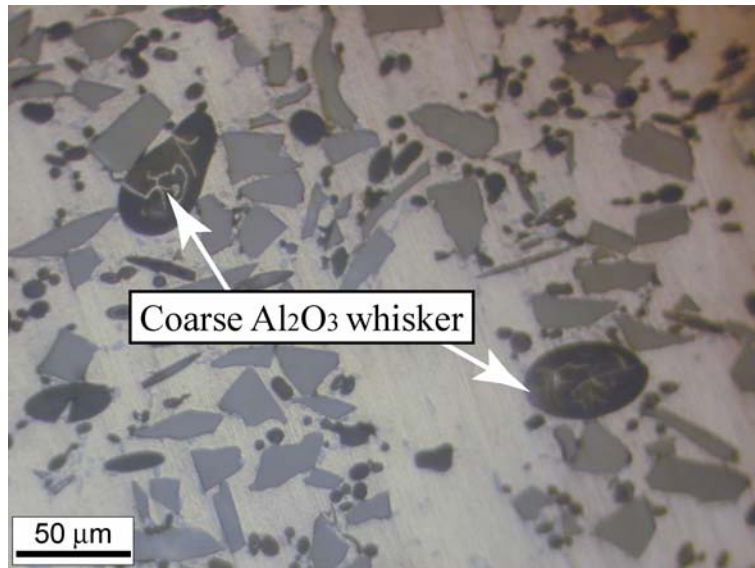


Fig. 2.4 Optical micrograph of the composite on the tensile side face, representing the coarse Al₂O₃ whiskers which were formed during the materials fabrication.

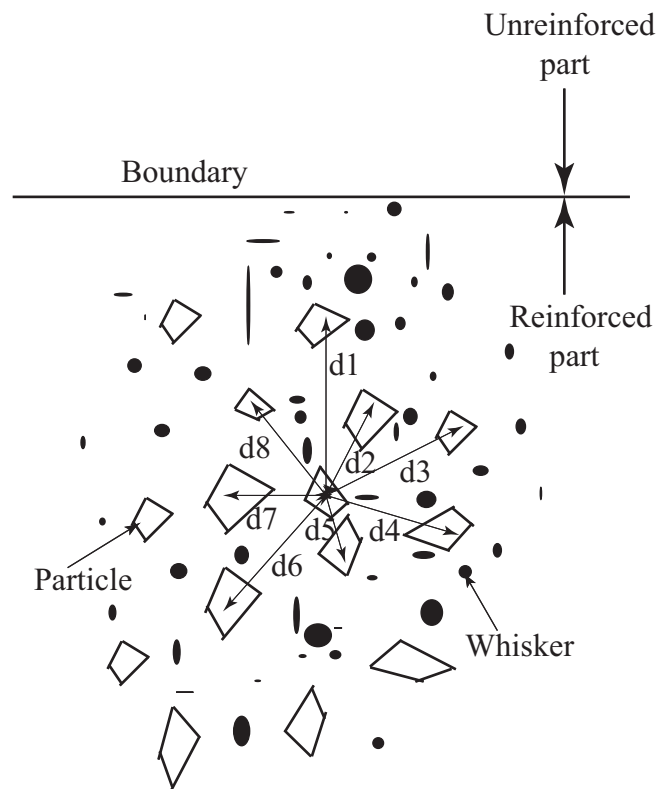


Fig. 2.5 Measurement of inter particle/whisker distance with respect to the boundary between reinforced and unreinforced part.

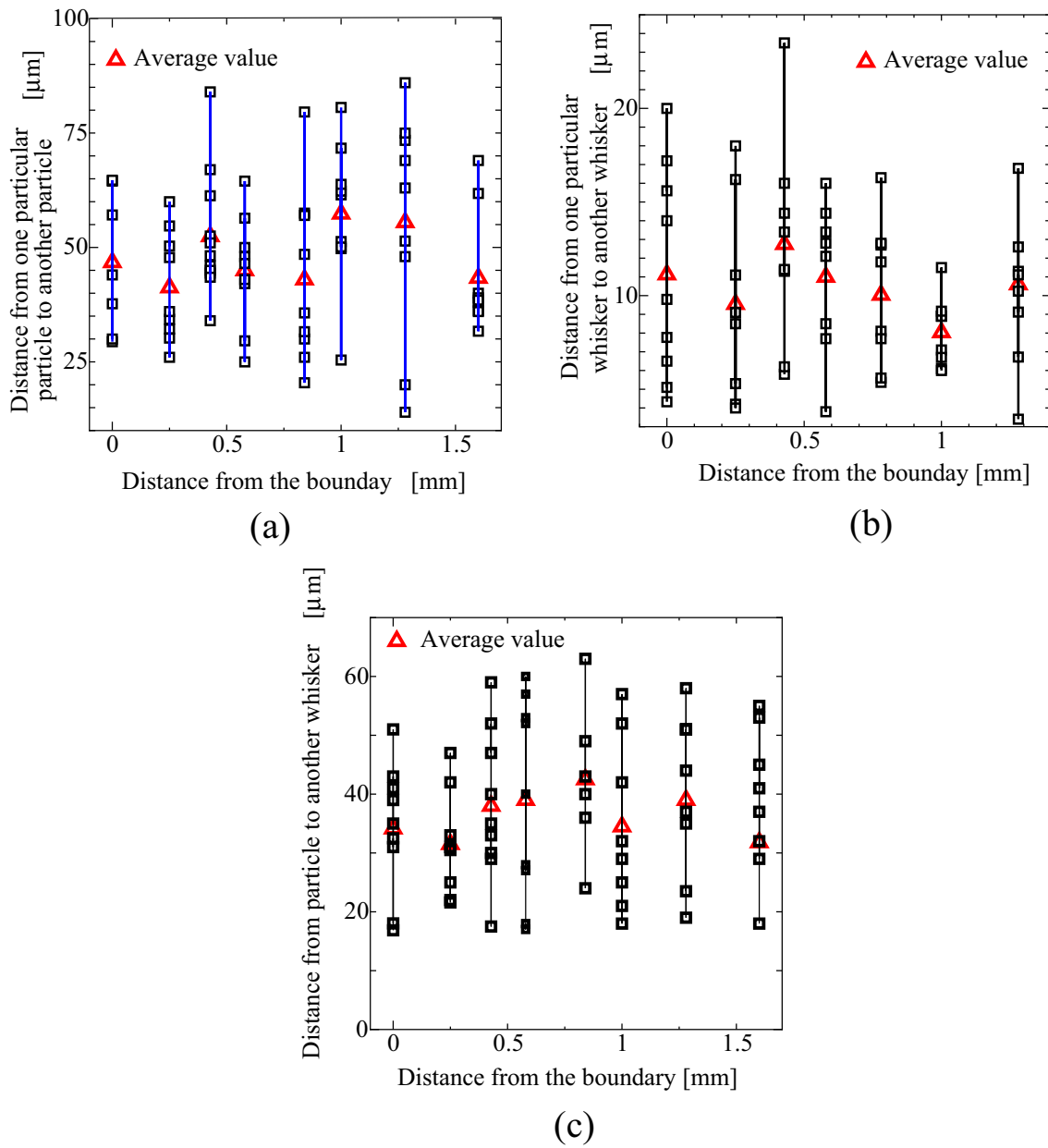


Fig. 2.6 Inter particle/whisker distance with respect to the boundary (a) particle to particle (b) whisker to whisker (c) particle to whisker

Some coarse Al_2O_3 whisker which is formed during the fabrication of hybrid whisker/particle preform is shown in Fig 2.4. When the materials subjected to monotonic and cyclic loading, this coarse Al_2O_3 might have an influence on failure

mechanism of the composite such as premature failure (crack initiation in the coarse Al_2O_3 and propagation quickly) the monotonic and cyclic test. Also this can be point out that; the coarse Al_2O_3 whisker does play an important role in mechanical properties.

To evaluate the density of reinforcement with respect to the boundary, inter particle/whisker distance was calculated (Illustration shown in Fig. 2.5) and the results shown in Fig. 2.6. From this results, it can be seen that the inter particle/whisker distance with respect to the boundary is random. Therefore, the particle/whisker dispersed randomly through matrix alloy.

2.4 Experimental setup and procedures

Symmetric four-point bending tests were performed using special bending fixtures equipped with a 980N load cell. An experimental set up is shown in Fig 2.7. The inner span was 10 mm and outer span was 20 mm. Load and deflection data were recorded by a computer data acquisition system. Monotonic bending tests were conducted with a displacement rate of 0.0025 mm s^{-1} . Strength was calculated from the maximum load at failure as a nominal bend stress. Schematic illustration of four-point bending test is shown in Fig. 2.8. The nominal bending stress was calculated from the following equation

$$\sigma_b = \frac{6aP}{2bh^2} \dots\dots\dots (2.1)$$

Cyclic fatigue tests were conducted in the load control mode under the load ratio $R = 0.1$ at a frequency of 1Hz and 10 Hz. All tests were carried out at room temperature. The number of cycles to failure is taken as the fatigue life (N_f). The tensile surfaces of broken specimens were examined with an optical microscope to determine the fracture

initiation location. Fracture surfaces were comprehensively examined in a SEM to determine the microscopic fracture mode and to characterize the microscopic mechanisms governing fracture. The microscopic mechanism refers to the local failure processes (fracture of particle or whisker, particle/matrix or whisker/matrix interfacial debonding, dimple fracture of matrix alloy). Energy Dispersive X-ray analysis (EDX) was used to identify constituents on the fractured surface. Special effort was made to take matching photographs from the two halves of the broken specimens to assess the relative incidence of particle/whisker cracking and particle/matrix or whisker/matrix interfacial debonding.

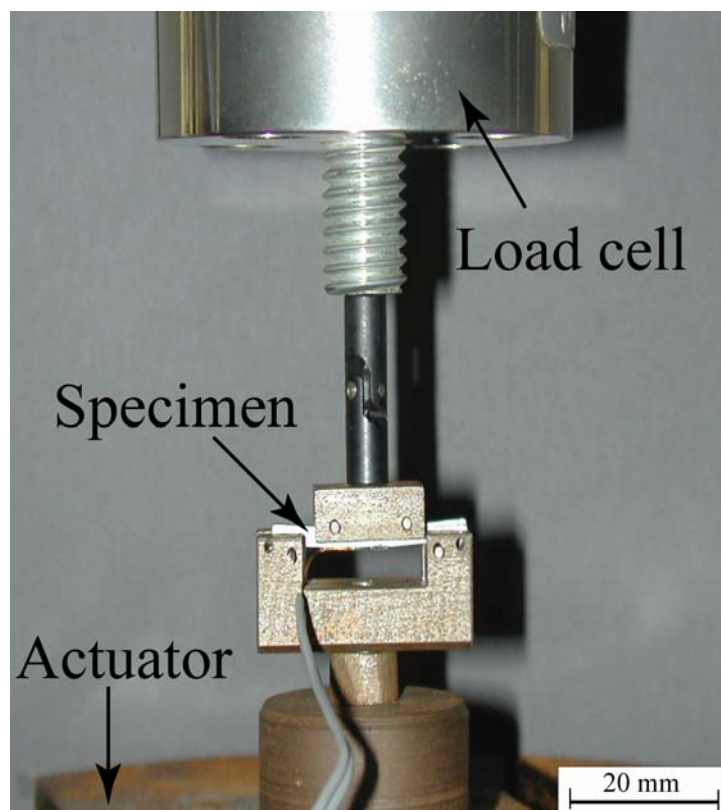


Fig. 2.7 Experimental setup

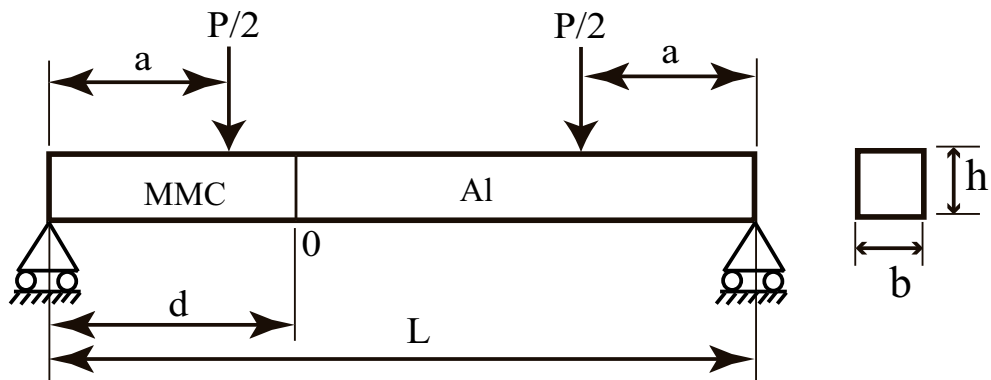


Fig. 2.8 Schematic illustration of four-point bending test

Additionally, the measured areas of dimple, interfacial debonding and particle/whisker fractures on the fracture surface were also examined. To determine the area fraction of particle/whisker fractures and interfacial debonding, we have selected a particular area 2 mm in width and 0.05 mm in height parallel and adjacent to the tensile surface. Therefore, the fraction of the particle and whisker fracture area is defined as the total particle and whisker fracture area divided by the total area measured. The area fractions of particle/matrix or whisker/matrix interfacial debonding were also measured by the same procedure.

References

- [1] Suresh, S., Mortensen, A. and Needleman, A. Fundamentals of metal matrix composites. London: Butterworth/Heinemann; 1993.
- [2] K. U. Kainer., Basic of Metal Matrix Composite, in Custom-made Materials for Automotive and Aerospace Engineering., 2006, WILEY-VCH Verlag GmbH and Co. KGaA, Weinheim.
- [3] D.B. Miracle., Metal matrix composite- From science to technological significance, *Composite Science and Technology*, Vol. 65 (2005), pp. 2526-2540
- [4] Zeuner, T., Stojanov, P., Sahm, P.R., Ruppert. H., and Engels A., Developing trends in disc brake technology for rail application, *Material Science and Technology*, Vol. 14 (1998), pp. 857-863.
- [5] S.M. Seyed Reihani: Processing of squeeze cast Al6061-30vol.% SiC composite and their characterization. *Material and Design*, Vol. 27, pp. 216-222, 2006.
- [6]. JIS H 5202, Aluminium alloy castings, in Japan Industrial Standard 2002.

Chapter 3: Experimental Results

3.1 Introduction

The aim of this chapter is to explain and discuss the experimental results in our research. The material is monotonically and cyclically deformed to failure at room temperature under four-point bending test. SEM observation of the fracture surfaces were made to describe the failure mechanism and EDX analysis was used to identify constituents on the fractured surfaces. Additionally, the measured areas of dimple, interfacial debonding and particle/whisker fractures on the fracture surface were also examined.

In section 3.2 we will present the experimental results of boundary effect on fracture mechanism under monotonic load condition. The fracture occurs in the reinforced part and the static fracture (monotonic loading) shows that the fracture mechanism is the combination of reinforcing particle fracture and interfacial debonding between reinforcing ceramics and metal matrix. In section 3.3 we will present the experimental results of boundary effect on fracture mechanism under cyclic load condition. Fatigue fracture is controlled by the fracture of coarse Al_2O_3 whisker. The critical location for fracture is changed by the external stress level. In section 3.4 we will present the whisker orientation effect on monotonic and fatigue strength. Whisker orientated parallel to the bending stress direction gives higher monotonic and fatigue strength in the composites. Finally a summery of experimental investigation is given in section 3.5.

3.2 Boundary effect on fracture mechanism under monotonic loading

In order to describe the boundary effect on fracture mechanism under monotonic loading, the experimental results of locally reinforced material ($\alpha = 90^\circ$) is discussed in this section.

The nominal bending stress and deflection curves measured by the four-point bending test of locally reinforced material ($\alpha = 90^\circ$) are shown in Fig.3.1. The curves exhibit the nonlinear relation between nominal bending stress and deflection under stress levels above 200 MPa. Fracture stresses and minimum distance from the fracture location to macroscopic boundary between reinforced part and unreinforced part under monotonic loading are given in Table 3. The average value of fracture stress is 298 MPa. All specimens are broken in the reinforced part. This is occurred because of high stiffness of reinforced part due to existence of reinforcement. Matching surface view of fractured specimen under monotonic loading is shown in Fig. 3.2. As indicated in Fig.3.2, 3.3 and Table 3, the fracture of locally reinforced samples occurs at the first or second closest SiC particle to the unreinforced part in the macroscopic boundary between reinforced part (MMC) and unreinforced part (aluminium alloy).

The matching halves of the sample fractured as a result of monotonic loading, which include the surface around the fracture initiation site (maximum tension site), are shown in Fig.3.4. Fractured particles/whiskers or debonded particles/whiskers are displayed on the fracture surface as well as microscopic dimples of matrix alloy.

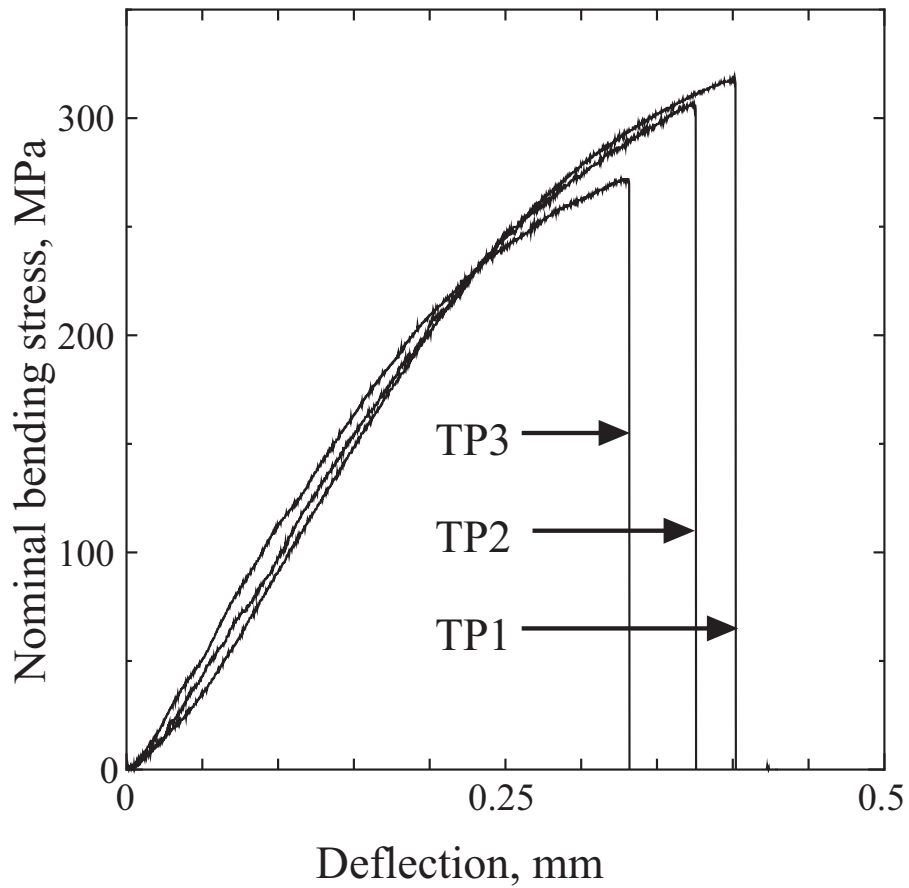


Fig.3.1 Nominal bending stress versus deflection curves under monotonic loading of locally reinforced material ($\alpha = 90^\circ$).

Table 3 Fracture stresses and minimum distance from the fracture location to macroscopic boundary between reinforced part and unreinforced part under monotonic loading of locally reinforced material ($\alpha = 90^\circ$).

Specimen	Fracture stress (MPa)	d_f
TP1	318	2 particles (46 μm)
TP2	306	1 particle (23 μm)
TP3	272	1 particle (23 μm)

d_f minimum distance from boundary to fracture site.

In Fig.3.4, the symbols indicated by P denote SiC particles which contain a lot of Si (99%) and a small amount of Al (1%) according to EDX analysis. A P-P pair in the matching halves, therefore, denotes a SiC particle fracture. The composition indicated by M contains a lot of Al (92%) and a small amount of Si (8%) which means the area is the Al cast alloy. Therefore, a P-M pair in the matching halves denotes SiC-particle/matrix interfacial debonding. The composition of the area indicated by W contains only Al (100%) which means the area is Al₂O₃. A W-M pair in the matching halves, therefore, denotes Al₂O₃-whisker/matrix interfacial debonding and the W-W pair in the matching halves denotes a Al₂O₃ whisker fracture. The area fractions of particle/whisker fracture and particle/matrix and whisker/matrix interfacial debonding under monotonic and cyclic loading conditions are listed in Table 4. The listed values in monotonic case are the average of the results for TP1, 2 and 3.

Table 4 Area fractions of SiC particle and Al₂O₃ whisker fracture and interface debonding between SiC particle-matrix and Al₂O₃ whisker-matrix under monotonic and cyclic loading condition

Load type	SiC particle		Al ₂ O ₃ whisker		Al (matrix) area (%)
	F (%)	D (%)	F (%)	D (%)	
Monotonic	10.5	10.1	0.85	9.3	69.25
Cyclic	1.9	19.0	0.85	8.9	69.35

F fracture area; D debonding area.

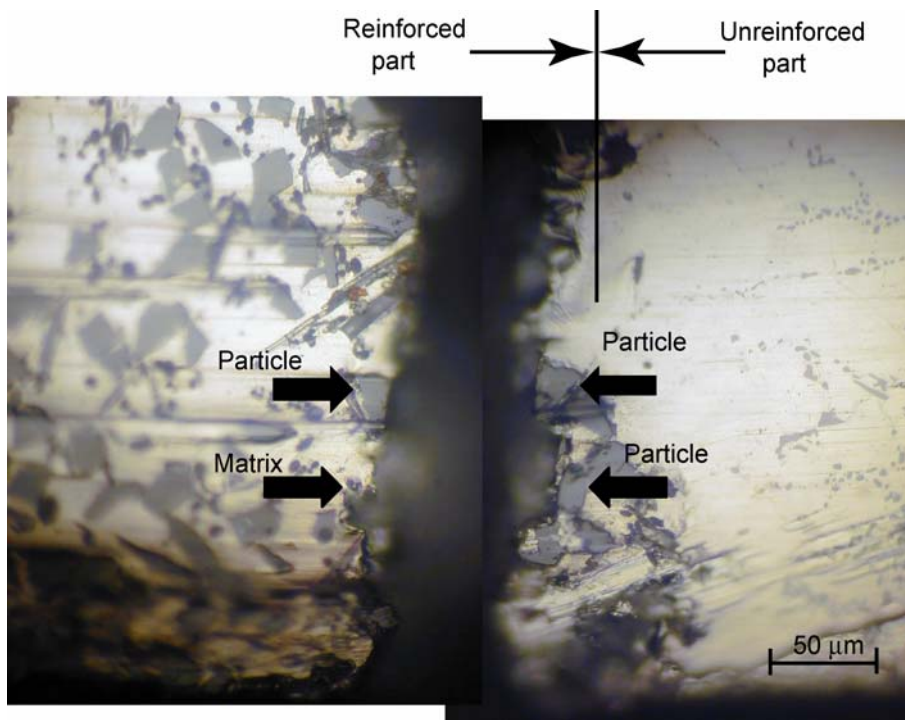


Fig.3.2 Matching surface view of fractured specimen ($\alpha = 90^\circ$) under monotonic loading, $\sigma_f = 272$ MPa

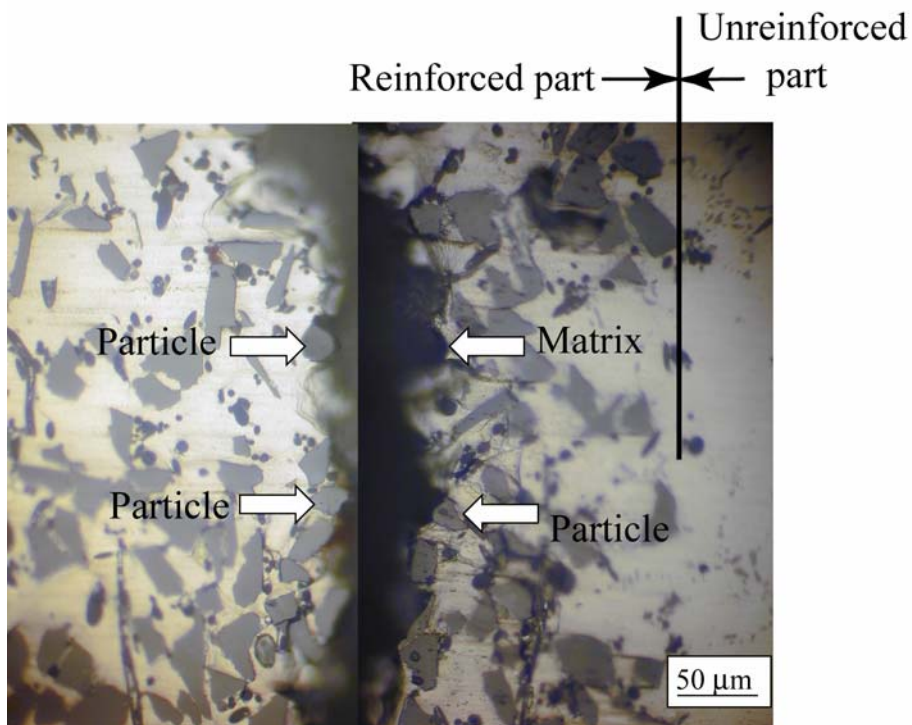


Fig.3.3 Matching surface view of fractured specimen ($\alpha = 90^\circ$) under monotonic loading, $\sigma_f = 318$ MPa

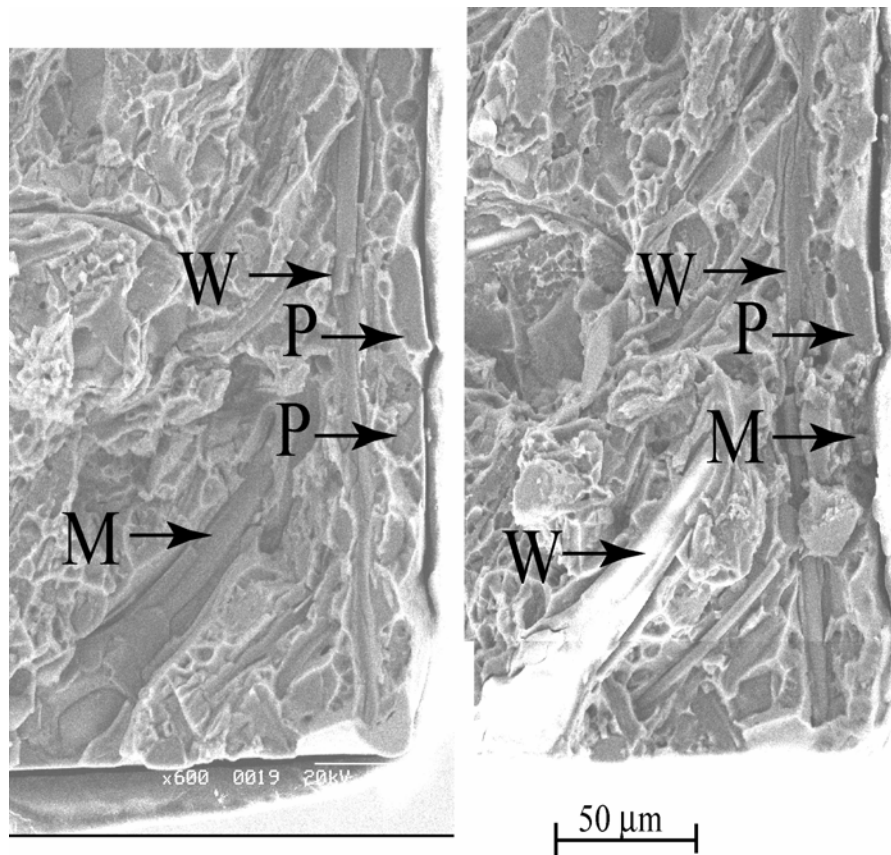


Figure.3.4 Matching fracture surface of locally reinforced material ($\alpha = 90^\circ$) under monotonic loading, $\sigma_f = 272$ MPa.

The area fractions of SiC particle fracture and the interfacial debonding of SiC particle/matrix and Al₂O₃ whisker/matrix are almost the same. From these results, it is clear that the fracture occurred in the particles as well as the particle/matrix interface and Al₂O₃ whiskers/matrix interface under monotonic loading condition. The local effective stress which is acting on the particle mainly controls the fracture characteristic of reinforcing particles. At the fracture stress under monotonic loading condition, the reinforcing particles and whiskers are deforming elastically within the plastically

deforming matrix alloy [1-5]. Thus, large strain mismatch occurs between these two materials. For this mismatch strain, a consequent concentration of stresses is generated in the particles and whiskers and on the interface between the reinforcing particles/whiskers and matrix alloy. These stresses may cause the separation of particle/whisker and Al matrix alloy or particle/whisker cracking.

3.3 Boundary effect on fracture mechanism under cyclic loading

In order to describe the boundary effect on fracture mechanism under cyclic loading, the experimental results of locally reinforced material ($\alpha = 90^\circ$) is discussed in this section.

The experimental results of fatigue life behavior of the samples of locally reinforced material ($\alpha = 90^\circ$) are shown in Fig.3.5. The horizontal arrow indicates the test that was suspended after 10^7 cycles. Fatigue fracture occurs under the maximum stress above one half of the monotonic fracture stress in the reinforced part. The experimental results of fatigue life and distance from fatigue fracture location to macroscopic boundary are given in Table 5.

As indicated in Table 5, when the maximum stress is low and the matrix alloy is deformed elastically in the reinforced part, (see the results of CTP4~8 in Table 5) the minimum distance of fracture location is far (0.28 ± 0.06 mm) from the boundary between the reinforced and unreinforced parts. In the monotonic bending test, the specimens are broken very close to the boundary (i.e., at the first or second particle closest to the unreinforced part, see Fig.3.2 and Table 3). In the fatigue test, when the

maximum stress is high, the specimens are also broken very close to the macroscopic boundary and in the reinforced part (see CTP1~3 in Table 5). This occurs when the matrix alloy in the reinforced part is deformed plastically within the elastically deformed reinforcement. The difference in the deformation state may be the cause of different fracture locations between the monotonic and cyclic loading.

After cyclic tests, the free surface (tension side) of the broken sample was observed and is shown in Fig.3.6 and Fig. 3.8. The cyclic fracture surface around the fatigue crack initiation site is shown in Fig.3.7 and Fig. 3.9. Fig.3.6 and Fig.3.7 are the corresponding tensile surfaces and fracture surfaces, respectively. Also Fig.3.8 and Fig.3.9 are the corresponding tensile surfaces and fracture surfaces, respectively

Table 5 Fatigue life and distance from fatigue fracture location to macroscopic boundary of locally reinforced material ($\alpha = 90^\circ$).

Specimen	σ_{\max} (MPa)	N_f	d_f
CTP1	261	517	2 particles (46 μm)
CTP2	225	3781	0.11 mm
CTP3	200	1.08×10^4	0.13 mm
CTP4	191	1.8×10^4	0.34 mm
CTP5	156	5.73×10^5	0.23 mm
CTP6	156	3.56×10^5	0.26 mm
CTP7	156	2.02×10^5	0.31 mm
CTP8	156	1.30×10^6	0.35 mm

d_f minimum distance from the boundary to fracture site;

σ_{\max} maximum stress; N_f number of cycle to failure.

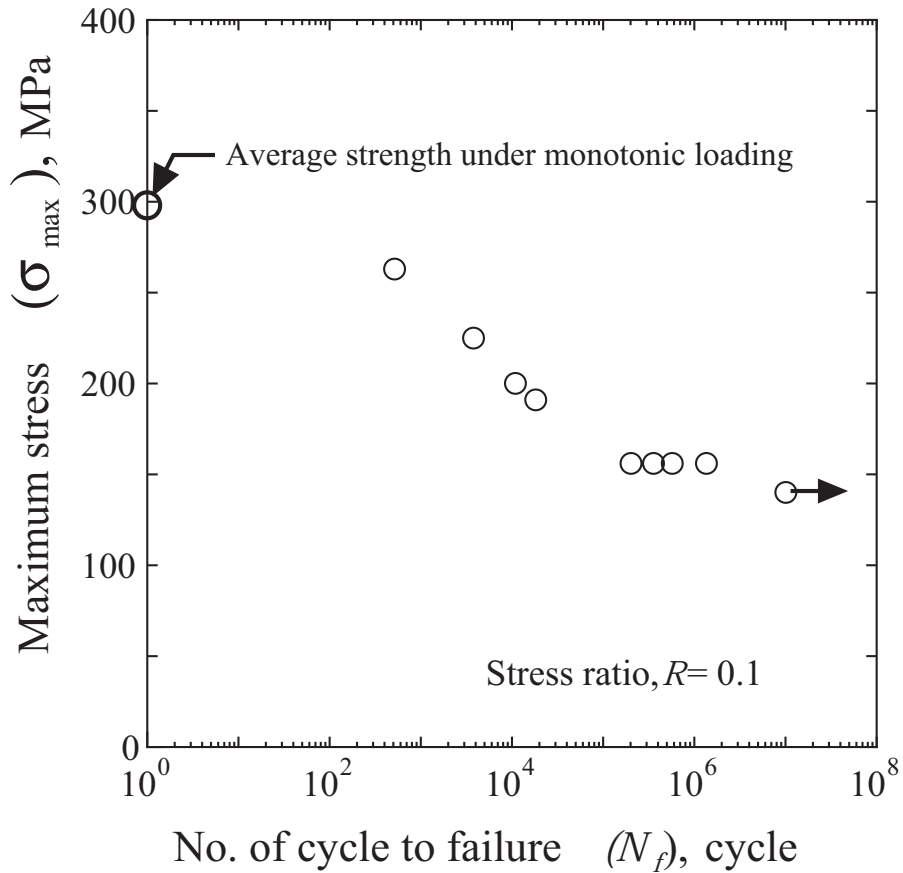


Fig. 3.5 Stress versus fatigue life behavior locally reinforced material

$(\alpha = 90^\circ)$ (stress ratio, $R=0.1$).

In Fig.3.6, Fig.3.7, Fig.3.8 and Fig.3.9, the areas indicated by W were areas that contained a lot of Al (99%) and a small amount of Si (1%) according to EDX analysis. Based on the color in the tensile surface image (Fig.3.6) and fracture surface morphology (Fig.3.7), a W-W pair in the matching halves can be assigned to an Al_2O_3 whisker fracture. The composition of the area indicated by M in Fig.3.6 and Fig.3.7 contains a lot of Al (92%) and a small amount of Si (8%). Therefore, the fatigue crack initiates from a coarse Al_2O_3 whisker fracture and propagates through the aluminium alloy matrix.

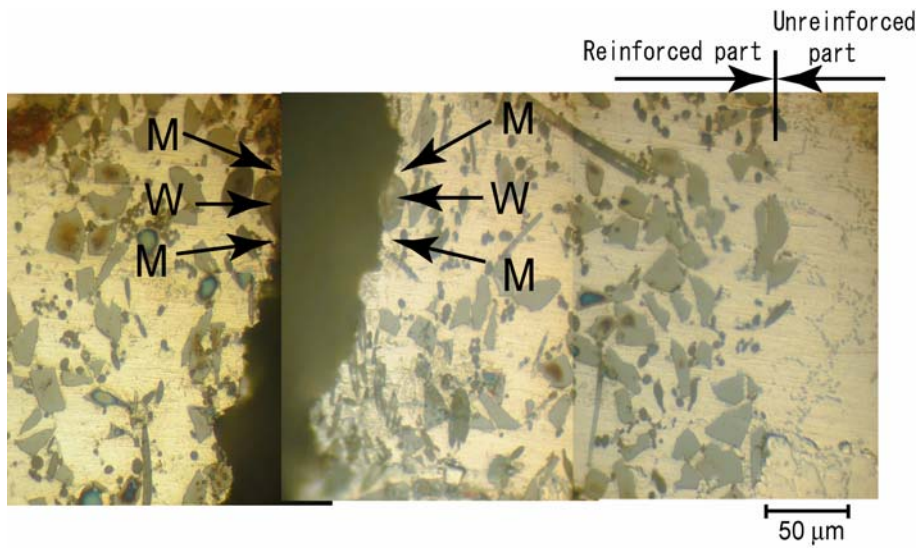


Fig. 3.6 Matching surface view of fatigue fractured specimen under cyclic loading,

maximum stress $\sigma_{\max} = 156 \text{ MPa}$, $N_f = 5.73 \times 10^5$.

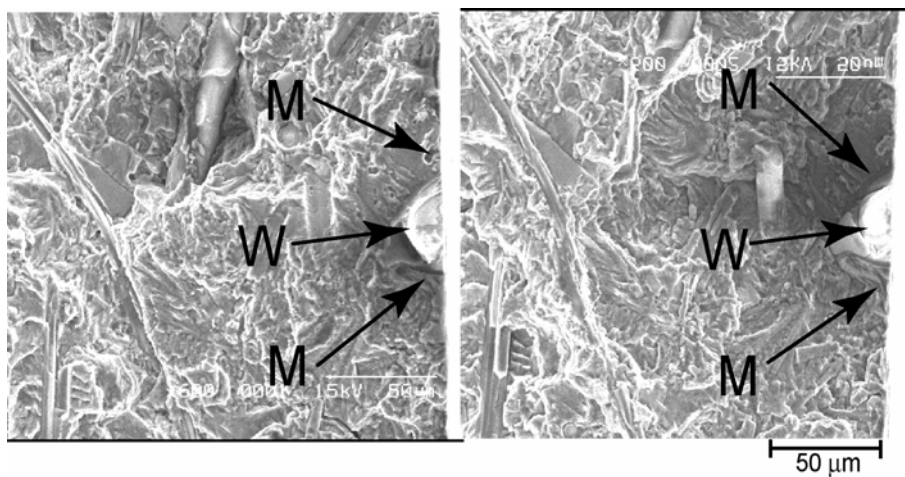


Fig.3.7 Matching fracture surface after fatigue fracture, maximum

stress $\sigma_{\max} = 156 \text{ MPa}$, $N_f = 5.73 \times 10^5$.

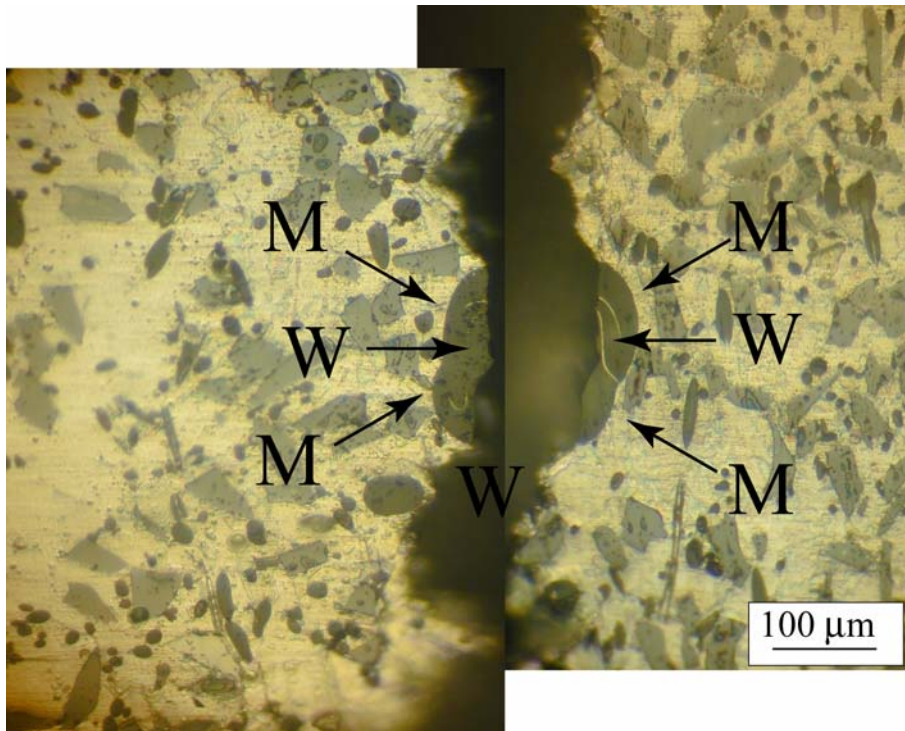


Fig. 3.8 Matching surface view of fatigue fractured specimen under cyclic loading,

maximum stress $\sigma_{\max} = 156 \text{ MPa}$, $N_f = 716$.

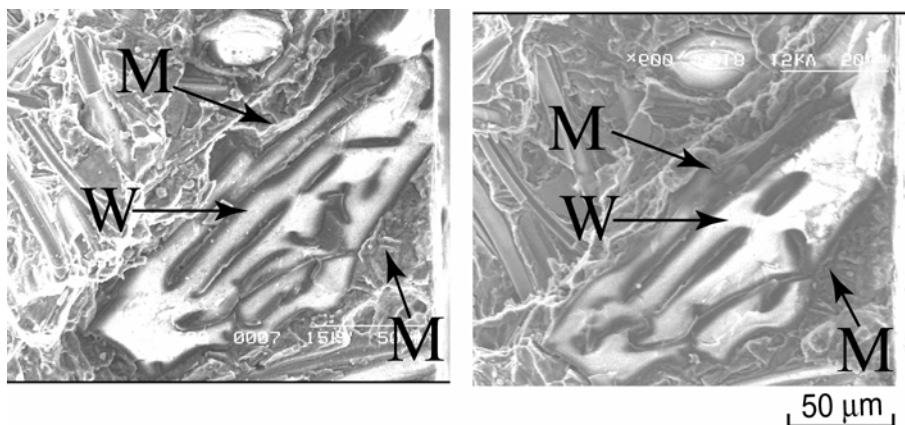


Fig.3.9 Matching fracture surface after fatigue fracture, maximum

stress $\sigma_{\max} = 156 \text{ MPa}$, $N_f = 716$.

The area fractions of SiC-particle/Al₂O₃-whisker fracture and interfacial debonding are measured by the same procedure as in the monotonic case and the average value of the results for CTP4 and CTP5 are indicated in Table 4. From Table 4, it can be seen that the fracture under the cyclic loading condition is dominated by particle/matrix interfacial debonding and whisker/matrix interfacial debonding. The fracture surfaces of broken specimens under monotonic and cyclic loading conditions show different fracture mechanisms. While the monotonic tests show that the fracture surface is dominated by the combination of particle fracture, particle/matrix interfacial debonding and whisker/matrix interfacial debonding, fatigue tests show that the fracture surface is dominated by particle/matrix interfacial debonding and whisker/matrix interfacial debonding. During the loading and unloading process in the cyclic deformation cyclic hardening is occur due to the accumulation of plastic strain. During the monotonic deformation the plastic strain also develop, especially at the interface between reinforcement and matrix is develop, but significantly lower than in cyclic deformation [6]. This might be one of the reason that the fatigue fracture dominated by the interfacial debonding.

3.4 Whisker orientation effect on monotonic and fatigue strength

In this section, the experimental results of whisker orientation effect on strength under monotonic and cyclic load are present. To describe these phenomena, the experimental results of both locally reinforced material ($\alpha = 90^\circ$) and homogeneous MMCs ($\alpha = 0^\circ \sim 90^\circ$) are discussed.

The nominal bending stress and displacement curves measured by the four-point bending test for homogeneous MMC and locally reinforced materials are shown in Fig.3.10. As indicate in Table 3 and Table 6 and Fig. 3.10, locally reinforced ($\alpha = 90^\circ$) and homogeneous ($\alpha = 0^\circ \sim 90^\circ$) samples exhibit a significant difference in strength. The results of locally reinforced material ($\alpha = 90^\circ$) in Fig. 3.10 are same as the results of Fig. 3.1. The average value of fracture stress of locally reinforced material ($\alpha = 90^\circ$) was 298 MPa are less than the scatter band of the value for homogeneous MMC ($\alpha = 0^\circ \sim 90^\circ$) which was 364 MPa. The whisker orientation in the MMC may be the cause of low bending strength of the locally reinforced material ($\alpha = 90^\circ$). Whiskers oriented parallel ($\alpha = 90^\circ$) to the bending stress direction give higher monotonic strength of homogeneous MMC ($\alpha = 0^\circ \sim 90^\circ$). The experimental results of fatigue life behavior of homogeneous MMC and locally reinforced material are shown in Fig.3.11. The horizontal arrows indicate the tests that were suspended after 10^7 cycles. The results of locally reinforced material ($\alpha = 90^\circ$) in Fig. 3.11 are same as the results of Fig. 3.5. From Table 5 and Table 7 and Fig. 3.11, it can be seen that the fatigue strength of locally reinforced material ($\alpha = 90^\circ$) is lower than the fatigue strength of homogeneous MMC ($\alpha = 0^\circ \sim 90^\circ$). The whisker orientation in the MMC may be the cause of low fatigue strength of locally reinforced material ($\alpha = 90^\circ$). Whiskers randomly oriented relative to the bending stress direction cause longer fatigue life of homogeneous MMC ($\alpha = 0^\circ \sim 90^\circ$).

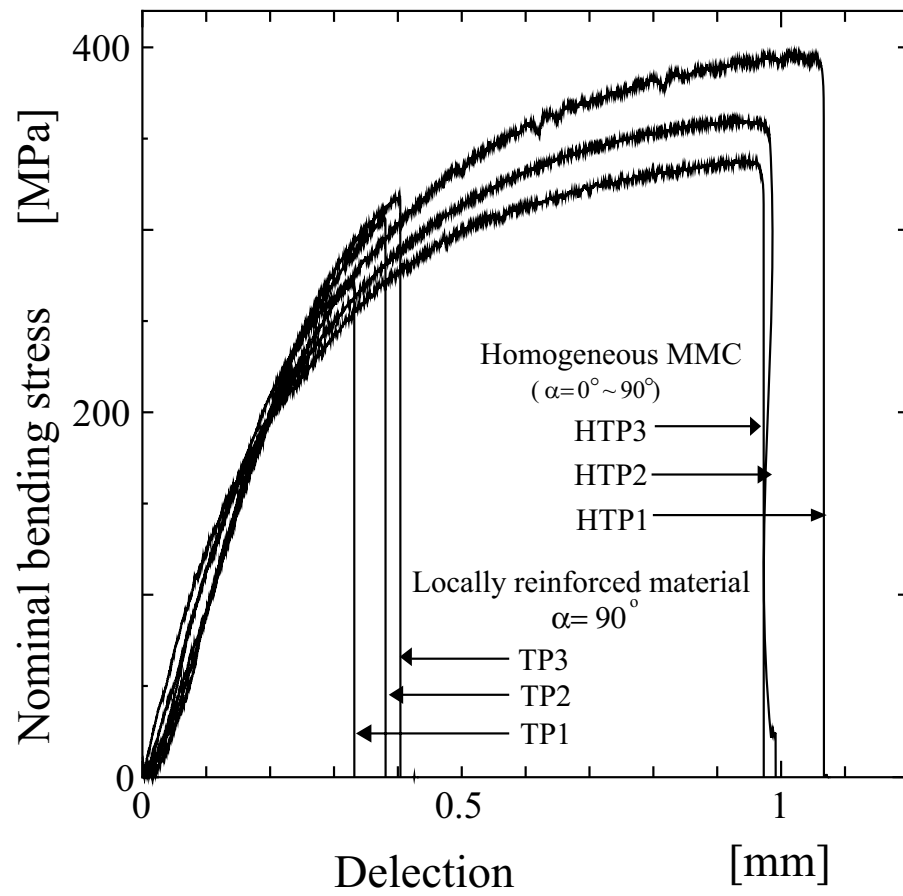


Fig.3.10 Nominal bending stress versus deflection curves under monotonic loading.

Table 6 Fracture stresses under monotonic loading of homogeneous MMC ($\alpha = 0^\circ \sim 90^\circ$).

Specimen	Fracture stress (MPa)
HTP1	394
HTP2	359
HTP3	337

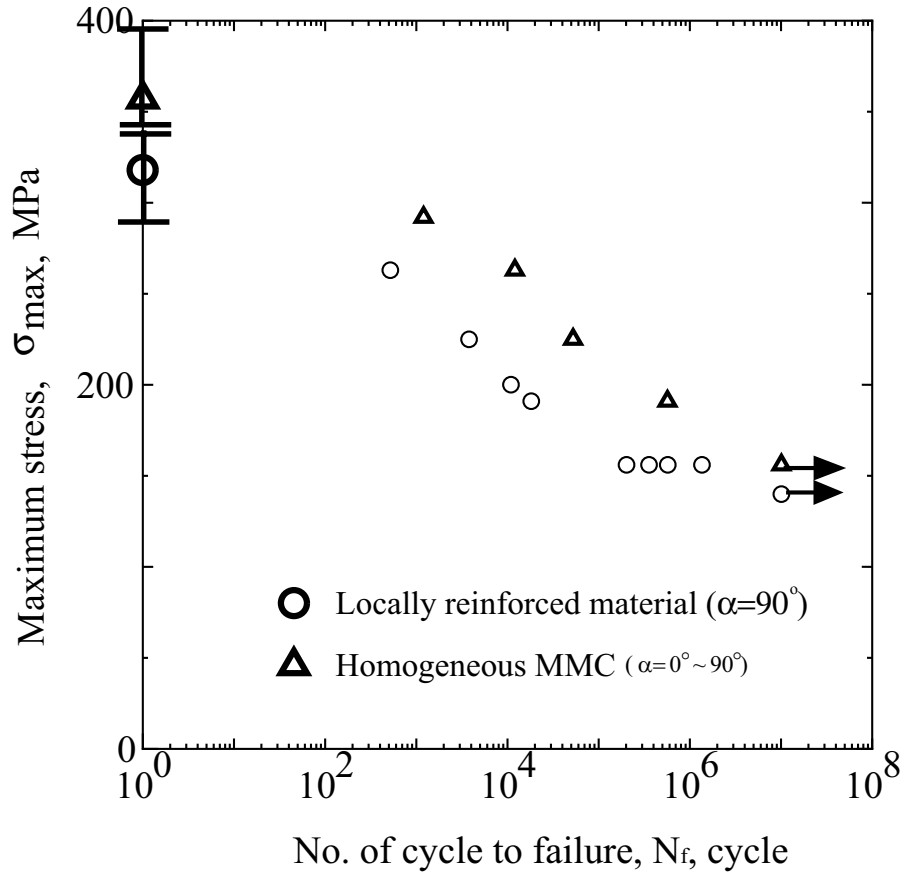


Fig.3.11 Stress versus fatigue life behavior (stress ratio, $R=0.1$), the plots on $N_f=0$ show average strength under monotonic load.

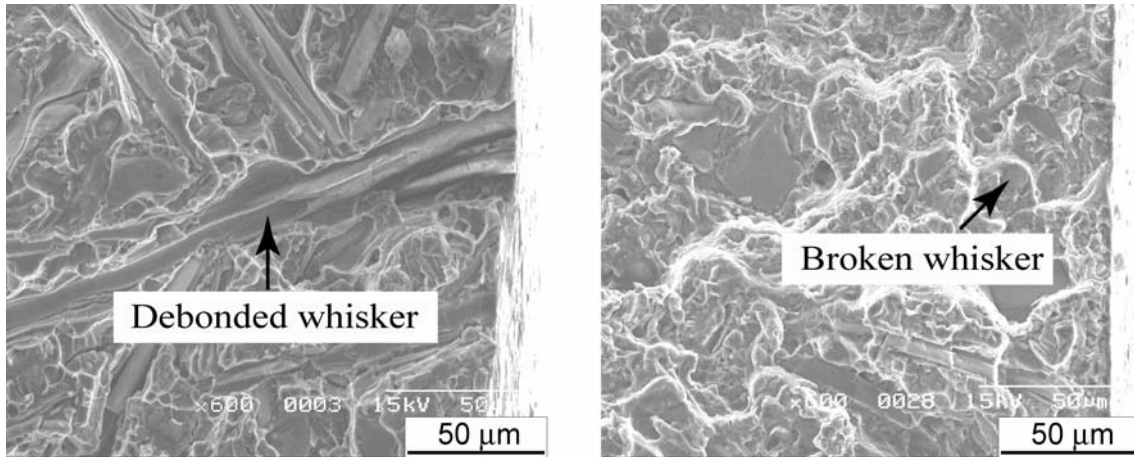
Table 7 Fatigue life of homogeneous MMC ($\alpha = 0^\circ \sim 90^\circ$).

Specimen	σ_{max} (MPa)	N_f
HCTP1	292	1200
HCTP2	261	12060
HCTP3	225	5.24×10^4
HCTP4	191	6.67×10^4
HCTP5	191	5.6×10^5
HCTP6	156	1×10^7

σ_{max} maximum stress; N_f number of cycle to failure

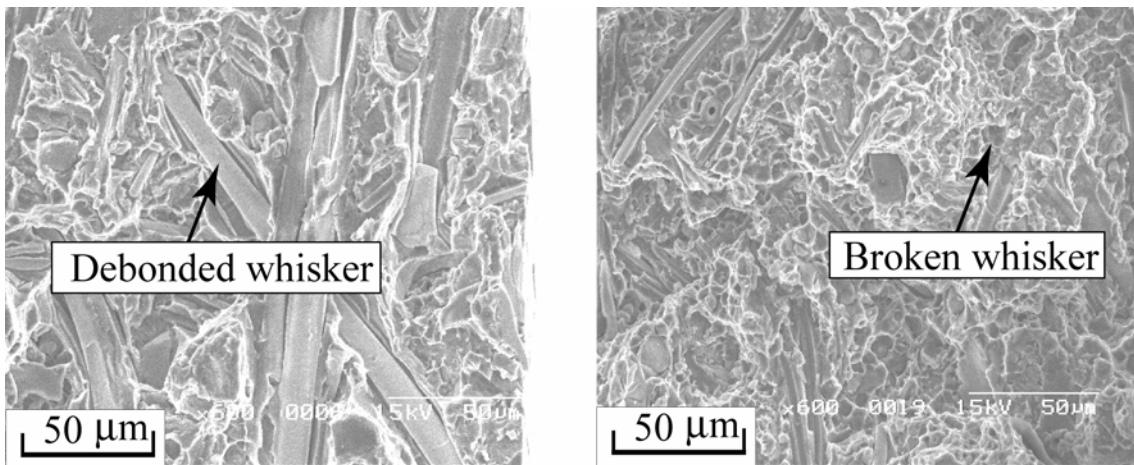
To clarify the fracture mechanism, fracture surfaces were examined in SEM and the characteristics of the fracture surface were described as follows: The characteristic fracture surface of locally reinforced material under cyclic loading condition ($\alpha = 90^\circ$) is shown in Fig. 3.12 (a) and monotonic loading condition is shown in Fig. 3.13 (a). There were many transversely debonding whiskers parallel to the fracture surface. The broken whiskers in the fracture surface were scarce. The whiskers pulled-out could not be seen in the fracture surface.

Area fractions of SiC particle and Al₂O₃ whisker fracture and interface debonding between SiC particle-matrix and Al₂O₃ whisker-matrix of locally reinforced material ($\alpha = 90^\circ$) and homogeneous MMC ($\alpha = 0^\circ \sim 90^\circ$) under cyclic and monotonic loading conditions are shown in Table 8 and Table 9. The results of locally reinforced material ($\alpha = 90^\circ$) in Table 8 and Table 9 are the same as the results of Table 4. As listed in Table 8 and Table 9, large area fractions of interfacial debonding of Al₂O₃ whisker/matrix are observed in locally reinforced materials and the area fractions of Al₂O₃ whisker fracture are negligible under monotonic and cyclic loading condition. From the above observation it is pointed out that when whisker direction is perpendicular ($\alpha = 90^\circ$) to the stress direction, almost all whiskers are transversely debonded, that means the lower strength and shorter fatigue life of locally reinforced material ($\alpha = 90^\circ$) is corresponding to the interface debonding between whisker-matrix interfaces.



(a) Locally reinforced material ($\alpha = 90^\circ$) (b) Homogeneous MMC ($\alpha = 0^\circ \sim 90^\circ$)

Fig 3.12 Comparison of two types of fracture surface (a) locally reinforced material ($\alpha = 90^\circ$) [CTP5] (b) Homogeneous MMC ($\alpha = 0^\circ \sim 90^\circ$) [HCTP4], under cyclic loading condition (Observed locations are near the tensile side)



(a) Locally reinforced material ($\alpha = 90^\circ$) (b) Homogeneous MMC ($\alpha = 0^\circ \sim 90^\circ$)

Fig 3.13 Comparison of two types of fracture surface (a) locally reinforced material ($\alpha = 90^\circ$) [TP1] (b) Homogeneous MMC ($\alpha = 0^\circ \sim 90^\circ$) [HTP1], under monotonic loading condition (Observed locations are near the tensile side)

The characteristic fracture surface of homogeneous MMC ($\alpha = 0^\circ \sim 90^\circ$) under monotonic loading condition is shown in Fig. 3.12 (b) and under cyclic loading condition is shown in Fig 3.13 (b). There were many dimples and broken whiskers in the fracture surface. The transversely debonding whiskers parallel to the fracture surface are scarce. The whiskers pulled-out could not be seen in the fracture surface.

As listed in Table 8 and Table 9, large area fractions of Al_2O_3 whisker fracture are observed and the area fractions of interfacial debonding of Al_2O_3 whisker/matrix are negligible. This means whisker-matrix interface is strong enough to avoid whisker pull out in this whisker orientation. Load is transferred from matrix to the whisker and whisker fractures dominate the fracture mechanism. This is one of the reasons why the monotonic strength and fatigue strength of homogeneous MMC is higher than that of locally reinforced material. As indicated in Table 8 and Table 9, the area fractions of SiC particle fracture and the interfacial debonding of SiC particle/matrix are almost the same for the both materials.

Table 8 Area fractions of SiC particle and Al_2O_3 whisker fracture and interface debonding between SiC particle-matrix and Al_2O_3 whisker-matrix under cyclic loading conditions

Material	SiC particle		Al_2O_3 whisker		Al (matrix) area (%)
	F ^a (%)	D ^b (%)	F ^a (%)	D ^b (%)	
Homogeneous MMC ($\alpha = 0^\circ \sim 90^\circ$)	1.9	20.6	11	0.1	69.0
Locally reinforced material ($\alpha = 90^\circ$)	1.9	19.0	0.85	8.9	69.35

^a F fracture area, ^b D debonding area

Table 9 Area fractions of SiC particle and Al₂O₃ whisker fracture and interface debonding between SiC particle-matrix and Al₂O₃ whisker-matrix under monotonic loading conditions

Material	SiC particle		Al ₂ O ₃ whisker		Al (matrix) area (%)
	F ^a (%)	D ^b (%)	F ^a (%)	D ^b (%)	
Homogeneous MMC ($\alpha = 0^\circ \sim 90^\circ$)	2.9	19.6	9.8	0.8	66.9
Locally reinforced material ($\alpha = 90^\circ$)	10.5	10.1	0.85	9.3	69.25

^a F fracture area, ^b D debonding area

In order to characterize the fracture initiation, fracture surfaces were examined in SEM and EDX and the characteristics of the fracture initiation were described as follows: The cyclic fracture surface of homogeneous MMC ($\alpha = 0^\circ \sim 90^\circ$) (specimen HCTP4 in Table 5) around the fatigue crack initiation site is shown in Fig.3.14. In Fig.3.14, the areas indicated by W were areas that contained a lot of Al (99%) and a small amount of Si (1%) according to EDX analysis. Therefore, a W-W pair in the matching halves can be assigned to a Al₂O₃ whisker fracture. The composition of the area indicated by M in Fig. 3.14 contains a lot of Al (92%) and a small amount of Si (8%). Therefore, the fatigue crack initiates from a coarse Al₂O₃ whisker fracture and propagates through the aluminium alloy matrix. As shown in Fig. 3.7 and Fig.3.9, in the locally reinforced material ($\alpha = 90^\circ$) the fatigue crack also initiates from a coarse Al₂O₃ whisker fracture and propagates through the aluminium alloy matrix. Thus, the fatigue crack initiation process is independent on the whisker orientation such that a coarse Al₂O₃ whisker

fracture is the origin and the crack propagates through the aluminium alloy matrix.

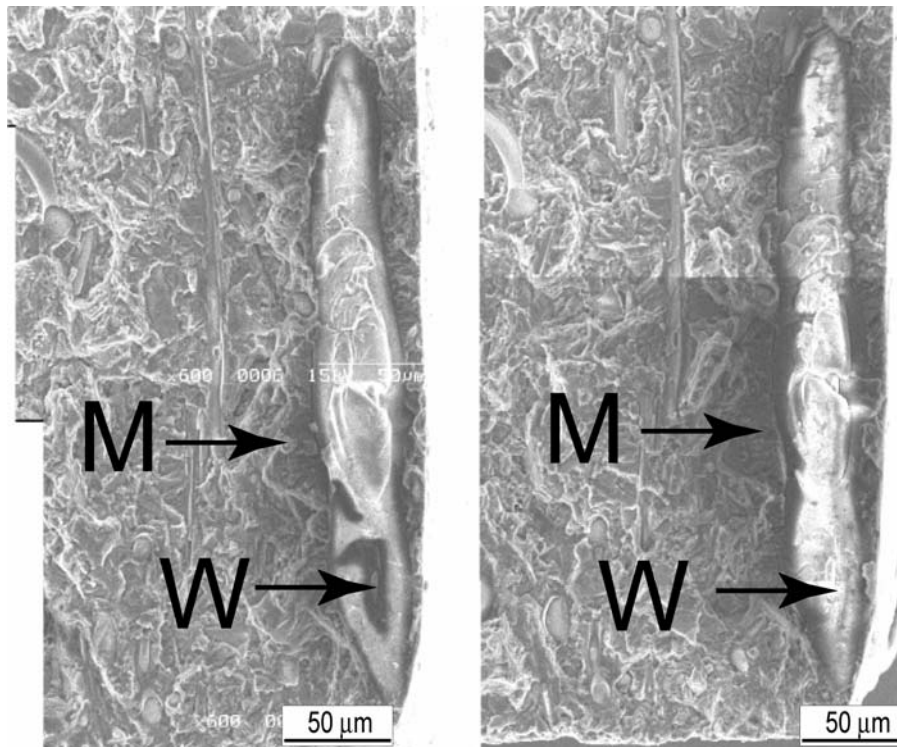


Fig.3.14 Matching fatigue fracture surface of homogeneous MMC ($\alpha = 0^\circ \sim 90^\circ$)

after fatigue fracture $\sigma_{\max} = 191 \text{ MPa}$, $N_f = 6.67 \times 10^4$

3.5 Summery

In this chapter the experimental results were presented, which include the the monotonic and cyclic fracture behavior, boundary effect between reinforced and unreinforced part, and whisker orientation effect on overall strength of an aluminium cast alloy, locally reinforced by SiC particles and Al₂O₃ whiskers. The research was concentrated on the fracture mechanism and fracture location of locally reinforced material fractured and whisker orientation effect on strength under monotonic and

cyclic loads. The following results are the key findings:

1. The fracture occurs in the reinforced part under both monotonic and cyclic loads.
2. The stress-deflection curves under monotonic load exhibit the nonlinear relation under stress levels above 200 MPa.
3. Under cyclic load, the fracture is dominated by interfacial debonding of particle-matrix and whisker-matrix interfaces, whereas, under monotonic load, the fracture is dominated by both particle fracture and particle/whisker-matrix interfacial debonding. During the loading and unloading process in the cyclic deformation cyclic hardening is occur due to the accumulation of plastic strain. During the monotonic deformation the plastic strain also develop, especially at the interface between reinforcement and matrix is develop, but significantly lower than in cyclic deformation [6]. This might be one of the reason that the fatigue fracture dominated by the interfacial debonding.
4. Under cyclic loading when the maximum stress is low and the matrix alloy is deformed elastically in the reinforced part, the minimum distance of fracture location is far (0.28 ± 0.06 mm) from the boundary between the reinforced and unreinforced parts. In the monotonic bending test, the specimens are broken very close to the boundary (i.e, at the first or second particle closest to the unreinforced part). In the fatigue test, when the maximum stress is high, the specimens are also broken very close to the macroscopic boundary and in the reinforced part. This occurs when the matrix alloy in the reinforced part is deformed plastically within the elastically deformed reinforcement. The difference in the deformation state may be the cause of different fracture locations between the monotonic and cyclic loading.
5. From the fracture surface analysis (SEM and EDX), fatigue crack initiates from a

coarse Al_2O_3 whisker fracture and propagates through the aluminium alloy matrix. Under monotonic loading, coarse Al_2O_3 whisker was not found in crack initiation site.

6. The monotonic and fatigue strength of locally reinforced material ($\alpha = 90^\circ$) is lower than the strength of homogeneous MMC ($\alpha = 0^\circ \sim 90^\circ$). Whisker orientation effect gives lower monotonic and fatigue strength of locally reinforced material ($\alpha = 90^\circ$). Whiskers randomly oriented relative to the bending stress direction cause higher strength and longer fatigue life of homogeneous MMC ($\alpha = 0^\circ \sim 90^\circ$).
7. There were many transversely debonding whiskers parallel to the fracture surface on the characteristic fracture surface of locally reinforced material ($\alpha = 90^\circ$). Broken whiskers were scarce and whiskers pulled-out could not be seen. The fracture surface is dominated by interfacial debonding of Al_2O_3 whisker/matrix according to the area fraction results. The transversely debonded whisker gives the lower strength and shorter fatigue life of locally reinforced material ($\alpha = 90^\circ$) which is corresponding to the interface debonding between whisker-matrix interfaces.
8. There were many dimples and broken whiskers in the fracture surface of homogeneous MMC ($\alpha = 0^\circ \sim 90^\circ$). Debonding whiskers are scarce and whiskers pulled-out could not be seen in the fracture surface. Whisker fractures dominate the fracture mechanism and give the higher strength and longer fatigue life of homogeneous MMC ($\alpha = 0^\circ \sim 90^\circ$). This is one of the reasons why the monotonic strength and fatigue strength of homogeneous MMC is higher than that of locally reinforced material.

References

- [1] AL. Chen, Y. Arai and E. Tsuchida: An experimental study on effect of thermal cycling on monotonic and cyclic response of cast aluminum alloy-SiC particulate composites. *Composites Part B.*, Vol. 36 (2005), pp. 319-330.
- [2] T.S. Srivatsan and M. Al-Hajiri: The fatigue and final fracture behavior of SiC particle reinforced 7034 aluminum matrix composites., *Composite Part B.*, Vol. 33 (2002), pp. 391-404.
- [3] Q. Zhang, H. Zhang, Gu. Mingyuan and J. Yanping: Studies on the fracture and flexural strength of Al/Si_p composite. *Materials Letters.* Vol. 58 (2004), pp. 3545-3550.
- [4] M. Levin and B. Karlsson: Influence of SiC particle distribution and prestraining on fatigue crack growth rates in aluminum AA 6061-SiC composite *Material Science and Technology*, Vol. 7 (1991), pp. 596-607.
- [5] D. L. Davidson: Fatigue and fracture toughness of aluminum alloys reinforced with SiC and alumina particles *Composite.*, Vol. 24 (1993), pp. 248-255.
- [6] P. Poza and J. Llorca: Mechanical behavior and failure micromechanisms of Al/Al₂O₃ composites under cyclic deformation. *Metallurgical and materials Transaction A*: Vol. 26A, pp. 3131-3141, 1995.

Chapter 4: Numerical Study of Fracture Mechanism, Boundary Effect and Whisker Orientation Effect

4.1 Introduction

To understand and characterize mechanical properties and performance of metal matrix composite such as mechanisms of strengthening and of microscopic damage and failure, many researchers have made use of the computational and analytical method in the past many years [1-15]. To investigate the monotonic and cyclic deformation behavior of MMCs, a large number of finite element analyses have been carried out by using unit cell modeling approach [1-4]. Some of the studies concerned with the effect of particle size, shaped and distribution on mechanical performance of MMCs by using multi particle unit cell model [5]. Cubic shaped inclusions in a 3D unit cell model were used for describing the particle distribution effect in MMCs [6-8]. The influence of the aspect of particle shape, size and distribution on ductility of SiC particulate MMC has been successfully predicted by using periodic 3D unit cell concept [6]. All of the above works were concentrated on failure mechanism and particle size and distribution effect on mechanical performance of MMCs. Some numerical studies have shown that a significant level of hydrostatic stresses develop in the composite matrix due to constrained plastic flow [5-7]. Different level of plastic flow control the basic failure mechanism of metal matrix composites such as matrix void nucleation, growth and coalescence, reinforcement fracture and interface debonding between matrix and

reinforcement.

By using finite element method a great deal of research has addressed the fiber/whisker orientation effect on elastic properties and overall strength of the composites, especially for the randomly oriented fiber composite [11-15]. These numerical results have shown that the strength of the composite is strongly influenced by the distribution of the reinforcement. The strength of MMCs is greatly influenced by stress transfer between short fiber/whisker and the matrix alloy. These phenomena have already been investigated by 3D finite element studies [13, 15]. The whisker direction and interfacial bond has a remarkable effect on stress transfer between matrix and reinforcement. Good interfacial bonding enhances the stress transfer between matrix and reinforcement which results increase of the overall strength of composites [13].

The aim of this chapter is to investigate the stress distribution around the boundary between reinforced and unreinforced part based on 2-D inclusion array model considering the microscopic inhomogeneous effects. It is evident that the adopted 2-dimensional model cannot capture the precise 3-dimensional characteristics of the real material quantitatively. However by using 2-D periodic cell models with realistic microstructural arrangements within the cell, many researchers have successfully predicted the key of failure mechanism (particle fracture, debonding and matrix void nucleation) of composites [1-5]. There is only limited study on 3-D inclusion model which were used for describing the reinforcement effect on strength, ductility and fracture mechanism in MMCs [6-8]. The failure mechanisms have been predicted successfully by 2D studies [3, 4]. Those are qualitatively same as 3D studies [6, 7] which show stress distribution developed around and within hard particles in plastically

deforming matrix. The stress causes particle fracture or interfacial debonding. The best of our knowledge, there is no numerical investigations have been conducted to evaluate the boundary problem between reinforced and unreinforced part in the composite. To evaluate the boundary effect between reinforced and unreinforced part in the MMCs unit cell and periodic boundary condition is not a suitable method. In this analysis a real microstructure in the reinforced part is modeled by many 2D unit cells (20×12 unit cell) and each unit cell includes one circular reinforcement material surrounded by the matrix alloy. The calculation size of a 3D ideal array of circular inclusions which consists large number of unit cell is very large and almost impossible to carry. Thus, in this research using an elastic-plastic 2D finite element method (FEM), the effect of boundary between reinforced and unreinforced part on stress distribution are investigated. With this model we successfully predicted the stress distribution at the maximum tension site (maximum stress at particle or interface) and strain amplitude qualitatively.

This chapter also concerned with the study of whisker orientation effect on strength in the composite. To details understanding the reinforcement orientation effect in the composite precise 3-dimensional characteristics is necessary. It is evident that, only 3D model can show the reinforcement orientation effect in the composite rather than 2D model [12]. Therefore, the whisker orientation effect on overall strength in the composite based on 3D single whisker unit cell model was presented in this current research. However, the whisker orientation and the hybrid (reinforced by whisker and particle) effect on overall strength are still unsolved problem in the hybrid composites. Therefore, to describe the hybrid effect of the composites, a three-dimensional hybrid (particle and whisker) unit cell model is also conducted in this work.

4.2 Numerical model

To contribute to a better understanding of the stress distribution near the macroscopic boundary between the reinforced part and unreinforced part, a two-dimensional modeling was conducted using the finite element method (FEM). Finite element calculations were carried out under the plane strain condition. Fig. 4.1(a) shows a schematic illustration of a macroscopic model and Fig 4.1(b) shows finite element mesh used in this model. Eight node isoparametric element of size $25\mu m \times 11\mu m$ was used around the boundary in this model. The reinforced part (MMC) and unreinforced part (Al alloy) are assumed to be homogeneous in the macroscopic model. The boundary between MMC and Al alloy is set at $y=0$. Elastic properties used in this model are listed in Table 10. To evaluate the elastic constant, yield strength and hardening behavior of MMC, we used an infinite periodic circular inclusion array model is shown in Fig. 4.2 [2]. The yield strength and hardening properties of Al alloy and MMC predicted by the infinite periodic circular inclusion array model are listed in Table 11. We use a sub-modeling concept to consider the effect of microscopic inhomogeneity on the stress field around the boundary between the reinforced part and unreinforced part. We refer to this model as the “inclusion array model”. The schematic illustration of this inclusion array model is shown in Fig.4.3 (a). Finite element mesh used in this inclusion array model is shown in Fig. 4.3 (b). Eight node isoparametric element of size $2.3\mu m \times 4.6\mu m$ and three node fixed distortion element were used in this model. To evaluate the stress concentration in and around the reinforced particles and whiskers, a real microstructure in the reinforced part is modeled by an ideal array of circular inclusions.

Table 10 mechanical properties of materials

Parameters	Al ₂ O ₃	SiC	AC4CH alloy	MMC
Young's Modulus (GPa)	380	450	70.0	142
Poisson's ratio	0.27	0.20	0.33	0.28
Yield strength (MPa)	-	-	131	166

The reinforced part consists of many unit cells and each unit cell includes one circular reinforcement material surrounded by the matrix alloy (Fig.4.3). The matrix alloy in the reinforced part is of the same composition as the alloy in the unreinforced part. The

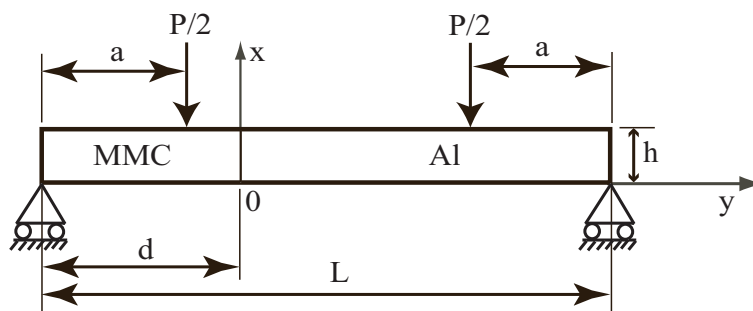
inclusion array model boundaries $\left\{0 \leq x \leq h_s, y = -\frac{L_s}{2}\right\}, \left\{0 \leq x \leq h_s, y = \frac{L_s}{2}\right\}$

and $\left\{x = h_s, -\frac{L_s}{2} \leq y \leq \frac{L_s}{2}\right\}$ in Fig.4.3 are derived by displacement fields of the

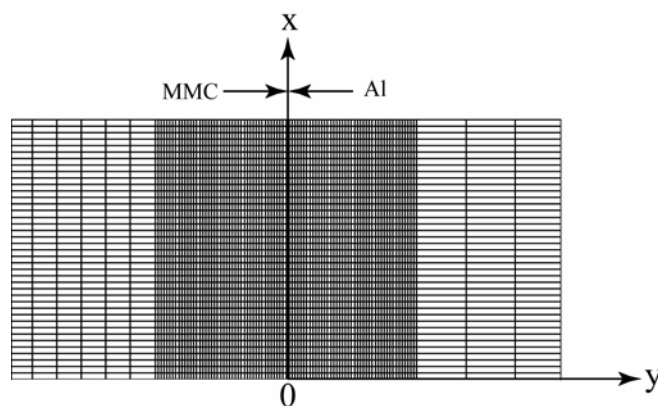
macroscopic model results. The nonlinear stress-strain relation of AC4CH aluminium alloy was obtained from the reference [2]. The boundary between the inclusion array part and the unreinforced Al part is set at $y=0$. The model adopted assumes that the circular inclusions only deform elastically while the matrix deforms elastically or elasto-plastically depending on the local effective stress level. Geometry of the numerical model is listed in Table 12.

Table 11 Flow stresses predicted by the model

Plastic strain (ε_p)	Unreinforced part Flow stress (σ_f), MPa	Reinforced part Flow stress (σ_f), MPa
0.00	131	166
0.0025	133	185
0.005	137	210
0.0075	139	219
0.001	142	231
0.0015	148	249
0.0017	150	256



(a)



(b)

Fig.4.1 Global model of homogeneous materials joint (a) model illustration (b) finite-element mesh.

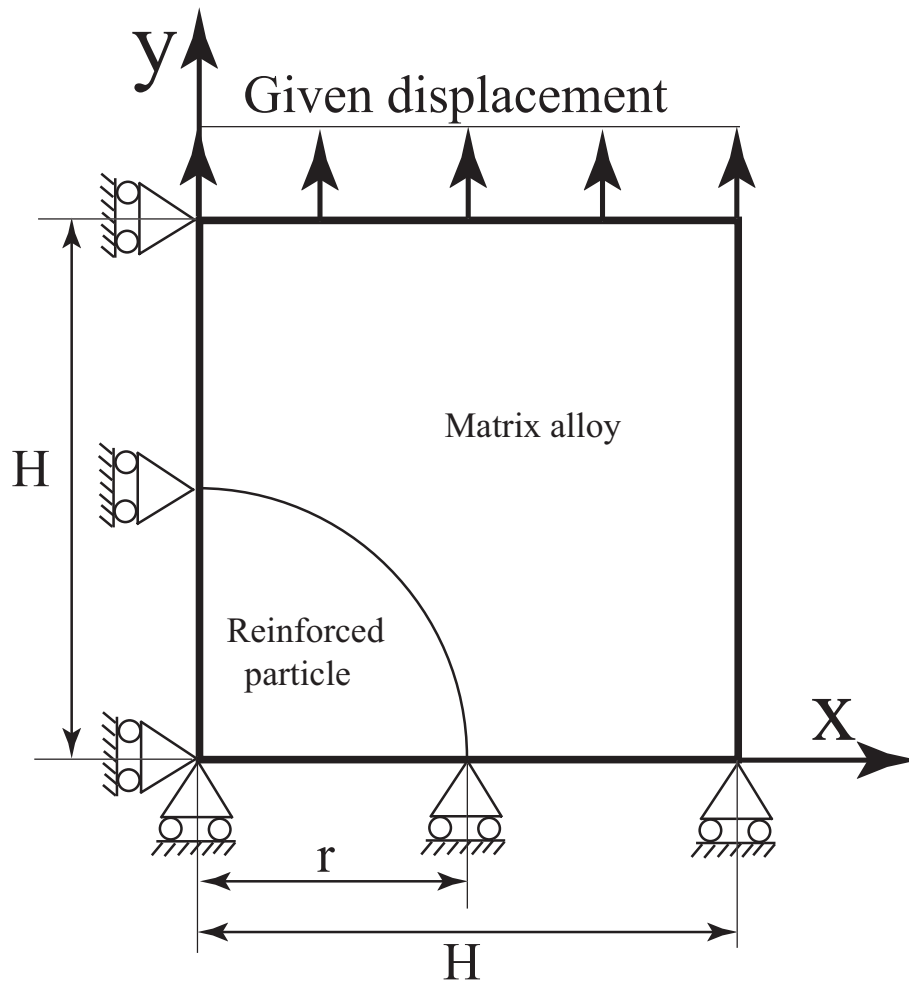
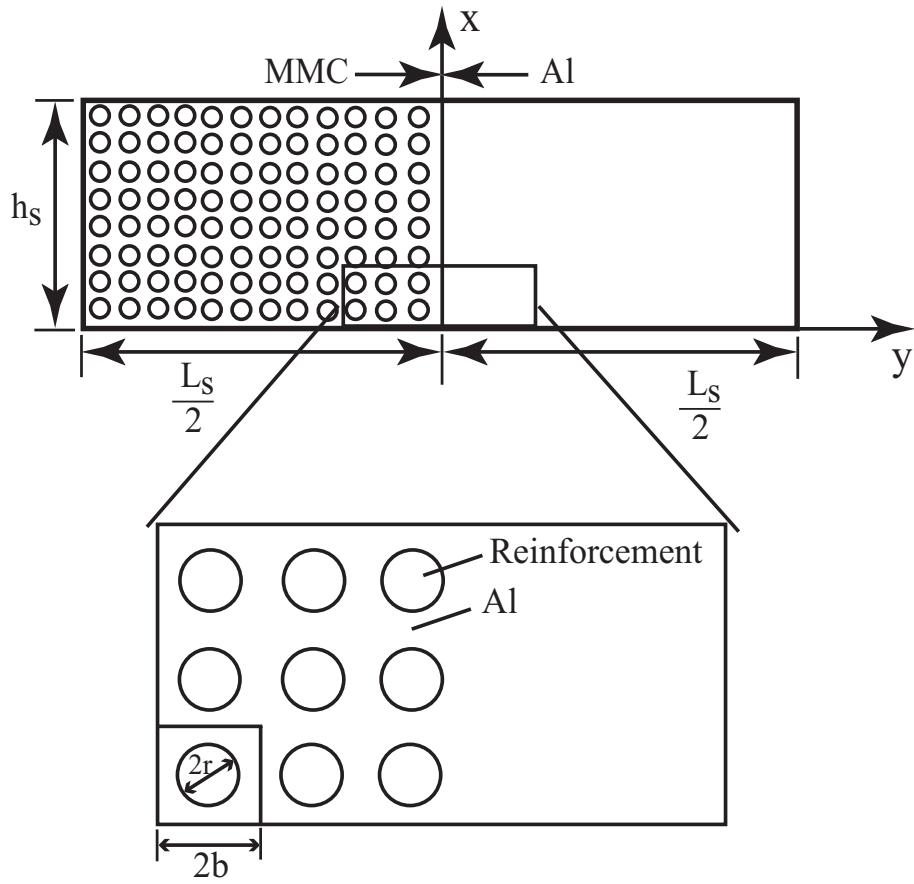


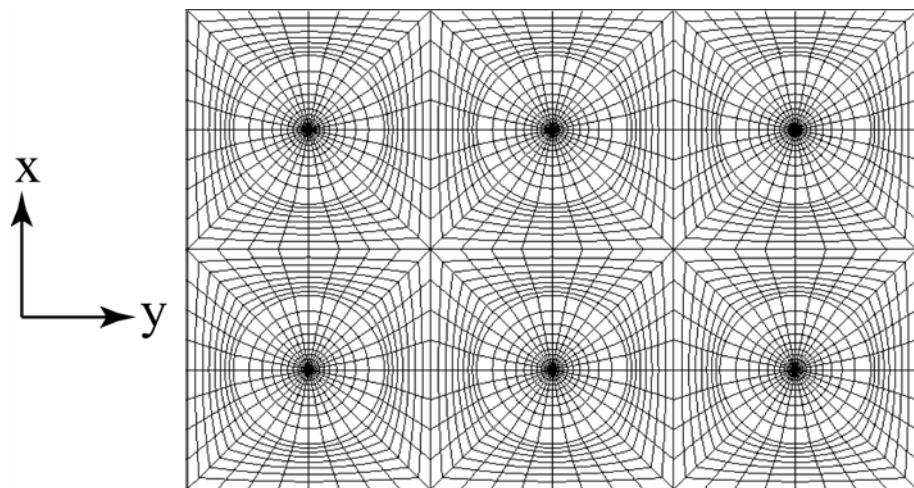
Fig. 4.2 Infinite periodic unit cell model

Table 12 Geometry of numerical model (unit: mm)

Model	L, L _s	h, h _s	a	d	2r	2b
Global model	20.0	2.0	5.0	7.0	-	-
Inclusion array	1.48	0.444	-	-	0.023	0.037



(a)



(b)

Fig. 4.3 Inclusion array model (a) model illustration (b) finite-element mesh.

As for the fatigue analysis, the predicted results of a loading and an unloading process are discussed. The illustration of loading and unloading system during fatigue analysis is shown in Fig. 4.4. The unloading process is calculated considering the history of the loading process as an initial condition. The difference in total strain between the maximum load state and the fully unloaded state gives the strain amplitude ($\Delta\varepsilon_y$) during the cyclic loading. The strain values are taken from the maximum tension side near the free surface and in the matrix.

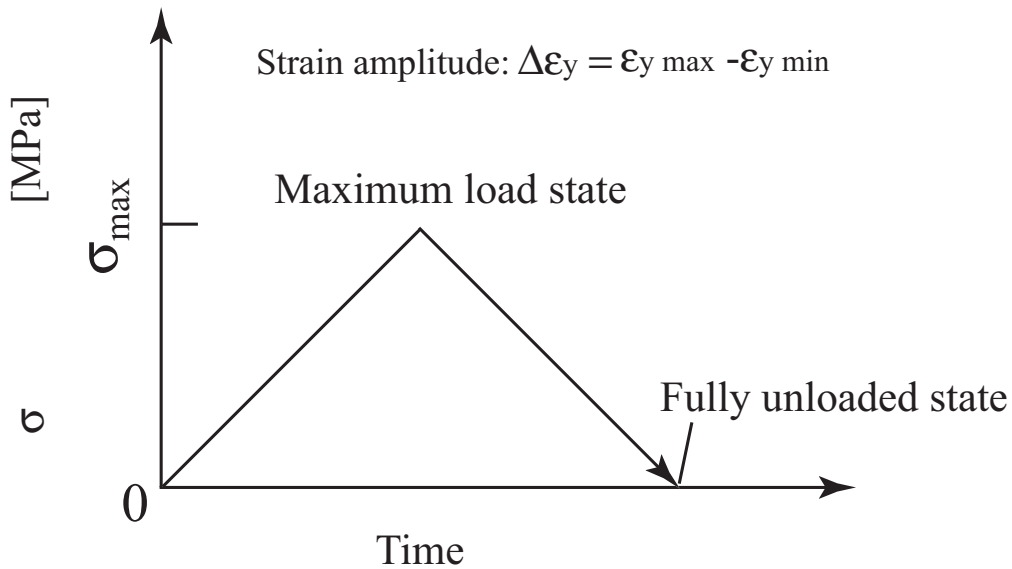


Fig. 4.4 Illustration of loading and unloading process during fatigue analysis

To characterize the whisker orientation effect, a three-dimensional single whisker unit cell model of brick shape whisker in the periodic boundary condition is developed using finite element method (FEM) to describe the overall behavior of the composite. A schematic illustration and finite-element mesh of the model is shown in Fig. 4.5. 20-nodes quadratic brick element was used in this model. In this model the whisker and the particle are embedded in a matrix in three-dimensional packing arrangement. For this model, we assume that the whisker is perfect cylinder of length l and diameter d .

Size determination of the model was made by following formulae: $ld^2 / LH^2 = V_w$ where V_w is the whisker volume fraction, L is the longitudinal whisker spacing and H is the transverse whisker spacing. Whisker volume fraction is modeled as real microstructure of 30 vol. % reinforcement in an Al alloy matrix. The whisker orientation is represented by the angle α between whisker's long axis and loading direction. To avoid complicated morphology we assumed all reinforcement to be whisker. This assumption may give overestimation of effect of whisker orientation on the stress distribution. Because of the symmetry of the cell, only 1/8 of one unit cell is treated in this analysis. The boundary condition formulation is identical to that in Llorca et al. [3] and Christman et al. [4]. The boundary conditions are as follows:

$$u_z=0, \quad \tau_{zy} = \tau_{zx} = 0 \quad \text{on } z = 0 \quad (4.1)$$

$$u_x=0, \quad \tau_{xz} = \tau_{xy} = 0 \quad \text{on } x = 0 \quad (4.2)$$

$$u_y=0, \quad \tau_{yz} = \tau_{yx} = 0 \quad \text{on } y = 0 \quad (4.3)$$

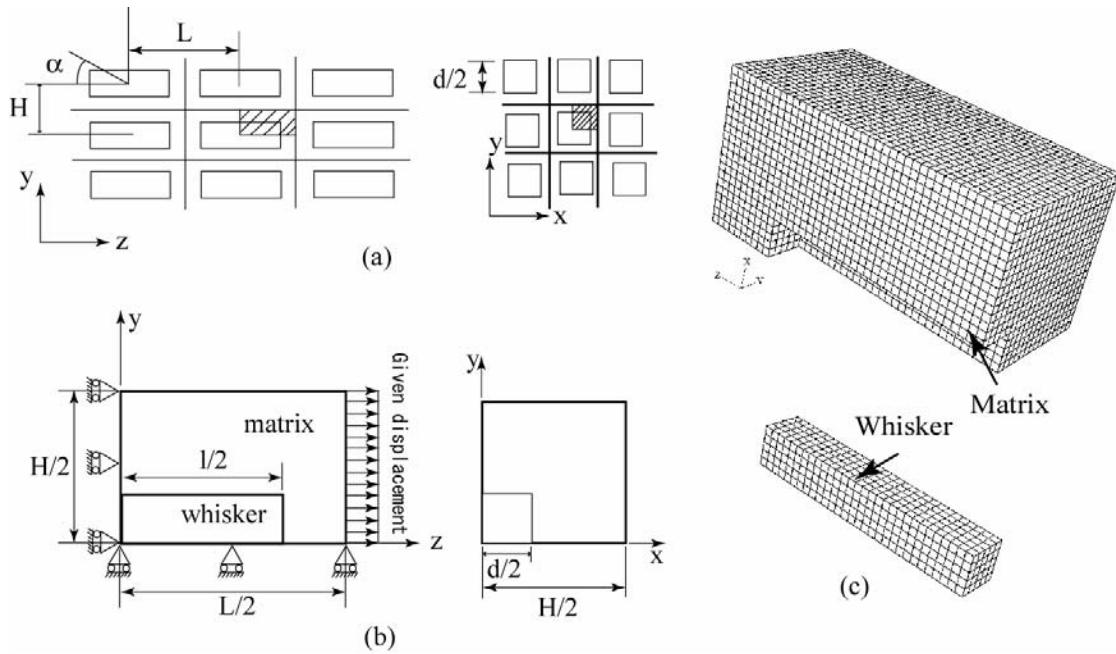
$$u_z = \varepsilon_{ave} L/2, \quad \int_{x=0}^{x=H/2} \int_{y=0}^{y=H/2} \tau_{xz} dx dy = 0,$$

$$\int_{x=0}^{x=H/2} \int_{y=0}^{y=H/2} \tau_{zy} dx dy = 0 \quad \text{on } z = L/2 \quad (4.4)$$

$$u_y = U_y, \quad \tau_{yz} = \tau_{yx} = 0, \quad \int_{z=0}^{z=L/2} \int_{x=0}^{x=H/2} \tau_{yx} dx dz = 0, \quad \int_{z=0}^{z=L/2} \int_{x=0}^{x=H/2} \tau_{yz} dx dz = 0 \quad \text{on } y = H/2 \quad (4.5)$$

$$u_x = U_x, \quad \tau_{xz} = \tau_{xy} = 0, \quad \int_{z=0}^{z=L/2} \int_{y=0}^{y=H/2} \tau_{xz} dy dz = 0, \quad \int_{z=0}^{z=L/2} \int_{y=0}^{y=H/2} \tau_{xy} dy dz = 0 \quad \text{on } x = H/2 \quad (4.6)$$

Where ε_{ave} is the macroscopic strain, U_y and U_x are constant which are determined such that the shear component of traction is free.



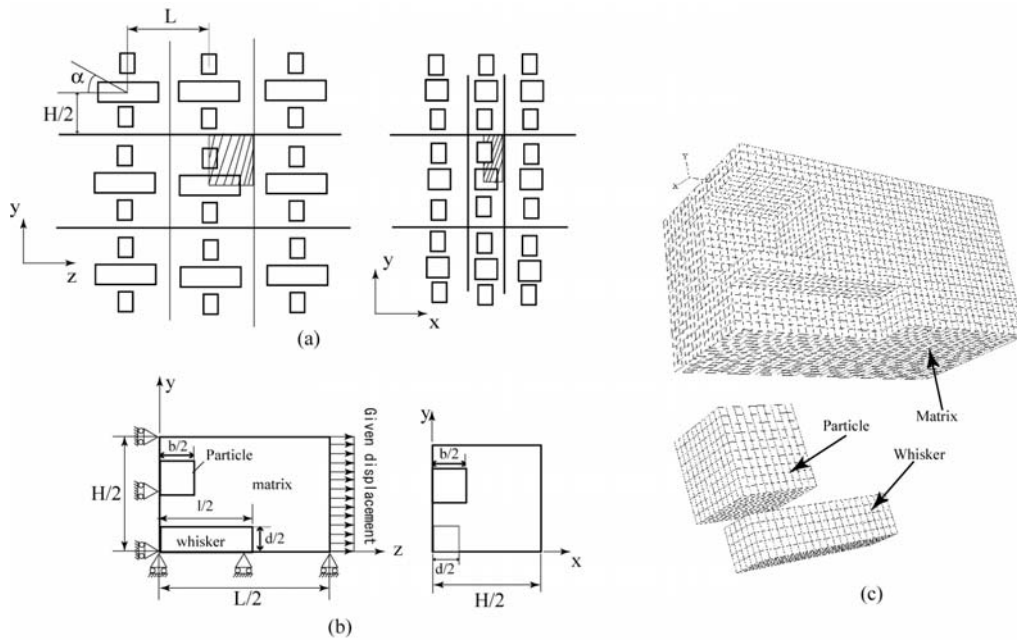
Model-1

Fig.4.5 3-D single whisker model representing the whisker reinforced Al alloy (a) and (b) schematic illustration of the periodic fiber arrangement (c) finite-element mesh.

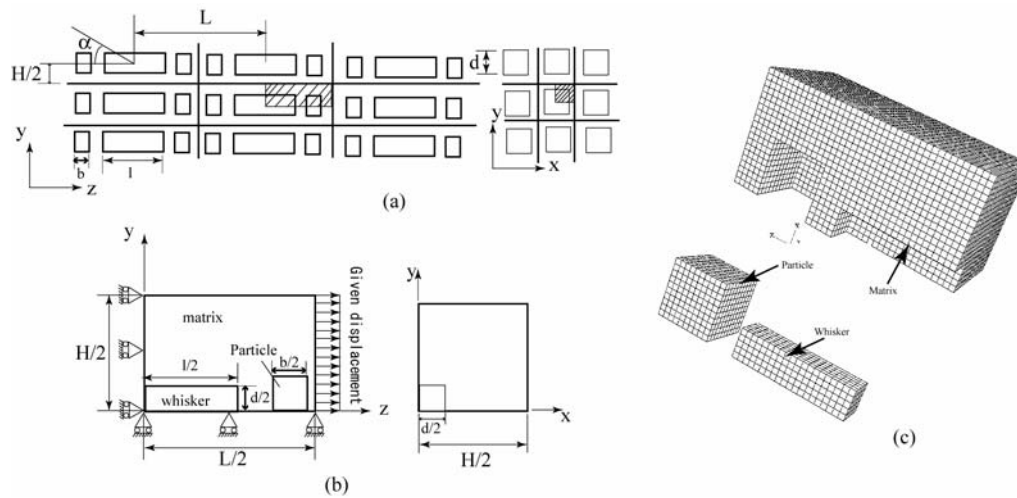
To characterize the whisker orientation effect on distributions of stress in a hybrid MMC (reinforced by Al_2O_3 whisker and SiC particle), a three-dimensional unit cell model including a whisker and particles in under the periodic boundary condition is developed using finite element method (FEM) to describe the overall behavior of the hybrid composite. A schematic illustration and finite-element mesh of the model is shown in Fig. 4.6 and Fig. 4.7 (Model-2, Model-3, and Model-4). 20-nodes quadratic brick element was used in this model.

We assume that the whisker is brick shape of length l and rectangular cross section of length d and the particle is cubic shape of length b respectively. The model-1 include only whisker. In model-2 a particle is located on the side of the whisker. For the model-3 shown in Fig. 4.6 the particle is located on the top side of the whisker end. For the model-4 shown in Fig. 4.7, the particles are located around the whisker. In all cases

only 1/8 of one unit cell is treated because of the symmetry of the cell. For all model reinforcement volume fractions is modeled as real microstructure of 9 vol. % Al_2O_3 whisker and 21 vol. % SiC particles in an Al alloy matrix for hybrid MMC and 30 Vol.% Al_2O_3 whisker for whisker reinforced MMC. Size determination of the model was made by following formulae: $ld^2 / LH^2 = V_w$ (for whisker) and $b^3 / LH^2 = V_p$ (for particle), where V_w is whisker volume fraction, V_p is particle volume fraction, L is longitudinal whisker spacing and H is the transverse whisker spacing. A chart of model illustration and mesh is shown in Table 13.

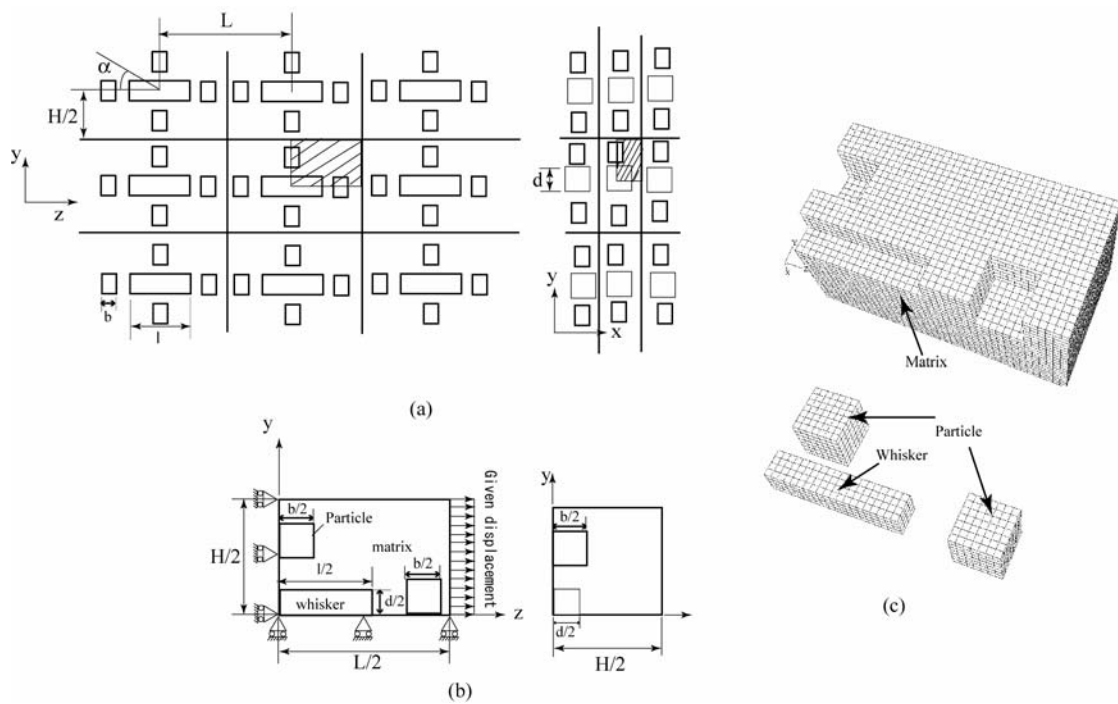


Model-2



Model-3

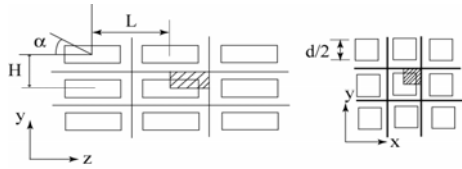
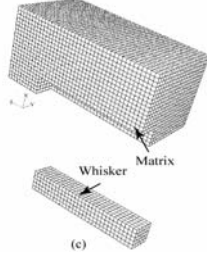
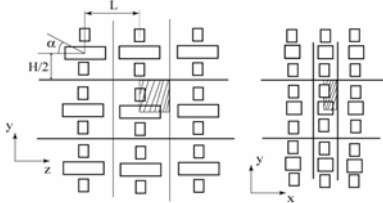
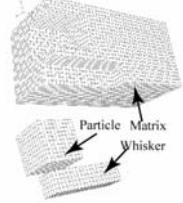
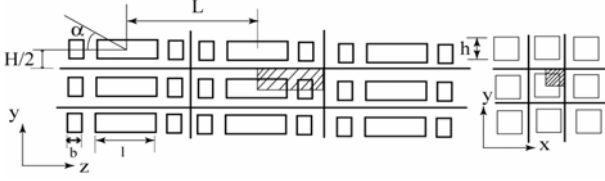
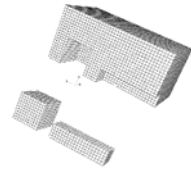
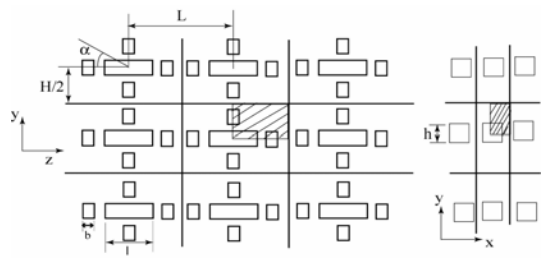
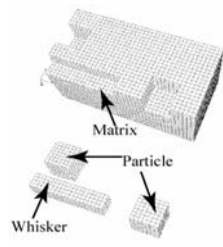
Fig.4.6 3-D hybrid model representing the whisker/ particle reinforced Al alloy (a) schematic illustration of the periodic whisker and particle arrangement (b) 1/8 model analyzed based on symmetry and (c) finite element mesh (9 Vol.% Alumina whisker and 21 Vol.% SiC particle) (Model-2, Model-3).



Model-4

Fig.4.7 3-D hybrid model representing the whisker/ particle reinforced Al alloy (a) schematic illustration of the periodic whisker and particle arrangement (b) 1/8 model analyzed based on symmetry and (c) finite element mesh (9 Vol.% Alumina whisker and 21 Vol.% SiC particle) (Model-4, Model-5).

Table13: Model chart

Model	Model illustration	Model mesh
Model-1		
Model-2		
Model-3		
Model-4		

4.3. Prediction of stress distributions and fracture mechanism

In this section, the stress distribution around the boundary between reinforced part and the unreinforced part are predicted based on a 2D inclusion array model. The critical fracture location changed by the external stress level which controls the local stress distribution obtained by the FEM prediction.

The stress distribution along y direction perpendicular to the macroscopic boundary predicted by global model of homogeneous material joint is shown in Fig. 4.8. From this result, it can be seen that the stress is concentrated around the edge of MMC and Al alloy boundary and in the MMC side which reflects a stress singularity for the interface edge of homogeneous materials joint.

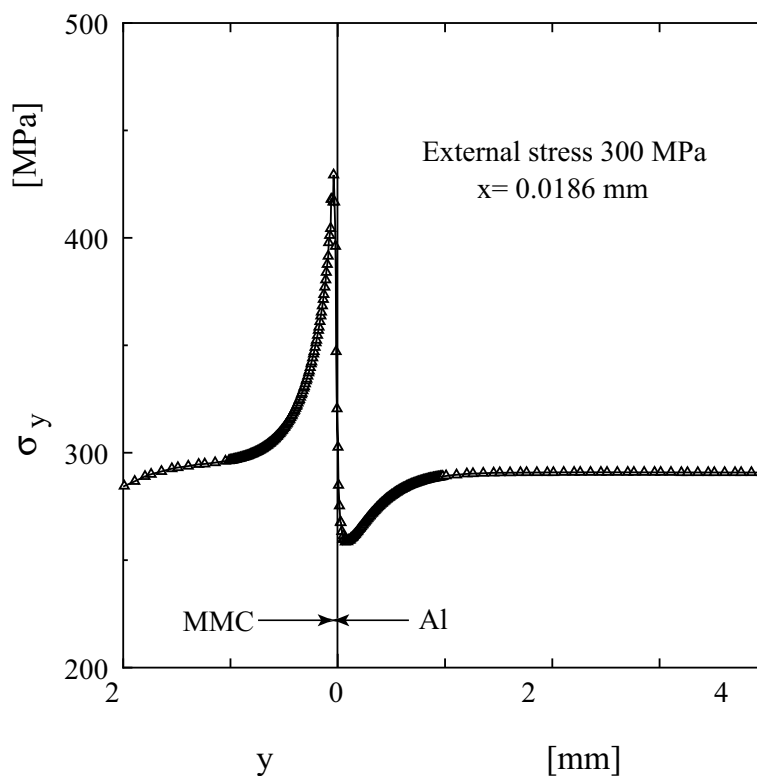


Fig. 4.8 Stress distribution along y direction of global model of homogeneous joint

From the inclusion array model analysis, the stress distribution along y direction perpendicular to the macroscopic boundary under 300 MPa nominal bending stress condition is shown in Fig 4.9 (a). The predicted stress distributions are along the inclusion array near the free surface (maximum tension side along the line A-A in Fig.4.9). The results show that the high stress is developed at the interface between matrix and inclusion. Large strain mismatch and plastic constraint between hard particle (SiC) and ductile matrix (Al) are causes the high stress in the interface. In low external stress level (under nominal bending stress is one of fatigue test 156 MPa), the stress distributions also shows that the high stress developed in the matrix between two inclusions (Fig 4.9(b)). As shown in Fig. 4.10, stress in the matrix between two inclusions perpendicular to the stress direction (along the line B-B in Fig. 4.10) gives lower stress compare to the other stress distributions.

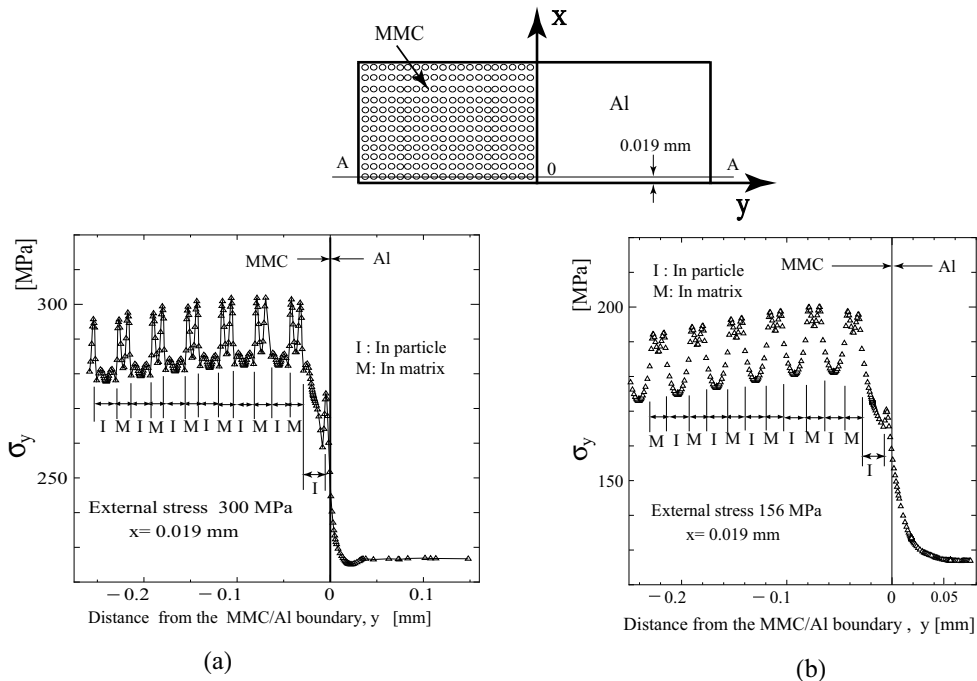


Fig. 4.9 Stress distributions along y direction of inclusion array model under nominal bending stress (a) 300 MPa (b) 156 MPa

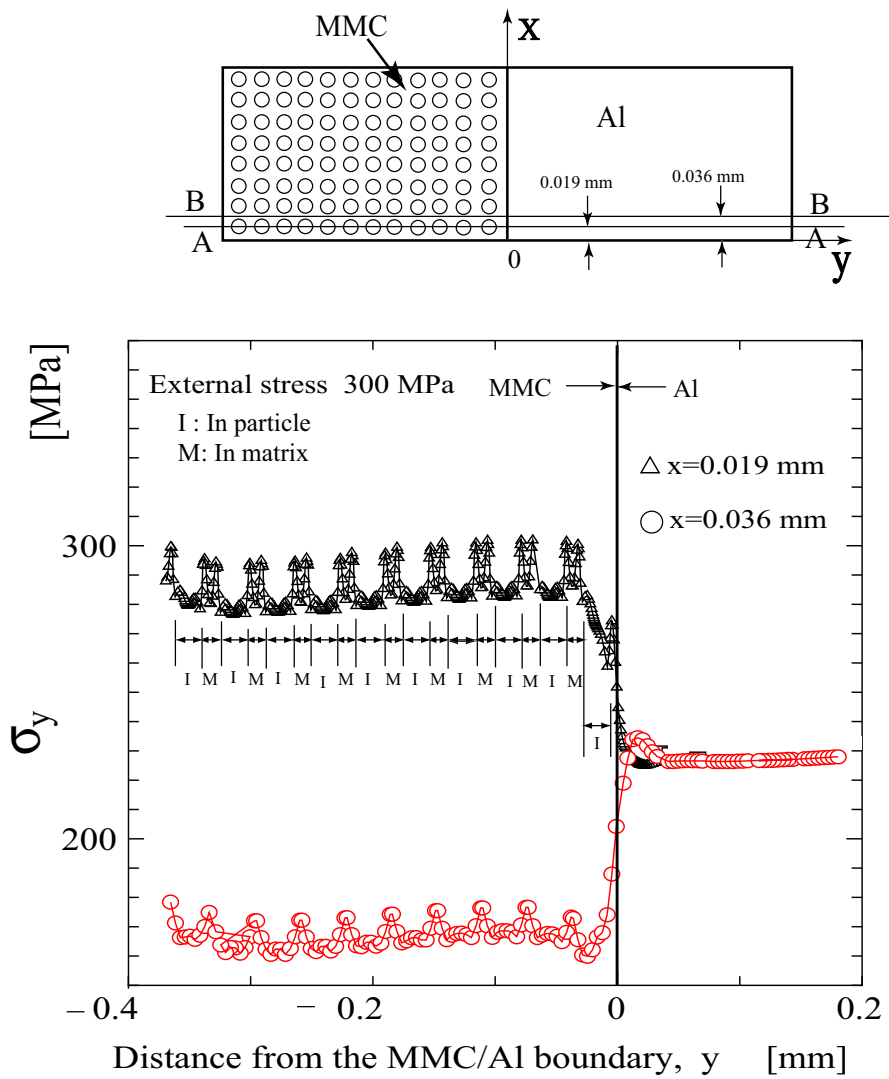
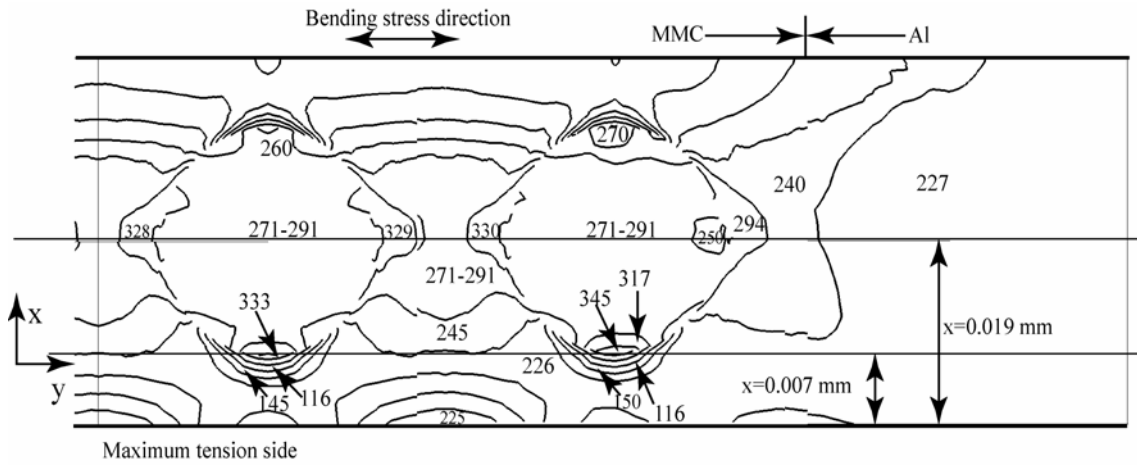


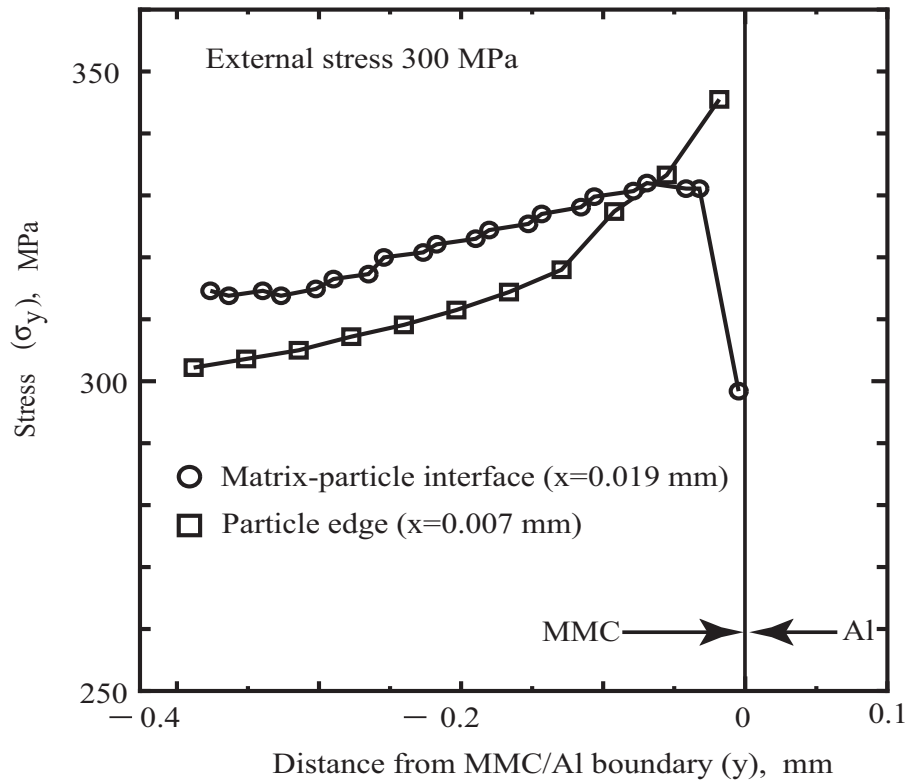
Fig. 4.10 Stress distributions along y direction of inclusion array model under nominal bending stress 300 MPa

To understand the fracture mechanism, we observe the two dimensional stress distributions at the first array of inclusions from the free surface on the tension side. Fig.4.11 (a) shows the distribution under 300 MPa nominal bending stress condition which corresponds to the nominal stress when the specimen breaks under monotonic loading and Fig.4.12 (a) shows the distribution under the nominal bending stress of 156 MPa which is one of the fatigue tests. Fig.4.11 (b) and Fig.4.12 (b) shows the distribution of the local maximum stress in the each inclusion (square symbol) and the stress on the each interface between particle and matrix (circular symbol).

From Fig.4.11 it can be seen that the peak stress develops in the first inclusion from the macroscopic boundary between the reinforced part and the unreinforced part (square symbol). The peak stress caused by the difference in mechanical properties (e.g. plastic constraint) of the inclusion and matrix leads to the particle fracture because the tensile stress is acting at the inclusion edge (345 MPa) in the high external stress case (Fig. 4.11 (a)). In the experimental observation under the monotonic loading condition, the fracture occurred at the first particle closest to the unreinforced part in the macroscopic boundary. The numerical result, which shows that the peak stress develops in the first inclusion from the macroscopic boundary, is consistent with the fracture location that was experimentally observed. On the other hand, as shown in Fig.4.12, under low nominal bending stress (156 MPa), the peak stress develops at the interface between inclusion and matrix (circle symbol) rather than in the inclusion. The maximum tensile stress (197 MPa) acting on the interface also agrees with the fractographic results, thereby, providing further verification of interfacial debonding between the reinforcing materials and the matrix alloy.

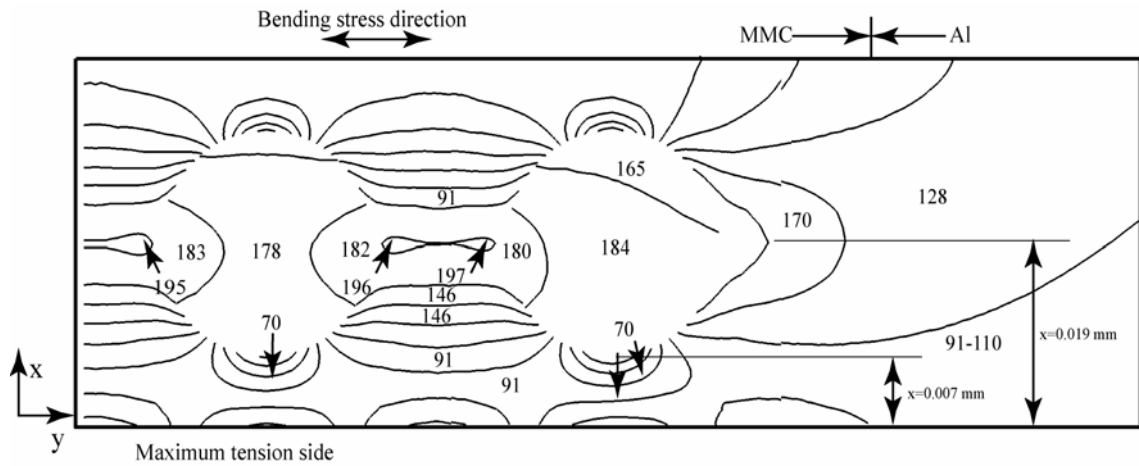


(a) Two dimensional distribution of σ_y

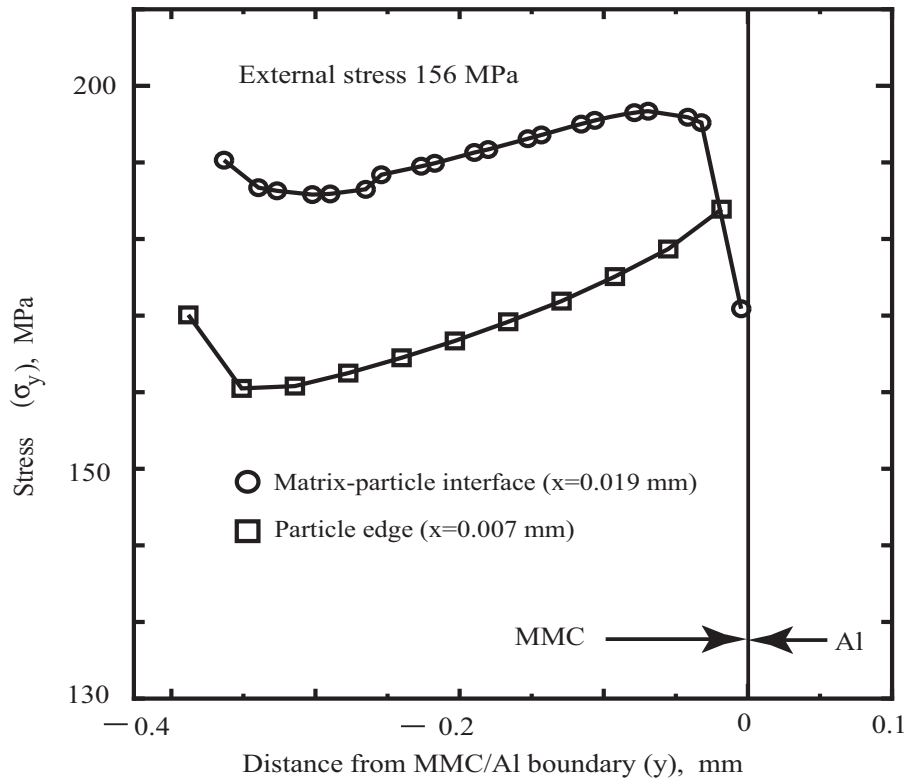


(b) Distribution of maximum stresses

Fig. 4.11 Stress distributions along y direction of inclusion array model under nominal bending stress 300 MPa



(a) Two dimensional distribution of σ_y



(b) Distribution of maximum stresses

Fig. 4.12 Stress distributions along y direction of inclusion array model under nominal bending stress 156 MPa

Distributions of total strain, ϵ_y in the matrix along the normal to the boundary at the maximum load state and the fully unloaded state for nominal bending stress of 156 MPa are shown in Fig.4.13.

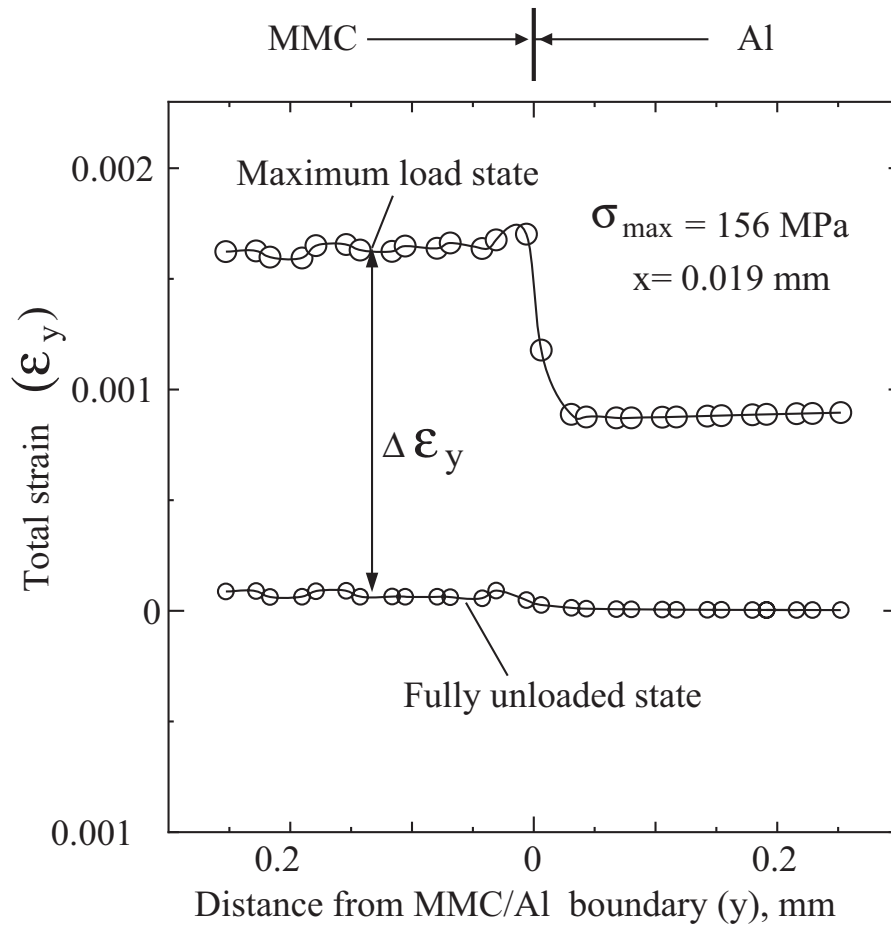


Fig. 4.13 Distributions of total strain in matrix along normal to the boundary of inclusion array model under cyclic loading at maximum stress 156 MPa.

The predicted strain amplitude ($\Delta\epsilon_y$) is much higher in the reinforced side compared to the unreinforced side. In the fatigue test, the specimen fractured in the reinforced part away from the interface. The simulation supports the experimental observation that the

fatigue fracture occurred in the reinforced part. Although the monotonic loading also passes the maximum stress the single monotonic load does not give the unstable failure.

Equivalent plastic strain distribution along y direction of inclusion array model under nominal bending stress is shown in Fig. 4.14. From this figure it can be seen that high plastic strain developed in the matrix between two inclusions. Under low nominal bending stresses (156 MPa), no equivalent plastic strain exists as shown in Fig. 4.15.

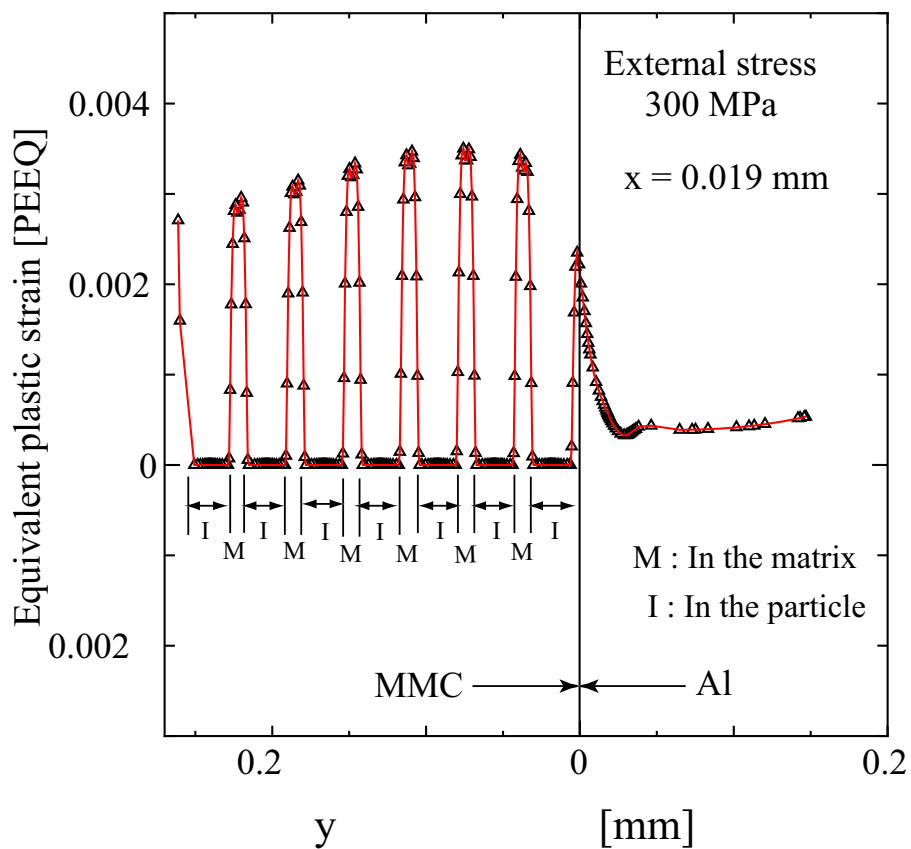


Fig. 4.14 Equivalent plastic strain distribution along y direction of inclusion array model under nominal bending stress 300 MPa

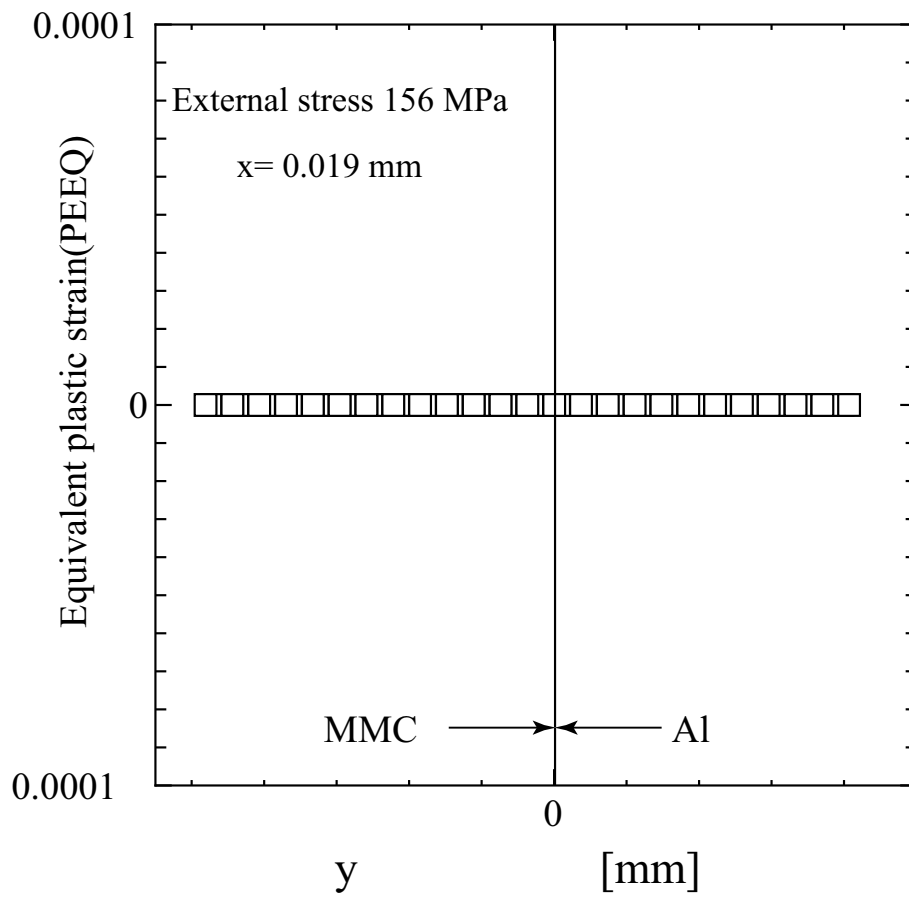


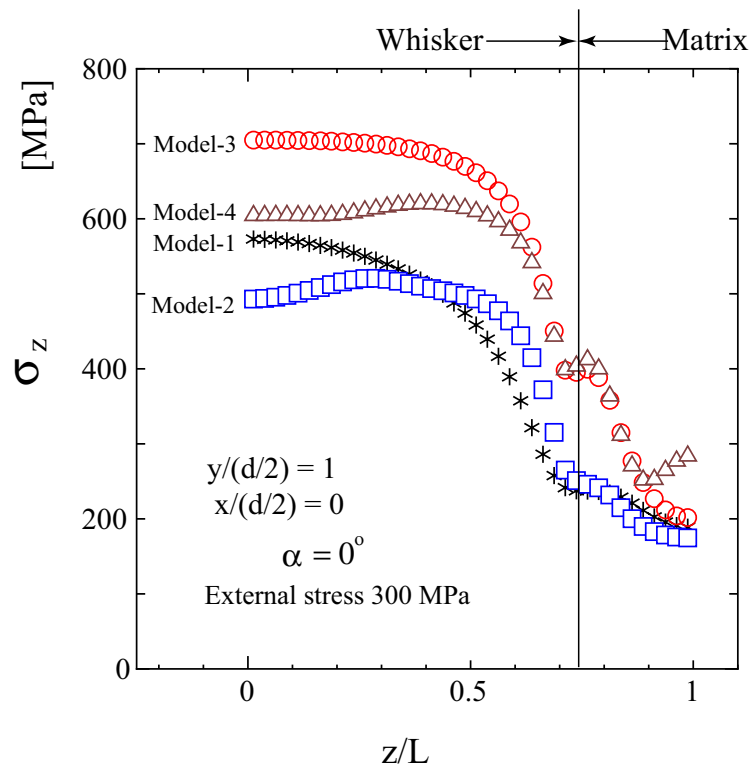
Fig. 4.15 Equivalent plastic strain distribution along y direction of inclusion array model under nominal bending stress 156 MPa

4.4. Prediction of whisker orientation effect on strength

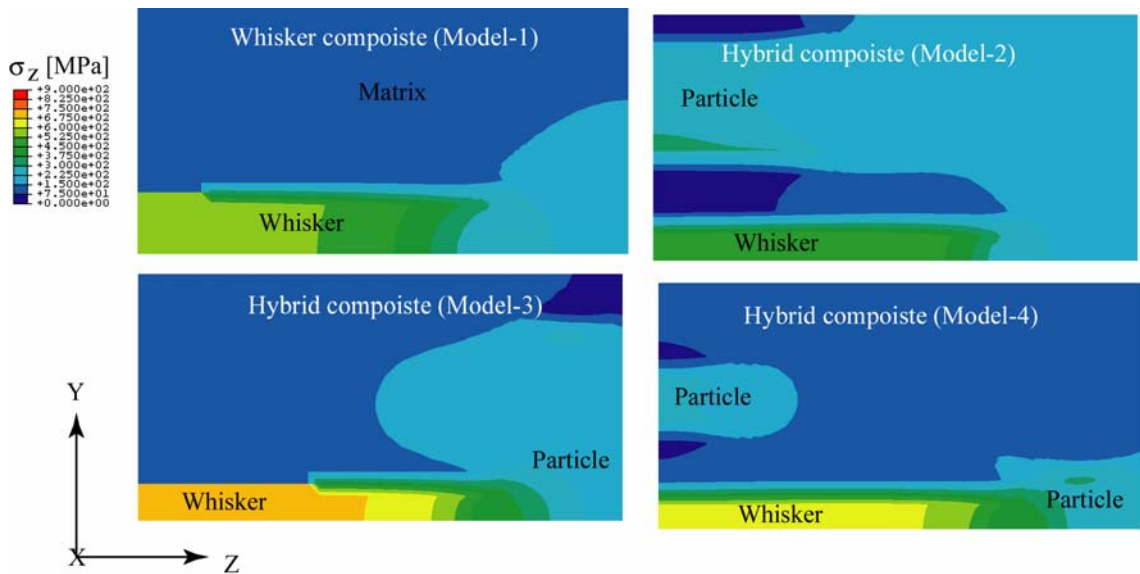
In this section, the stress distributions are predicted based on a 3D single whisker unit cell model to describe the overall behavior of the composite. These prediction results are found to be in reasonable agreement with the experimental observations.

Based on the 3-D single whisker composite and hybrid composite model (model-1, model-2, model-3, model-3) unit cell model shown in Fig. 4.5, 4.6 and 4,7, the stress distribution and magnitude of σ_{zz} along z direction of single whisker composite (Model-1) and hybrid composite (Model-2-4) shown in Fig. 4.16. From these results it can be seen that in all cases the high stress developed in the whisker which causes whisker fracture. The stress distribution in the whisker of hybrid composite is comparatively higher than whisker reinforced composite. This makes the strength of the particle/whisker reinforced hybrid composite lower in the whisker orientation $\alpha = 0^\circ$,.

Figure 4.17 shows the comparison results of stress distribution and magnitude of σ_{yy} along z direction of single whisker composite and hybrid composite. From these results it can be seen that in all cases the high stress developed at the interface between matrix and whisker end which causes whisker debonding. The stress distribution at the interface edge of hybrid composite is comparatively lower than whisker reinforced composite. This causes the higher strength of hybrid composite in the whisker orientation $\alpha = 90^\circ$.

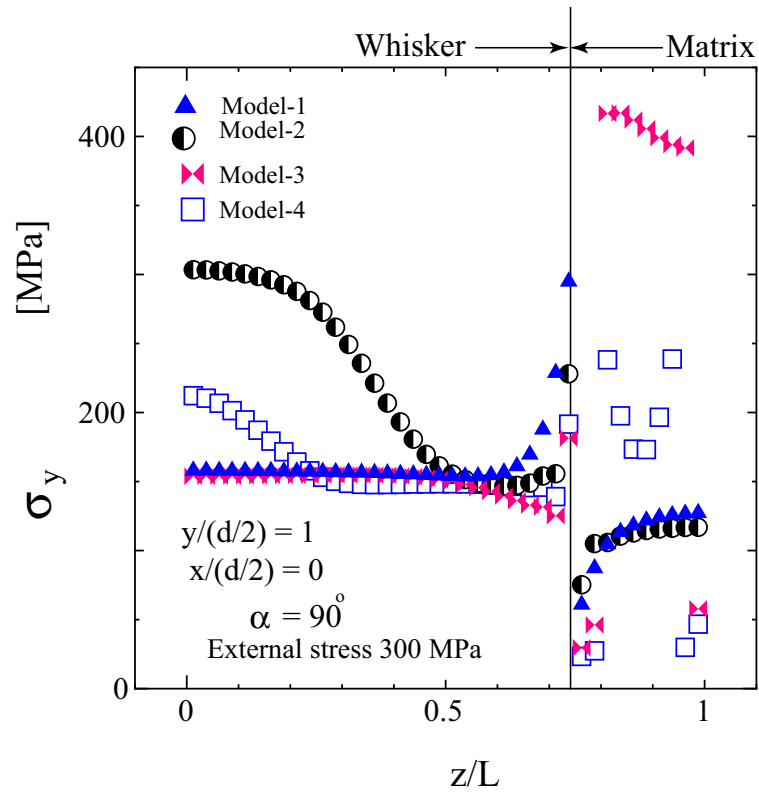


(a) Distribution of whisker stresses

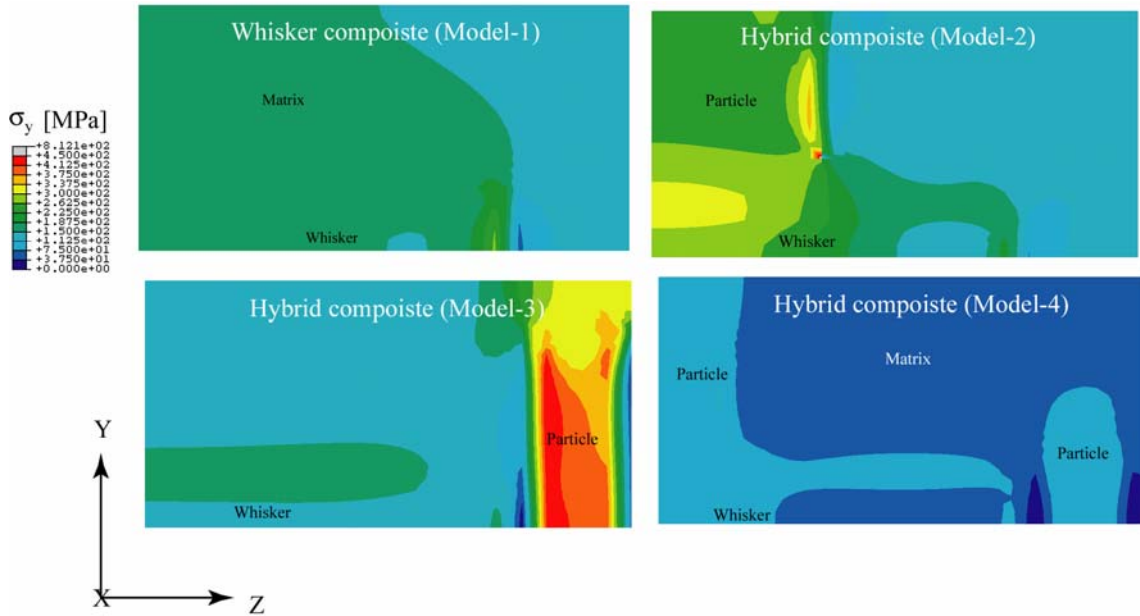


(b) Two dimensional distribution of σ_z

Fig.4.16 compares the stress distribution and magnitude of σ_{zz} along z direction of whisker composite and hybrid composite



(a) Distribution of interface stresses



(b) Two dimensional distribution of σ_r

Fig.4.17 compares the stress distribution and magnitude of σ_{yy} along z direction of whisker composite and hybrid composite

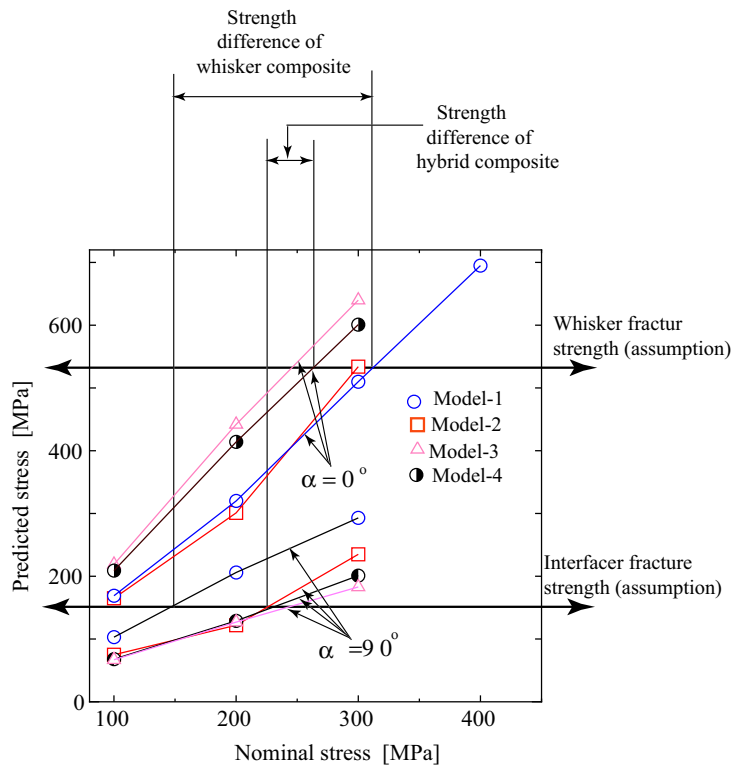


Fig.4.18 Predicted stress calculated from different nominal stress

To discuss the hybrid effect on the dependence of strength on whisker orientation, we predict the nominal stress at whisker fracture ($\alpha = 0^\circ$) and interface fracture (interface between whisker and matrix) as shown in Fig. 4.18. The calculated stresses in the whisker and on the interface are plotted. Lines of assumed whisker strength and interface strength are also plotted.

The nominal stress at the cross point between the predicted stress line and the strength line gives an estimated strength of the composite under the whisker orientation. From this figure it can be seen that hybrid composite gives higher whisker stress (Model-2, 3, and 4) than the one in whisker composite (Model-1). That's mean the strength of hybrid composite ($\alpha = 0^\circ$) is lower than in only whisker composite. It also can be seen that, the interface stress ($\alpha = 90^\circ$) of hybrid composite is lower which means the strength is

higher. On the other hand for the whisker composite strength is higher when $\alpha = 0^\circ$ and strength is lower when $\alpha = 90^\circ$. The strength difference for perpendicular loading ($\alpha = 90^\circ$) and parallel loading condition ($\alpha = 0^\circ$) of hybrid composite is small compared with that of whisker composite. That's mean whisker orientation effect on hybrid composite is lower than the whisker composite. This results gives a good agreement with others study (Trojanava et. al.[16]).

4.5. Summery

In this chapter, the stress distribution around the boundary between reinforced and unreinforced part based on inclusion array model were presented by using the finite element method. Moreover, the prediction of whisker orientation effect based on a three-dimensional single whisker unit cell model is conducted by using the finite element method. The following results are noteworthy:

1. The numerical results based on inclusion array model, which shows the peak stress develops in the first inclusion from the macroscopic boundary between the reinforced part and the unreinforced part under high nominal bending stress (300 MPa), is consistent with the fracture location that was experimentally observed. On the other hand, under low nominal bending stress (156 MPa), the peak stress develops at the interface between inclusion and matrix rather than in the inclusion that also agrees with the fractographic results of fatigue farcture, thereby, providing further verification of interfacial debonding between the reinforcing materials and the matrix alloy.
2. The predicted strain amplitude ($\Delta\varepsilon_y$) is much higher in the reinforced side compared to the unreinforced side, supports the experimental observation that the fatigue fracture occurred in the reinforced part.
3. The prediction results based on the 3-D single whisker unit cell model is found to be in reasonable agreement with experimental observations which shows with respect to the loading direction all perpendicular oriented whiskers are debonded and parallel orientated whisker are broken.
4. Whisker orientation effect on hybrid composite is lower than the whisker composite.

This results gives a good agreement with others study (Trojanava et. al.[16]).

References

- [1] AL. Chen, Y. Arai and E. Tsuchida: A numerical study on effect of thermal cycling on monotonic and cyclic response of cast aluminum alloy-SiC particulate composites. *Theoretical Applied Mechanics*, Vol. 53 (2004), pp. 63-73
- [2] L. Llorca, S. Suresh and A. Needleman: An experimental and numerical study of cyclic deformation in metal-matrix composites. *Metallurgical Transaction A*: Vol. 23A (1992), pp. 919-934.
- [3] L. Llorca, A. Needleman and S. Suresh: An analysis of the effects of matrix void growth on deformation and ductility in metal-ceramic composites. *Acta. Metall. Mater.*, Vol. 39, No. 10 (1991), pp. 2317-2335.
- [4] T. Christman, A. Needleman and S. Suresh: An experimental and numerical study of deformation in metal-ceramic composites. *Acta Materilia.*, Vol. 37, No. 11, pp. 3029-3050, 1989.
- [5] A. Borbely, H. Biermann, and O. Hartmann: FE investigation of the effect of particle distribution on the uniaxial stress-strain behavior of particulate reinforced metal-matrix composites. *Material Science and Engineering A*, Vol. 313, No. A, pp. 34-45, 2001.
- [6] D. F. Watt, X. Q. Xu and D. J. Llyod: Effect of particle morphology and spacing on the strain fields in a plastically deforming matrix. *Acta Materilia.*, Vol. 44 No. 2, pp. 789-799, 1996
- [7] X. Q. Xu and D. F. Watt: A finite element analysis of plastic relaxation and plastic accumulation at second phase particles. *Acta Materilia.*, Vol. 44 (1996), pp.

801-811.

- [8] X. Q. Xu and D. F. Watt: A numerical analysis of the effects of reinforcement content on strength and ductility in Al/(SiC)_p MMCs. *Acta Materilia.*, Vol. 44 (1996), pp 4501-4511.
- [9] T. Christman, A. Needleman, S. Nutt and S. Suresh: On microstructural evolution and micromechanical modeling of deformation of a whisker-reinforced metal-matrix composite. *Material Science and Engineering A*, Vol. 107, pp. 49-61, 1989.
- [10] S. R. Nutt and J. M. Duva: A failure mechanism in Al-SiC composites. *Scripta Metallurgica*, Vol. 20, pp. 1055-1058, 1986.
- [11] S. R. Nutt and A. Needleman: Void nucleation at fiber ends in Al-SiC composites. *Scripta Metallurgica*, Vol. 21, pp. 705-710, 1987.
- [12] R.J. Arsenault and Y. Flom: Proc. Symp. Phase Boundary Effects on Deformation, *TMS, AIME, Toronto, Canada*, pp. 261 – 279, 1985.
- [13] Guo-Zheng, Kang. and Quing, Gao., Tensile properties of randomly oriented short δ -Al₂O₃ fiber reinforced aluminium alloy composites: 2. Finite element analysis for stress transfer, elastic modulus and stress-strain curve, *Composites part A*, Vol. 33 (2002), pp. 657-667.
- [14] Li, A.B., Geng, L., Meng, Q.Y. and Zhang, J., Simulation of the large compressive deformation of the metal matrix composites with misaligned whiskers, *Material Science. and Engineering A*, Vol. 358 (2003), pp. 324-333.
- [15] Levy, A. and Papazian, J. M., Tensile properties of short fiber-reinforced SiC/Al composites: part 2. Finite-Element analysis, *Metallurgica Transection A*, Vol. 21 (1990), pp. 411-420
- [16] Trojanova, Z., Szaraz, Z., Labar, J. and Lukac, P., Deformation behaviour of an

AS21 alloy reinforced by short Saffil fibers and SiC particles, *Journal of Material Processing Technology*, Vol. 162-163 (2005), pp. 131-138.

Chapter 5: Conclusions

5.1. General conclusions

The monotonic and cyclic fracture behavior of an aluminium cast alloy, locally reinforced by SiC particles and Al₂O₃ whiskers, were investigated experimentally and numerically. The research was concentrated on the fracture mechanism and fracture location of locally reinforced material fractured under monotonic and cyclic loads. The effect of whisker orientation on monotonic and fatigue strength of an aluminium cast alloy reinforced by SiC particles and Al₂O₃ whiskers were also investigated experimentally and numerically. The key findings are as follows:

1. The fracture occurs in the reinforced part under both monotonic and cyclic loads. The stress-deflection curves under monotonic load exhibit the nonlinear relation under stress levels above 200 MPa. Fatigue fracture occurs under the maximum stress above one half of the monotonic fracture stress.
2. Under cyclic load, the fracture is dominated by interfacial debonding of particle-matrix and whisker-matrix interfaces, whereas, under monotonic load, the fracture is dominated by both particle fracture and particle/whisker-matrix interfacial debonding.
3. Under cyclic loading when the maximum stress is low and the matrix alloy is deformed elastically in the reinforced part, the minimum distance of fracture location is far (0.28 ± 0.06 mm) from the boundary between the reinforced and unreinforced parts. In the monotonic bending test, the specimens are broken very close to the boundary (i.e., at the first or second particle closest to the unreinforced part). In the

fatigue test, when the maximum stress is high, the specimens are also broken very close to the macroscopic boundary and in the reinforced part. This occurs when the matrix alloy in the reinforced part is deformed plastically within the elastically deformed reinforcement. The difference in the deformation state may be the cause of different fracture locations between the monotonic and cyclic loading.

4. From the fracture surface analysis (SEM and EDX), fatigue crack initiates from a coarse Al_2O_3 whisker fracture and propagates through the aluminium alloy matrix. Under monotonic loading, coarse Al_2O_3 whisker was not found in crack initiation site.
5. The monotonic and fatigue strength of locally reinforced material ($\alpha = 90^\circ$) is lower than the strength of homogeneous MMC ($\alpha = 0^\circ \sim 90^\circ$). Whisker orientation effect gives lower monotonic and fatigue strength of locally reinforced material ($\alpha = 90^\circ$). Whiskers randomly oriented relative to the bending stress direction cause higher strength and longer fatigue life of homogeneous MMC ($\alpha = 0^\circ \sim 90^\circ$).
6. There were many transversely debonding whiskers parallel to the fracture surface on the characteristic fracture surface of locally reinforced material ($\alpha = 90^\circ$). Broken whiskers were scarce and whiskers pulled-out could not be seen. The fracture surface is dominated by interfacial debonding of Al_2O_3 whisker/matrix according to the area fraction results. The transversely debonded whisker gives the lower strength and shorter fatigue life of locally reinforced material ($\alpha = 90^\circ$) which is corresponding to the interface debonding between whisker-matrix interfaces.
7. There were many dimples and broken whiskers in the fracture surface of homogeneous MMC ($\alpha = 0^\circ \sim 90^\circ$). Debonding whiskers are scarce and whiskers pulled-out could not be seen in the fracture surface. Whisker fractures dominate the

fracture mechanism and gives higher strength. The transversely debonded whisker gives the higher strength and longer fatigue life of homogeneous MMC ($\alpha = 0^\circ \sim 90^\circ$). This is one of the reasons why the monotonic strength and fatigue strength of homogeneous MMC is higher than that of locally reinforced material.

8. The numerical results based on inclusion array model, which shows the peak stress develops in the first inclusion from the macroscopic boundary between the reinforced part and the unreinforced part under high nominal bending stress (300 MPa), is consistent with the fracture location that was experimentally observed. On the other hand, under low nominal bending stress (156 MPa), the peak stress develops at the interface between inclusion and matrix rather than in the inclusion that also agrees with the fractographic results of fatigue fracture, thereby, providing further verification of interfacial debonding between the reinforcing materials and the matrix alloy.
9. The predicted strain amplitude ($\Delta\varepsilon_y$) is much higher in the reinforced side compared to the unreinforced side, supports the experimental observation that the fatigue fracture occurred in the reinforced part.
10. The prediction results based on the 3-D single whisker unit cell model is found to be in reasonable agreement with experimental observations which shows with respect to the loading direction all perpendicular oriented whiskers are debonded and parallel orientated whisker are broken.
11. Whisker orientation effect on hybrid composite is lower than the whisker composite. This results gives a good agreement with others study (Trojanava et. al. [Chapter1, Ref. 30]).

APPEDIX

Appendix I

As shown in Fig.A1-1and Fig. A1-2, after bending test crack has been found in or around the coarse Al_2O_3 whisker which is formed during the fabrication of hybrid whisker/particle preform. This coarse Al_2O_3 might have an influence of crack initiation and propagation during the bending test.

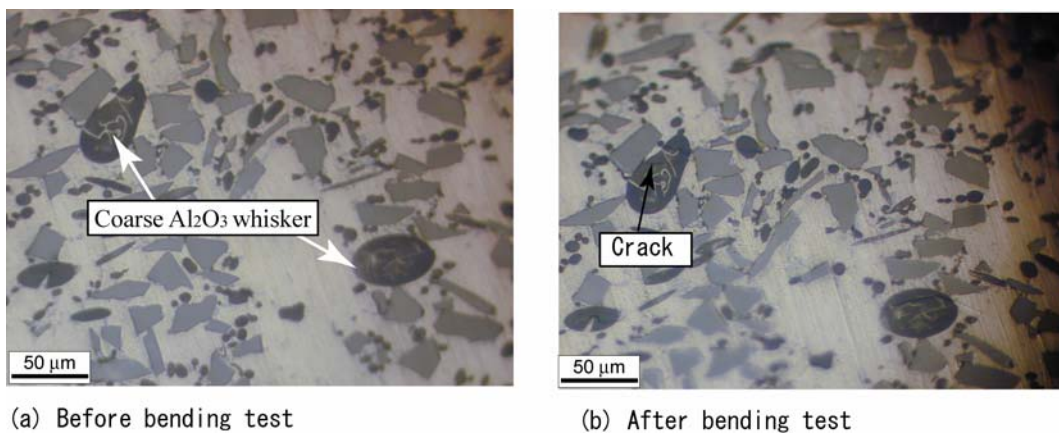


Fig. A1-1 Microscopic photograph of locally reinforced material ($\alpha = 90^\circ$) representing the coarse Al_2O_3 whisker (a) Before test (b) After test

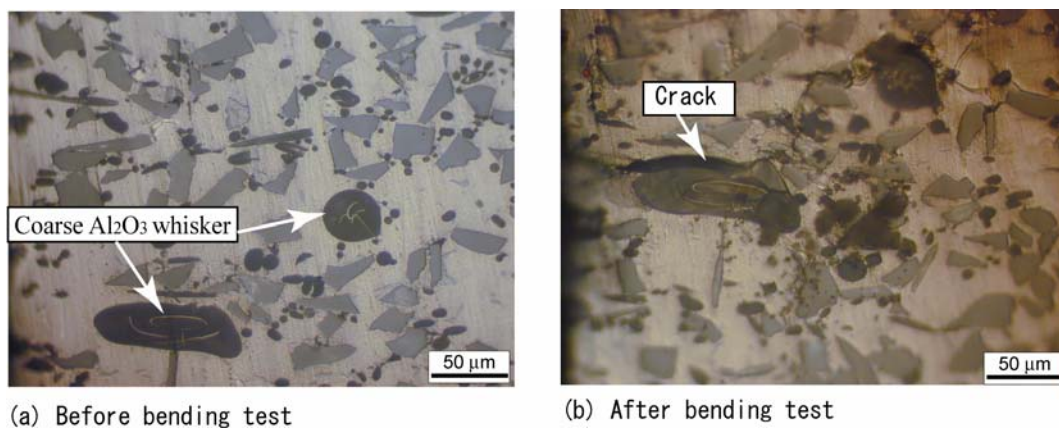


Fig. A1-2 Microscopic photograph of locally reinforced material ($\alpha = 90^\circ$) representing the coarse Al_2O_3 whisker (a) Before test (b) After test

Appendix II

Fracture path of locally reinforced material ($\alpha = 90^\circ$) and homogeneous MMC ($\alpha = 0^\circ \sim 90^\circ$) are shown in Fig.A2-1 and Fig. A2-2. Broken particles/whiskers or debonded particle/whisker are displayed on the fracture face as well as coarse whisker fracture.

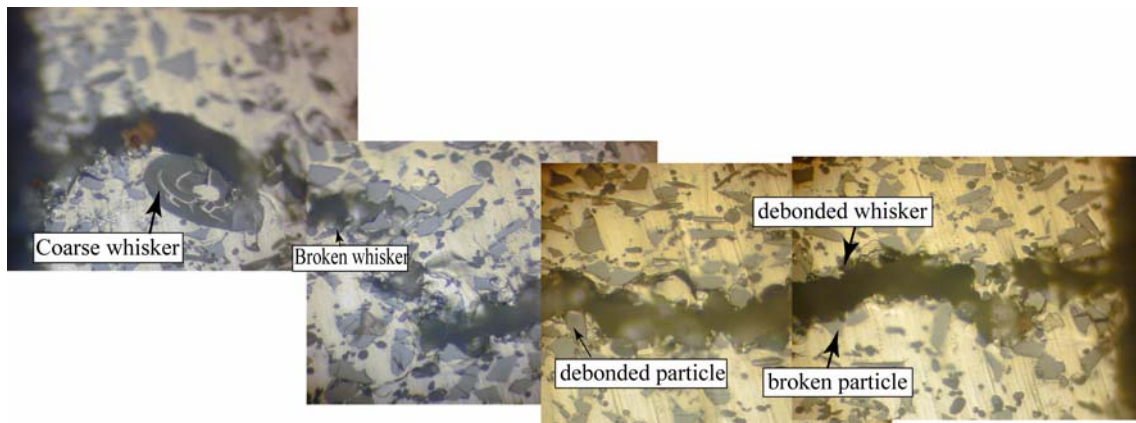


Fig.A2-1 Fracture path of locally reinforced material ($\alpha = 90^\circ$) under monotonic loading.



Fig.A2-2 Fracture path of homogeneous MMC ($\alpha = 0^\circ \sim 90^\circ$) under monotonic loading.

Appendix III

To evaluate the boundary location effect on monotonic and fatigue strength of locally reinforced material ($\alpha = 90^\circ$), we observed two types of sample are shown in Fig. A3-1 (boundary location at the center between reinforced and unreinforced part) and Fig A3-2 (boundary location not at the center).

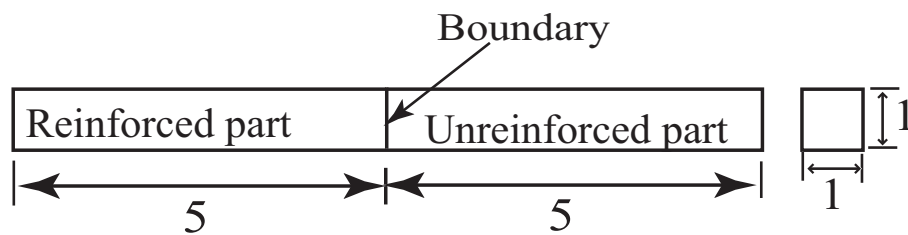


Fig.A3-1 Sample configuration of locally reinforced material ($\alpha = 90^\circ$) (boundary location at the center between reinforced and unreinforced part) (unit: mm)

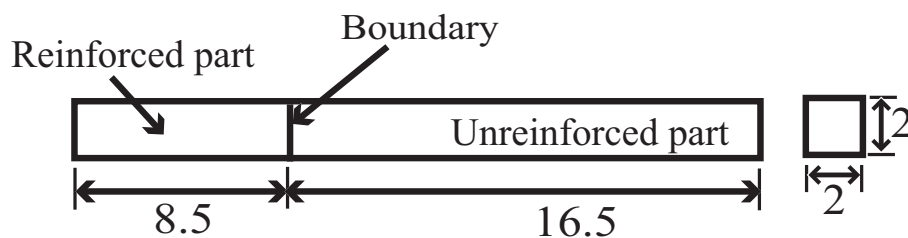


Fig. A3-2 Sample configuration of locally reinforced material ($\alpha = 90^\circ$) (boundary location not at the center between reinforced and unreinforced part) (unit: mm)

Both samples (boundary at the center and not at the center) exhibit the same average nominal bending stress is shown in Fig. A3-3. These results confirm that there is no effect of boundary location between reinforced part and unreinforced part on the strength of locally reinforced material ($\alpha = 90^\circ$).

Comparison of stress verses fatigue life behavior of locally reinforced material

($\alpha = 90^\circ$) under both boundary locations are shown in Fig. A3-4. From this Fig. it can be seen that the fatigue life with respect to the maximum stress are almost same for the both boundary location (boundary at the center and boundary not at the center) samples. From this result it is point out that there is no effect of boundary location on the fatigue strength of locally reinforced material ($\alpha = 90^\circ$).

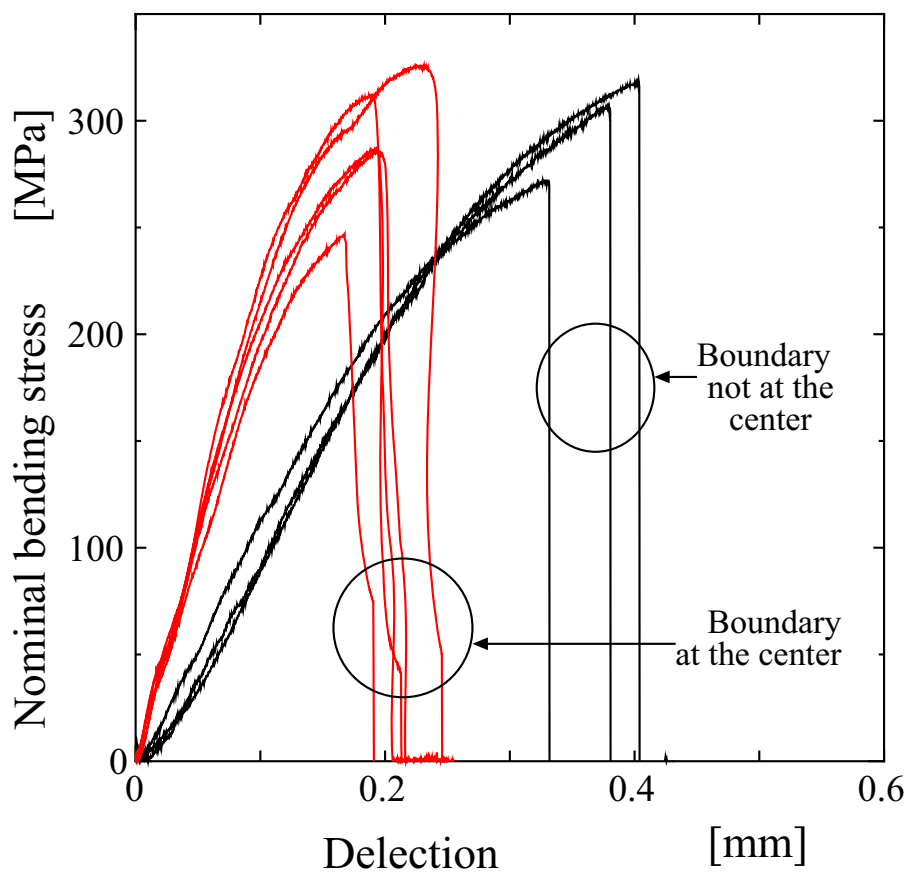


Fig. A3-3 Nominal bending stress versus deflection curves under monotonic loading (boundary location effect on strength)

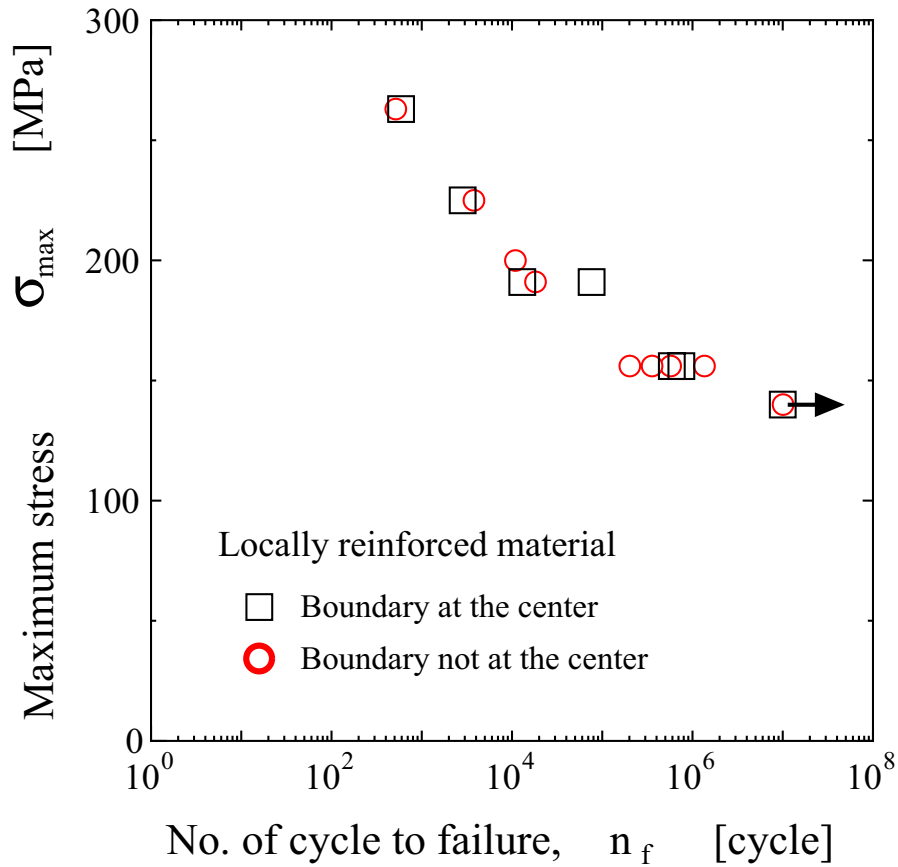
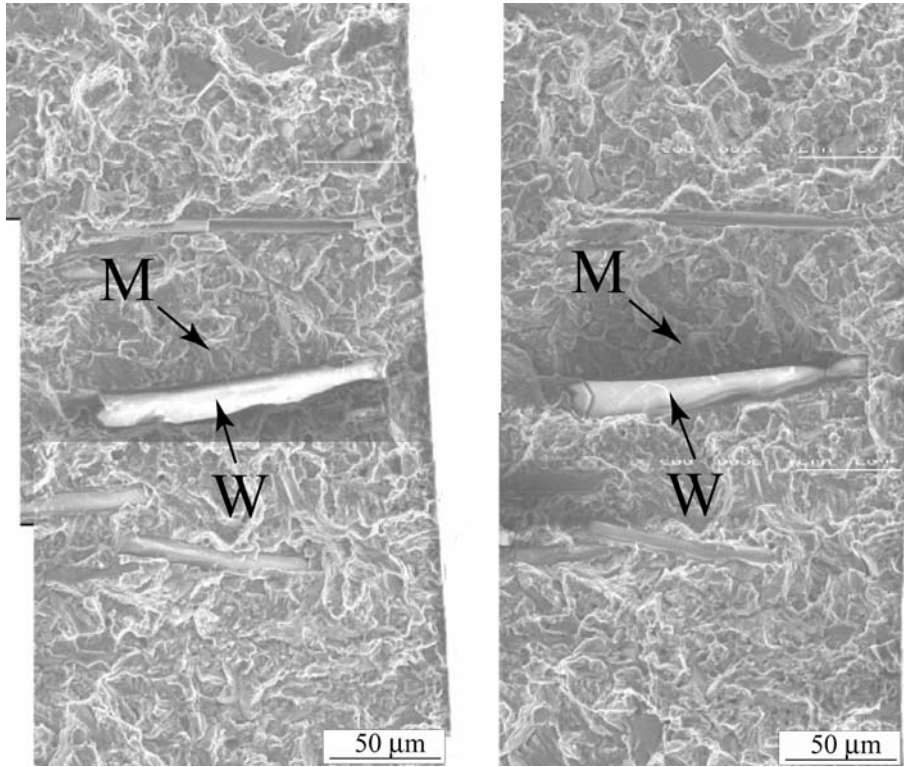


Fig.A3-4 Stress versus fatigue life behavior (stress ratio, $R=0.1$) (boundary location effect on fatigue strength)

The cyclic fracture surface of homogeneous MMC ($\alpha = 0^\circ \sim 90^\circ$) (Specimen HCTP5 in Table 5) around the fatigue crack initiation site is shown in Fig.A3-5. According to the EDX analysis, the fatigue crack initiation process is independent on the whisker orientation such that a coarse Al_2O_3 whisker fracture is the origin and the crack propagates through the aluminium alloy matrix as shown in Fig. 3.12.



**Fig. A3-5 Matching fatigue fracture surface of homogeneous MMC ($\alpha = 0^\circ \sim 90^\circ$)
after fatigue fracture $\sigma_{\max} = 191 \text{ MPa}$, $N_f = 5.6 \times 10^5$**

Appendix IV

In the global homogeneous material joint model we evaluate average elastic constants from the results of homogeneous by distributed inclusion array model shown in Fig.A4-1. Subjected forced uniform displacement at the model edge $y = L_y$. For the plane strain condition we get the following equation.

$$\bar{\varepsilon}_y = \frac{u_y}{L_y} \dots\dots\dots (1)$$

$$\bar{\varepsilon}_x = \frac{\frac{1}{L_y} \int u_x dx}{L_x} \dots\dots\dots (2)$$

$$\nu = -\frac{\bar{\varepsilon}_x}{\bar{\varepsilon}_y} \dots\dots\dots (3)$$

$$\bar{\sigma}_y = \frac{1}{L_x} \int_0^{L_x} \sigma_y(x) dx, \quad y = \frac{L_y}{2} \dots\dots\dots (4)$$

$$\bar{\sigma}_x = \frac{1}{L_y} \int_0^{L_y} \sigma_x(y) dy, \quad x = \frac{L_x}{2} \dots\dots\dots (5)$$

$$E = \frac{\bar{\sigma}_y}{\bar{\varepsilon}_y} (1 - \nu^2) - \frac{\bar{\sigma}_x}{\bar{\varepsilon}_x} \nu (1 + \nu) \dots\dots\dots (6)$$

Where $\bar{\sigma}_x$, $\bar{\sigma}_y$, $\bar{\varepsilon}_x$ and $\bar{\varepsilon}_y$ are average values of stress and strain components of the inclusion array model. From the above equation we get the results which are shown in Table A4-1.

Table A4-1 Elastic constant predicted by inclusion array model

Radius of inclusion (mm)	Young's modulus E (GPa)	Poisson's ratio ν
0.0115	168	0.244
0.015	253	0.20

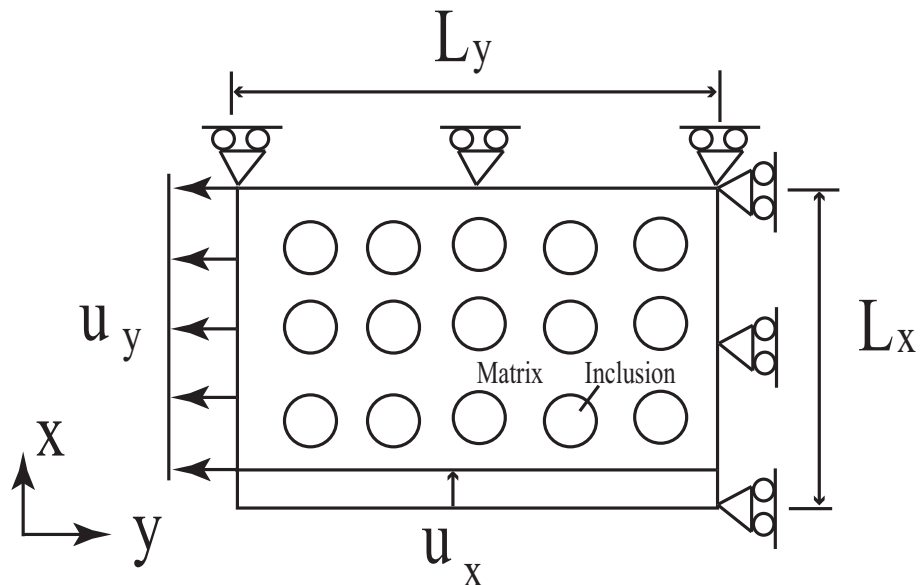


Fig. A4-1 Inclusion array model illustration to evaluate average elastic constant for homogeneous material joint model

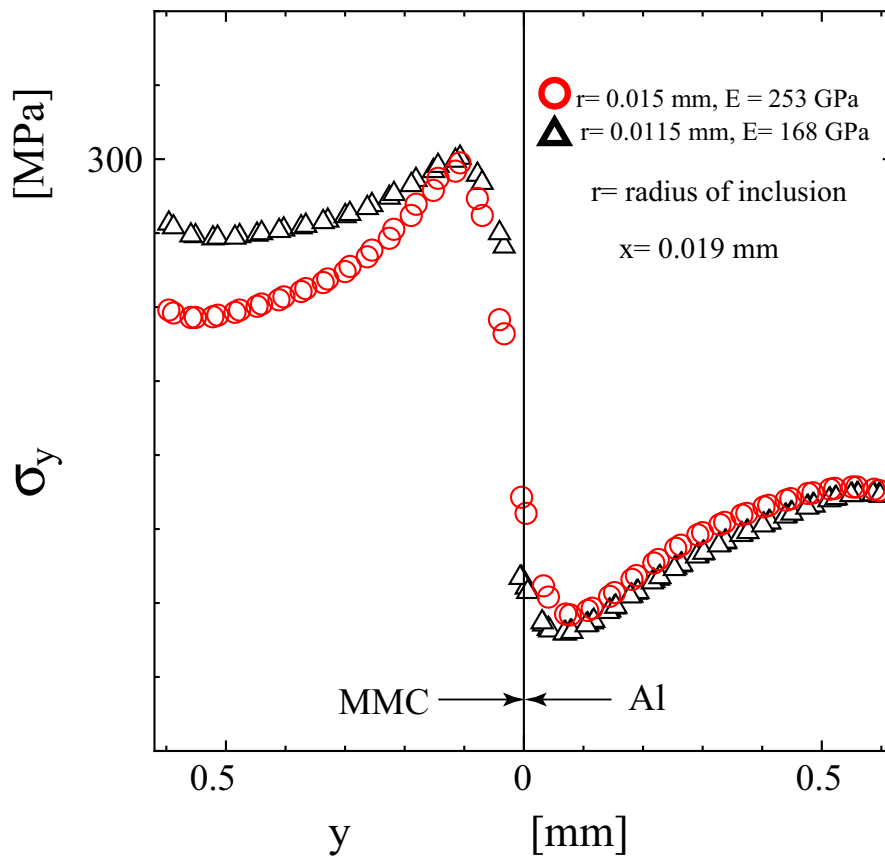


Fig. A4-2 Stress distribution along y direction of inclusion array model

By using the elastic constant in Table A4-1, the stress distribution along y direction of inclusion array model is shown in Fig. A4-1. High stress is developed in the MMC side near the interface. However, large inclusion size means high volume fraction of inclusion shows low stresses in the MMC side compare with low volume fraction inclusion results. Low strain which reflects high average Young's modulus for the higher volume fraction causes the low stress near the interface of the high volume fraction of inclusion results.

Appendix V

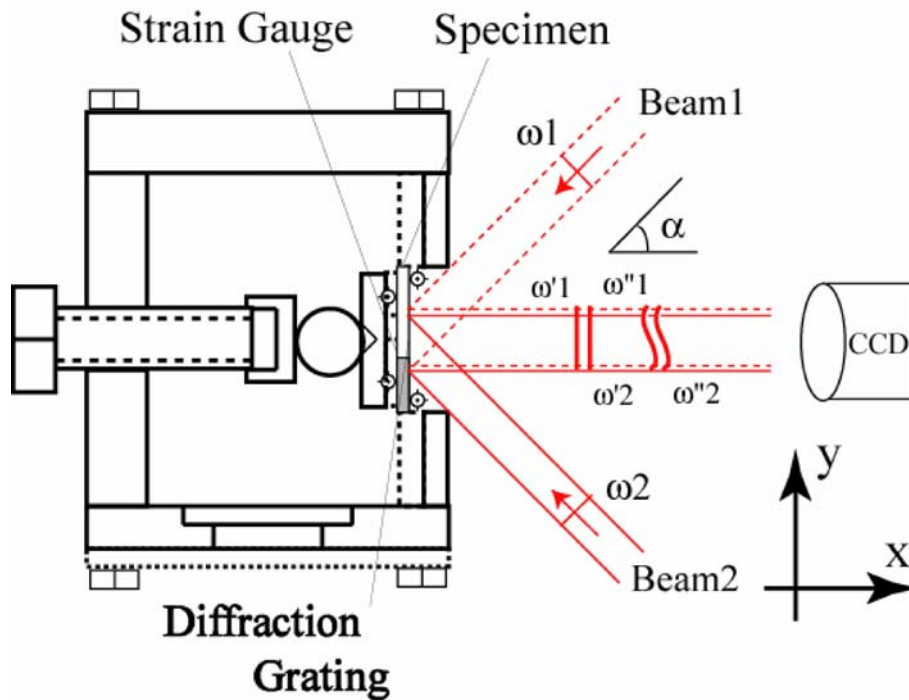


Fig. A5-1 Schematic description of moiré interferometry

Displacement fields around the boundary reinforced part and unreinforced part of locally reinforced material ($\alpha = 90^\circ$) were measured by means of high-sensitivity moiré interferometry [1]. Schematic description of moiré interferometry is shown in Fig. A5-1. Laser moiré interferometry consists of He-Ne laser (wave length 663 nm) and gratings (2 dimensional, 1200 lines/mm). While four pint bending load was applied on the specimen (the inner span 14 mm, the outer span 20 mm) the moiré fringe at mid region of the inner span was measured. The measured plan was in the tensile side.

The apparent displacement, $u_i^j (iN)$, can be measured from the fringe order, N ,

$$u_i^j(iN) = \frac{N}{f}, \dots\dots\dots (7)$$

where $u_i^j(iN)$ is the displacement in i direction, $i = y$ or z , i_N is the coordinate i of the N th fringe, $f = 2400 [1/mm]$, $j = s$ or c . $u_i^s(iN)$ is the apparent displacement in deformed state and $u_i^c(iN)$ is the apparent displacement in undeformed state. Therefore, the true displacement components $u_i(iN)$ can be calculated as the change due to the deformation,

$$u_i(iN) = u_i^s(iN) - u_i^c(iN) \dots\dots\dots (8)$$

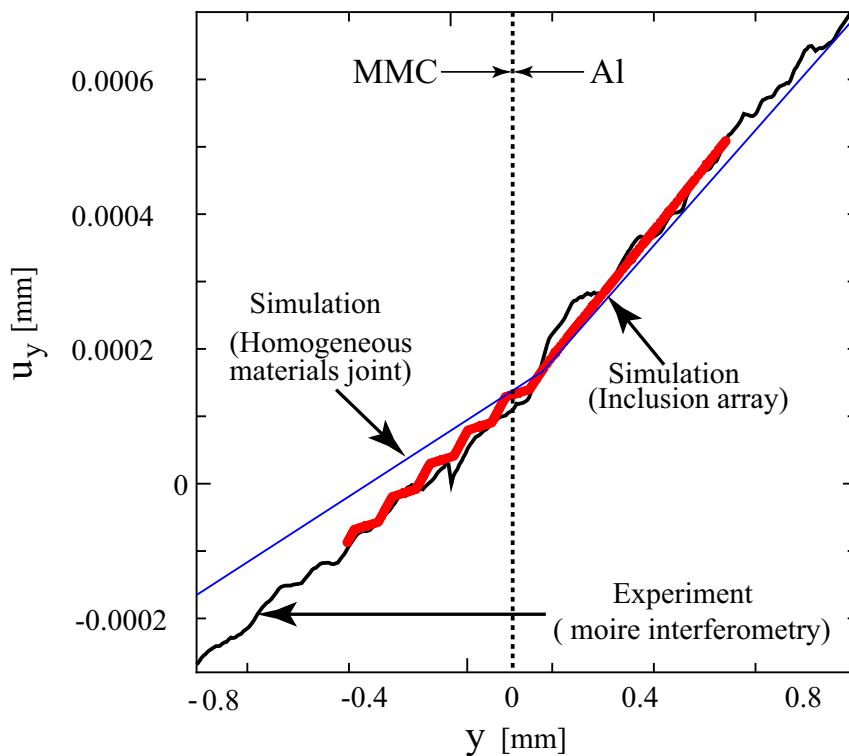


Fig. A5-2 Comparison results of experimental (moiré interferometry) and numerical displacement fields

The displacement fields around the boundary between reinforced and unreinforced part measured by moiré interferometry technique and numerical analysis is shown in Fig.A5-2. From this figure it can be seen that, the numerical results is in good agreement with the experimental results. In both cases, the high displacement gradient is developed in the MMC side that supports the experimental observation that the monotonic and fatigue fracture occurred in the reinforced part.

Appendix VI

Mesh size effect of inclusion array model was checked using a calculation on coarse and fine meshing system. The results show (Fig. A6-1) the stress distribution along y direction obtained from two meshes are the same.

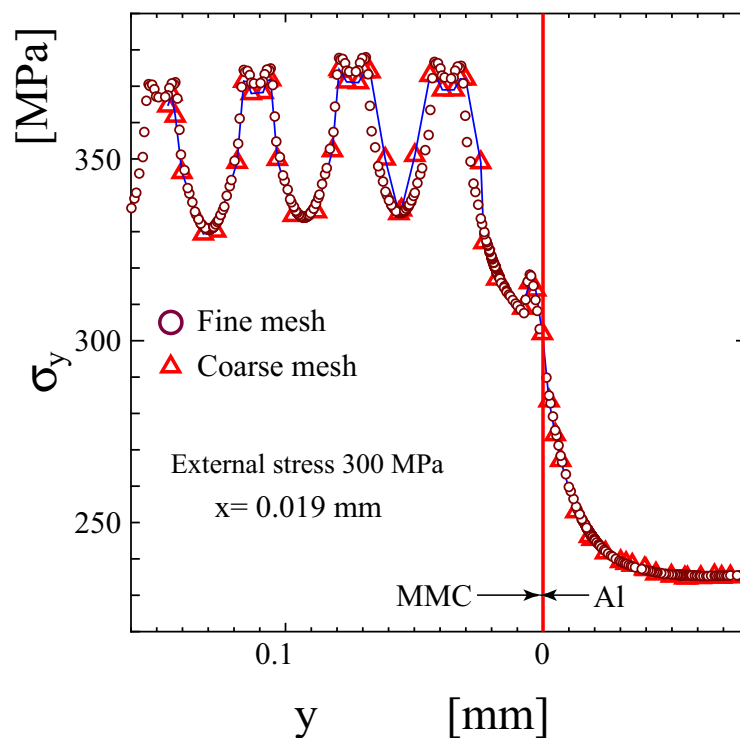


Fig. A6-1 Stress distribution along y direction of inclusion array model for two meshing system

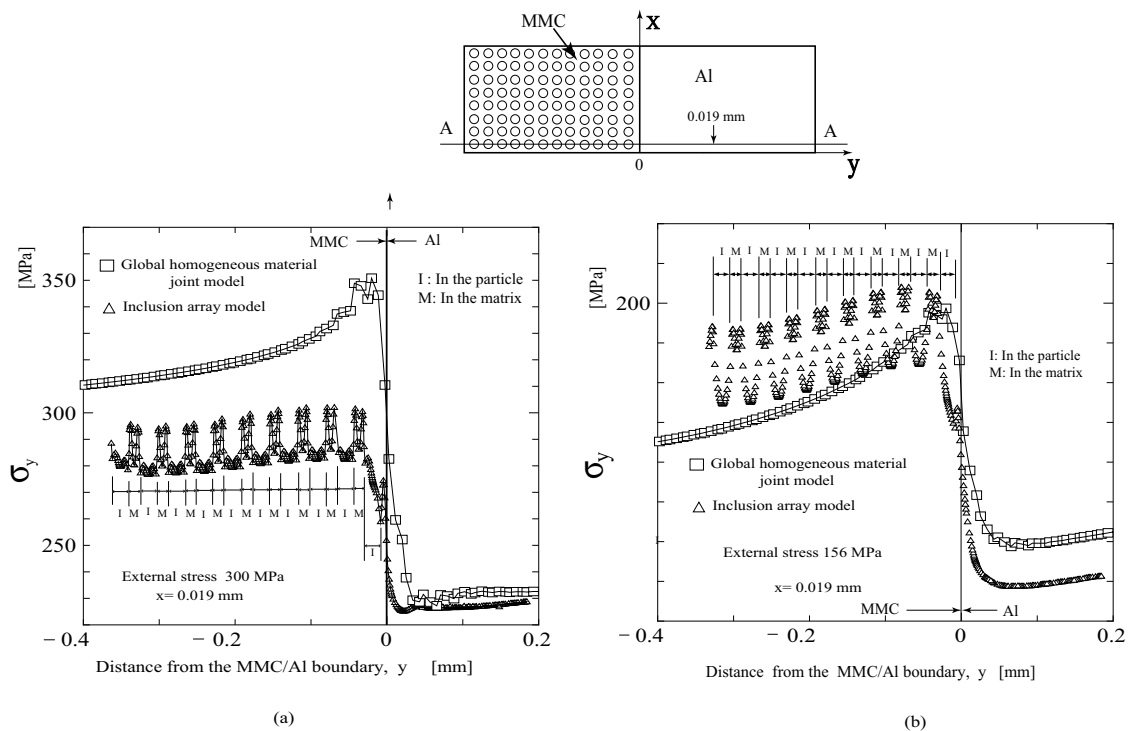


Fig. A6-2 Stress distribution around the boundary of homogeneous material joint model and inclusion array model under nominal bending stress (a) 300 MPa (b) 156 MPa

We use a sub-modeling concept and the inclusion array model boundaries (Fig. 4.2 in chapter 4) are derived by displacement fields of the macroscopic homogeneous material joint (Fig. 4.1 in chapter 4) model results. The stress distribution around the boundary of homogeneous material joint model and inclusion array model are shown in Fig. A6-2. The result shows high stress is developed in the MMC side. Under nominal bending stress 300 MPa, stress in the MMC side is less severe of inclusion array model than the one in the homogeneous material joint. However, under low external stress (156 MPa), the homogeneous materials joint model gives fairly same stress in the MMC side

compare to the inclusion array model. This is occurred due to different deformation state of matrix alloy. Under high external stress (300 MPa), SiC particle are deforming elastically within a plastically deforming matrix alloy [2]. Thus, large strain mismatch between matrix and inclusion gives the lower stress in the inclusion array model. SiC particle and matrix alloy both are elastically deforming when low external stress (156 MPa) was applied.

Appendix VII

To characterize the whisker orientation effect, a three-dimensional single whisker unit cell model of cylindrical shape whisker in the periodic boundary condition is developed using finite element method (FEM) to describe the overall behavior of the composite. A schematic illustration and finite-element mesh of the model is shown in Fig. A7-1. 20-nodes quadratic brick element was used in this model. In this model the whisker is embedded in a matrix in three-dimensional packing arrangement. For this model, we assume that the whisker is perfect cylinder of length l and diameter d . Size determination of the model was made by following formulae: $\pi d^2 l / (4LH^2) = V_w$ where V_w is the whisker volume fraction, L is the longitudinal whisker spacing and H is the transverse whisker spacing. Whisker volume fraction is modeled as real microstructure of 30 vol. % reinforcement in an Al alloy matrix. The whisker orientation is represented by the angle α between whisker's long axis and loading direction. To avoid complicated morphology we assumed all reinforcement to be whisker. This assumption may give overestimation of effect of whisker orientation on the stress distribution. Because of the symmetry of the cell, only 1/8 of one unit cell is

treated in this analysis. The boundary condition formulation is identical to that in Llorca et al. [3] and Christman et al. [4]. The boundary conditions are as follows:

$$u_z=0, \quad \tau_{zy} = \tau_{zx} = 0 \quad \text{on } z = 0 \quad (\text{A7-1})$$

$$u_x=0, \quad \tau_{xz} = \tau_{xy} = 0 \quad \text{on } x = 0 \quad (\text{A7-2})$$

$$u_y=0, \quad \tau_{yz} = \tau_{xy} = 0 \quad \text{on } y = 0 \quad (\text{A7-3})$$

$$u_z = \varepsilon_{ave} L/2, \quad \int_{x=0}^{x=H/2} \int_{y=0}^{y=H/2} \tau_{xz} dx dy = 0,$$

$$\int_{x=0}^{x=H/2} \int_{y=0}^{y=H/2} \tau_{zy} dx dy = 0 \quad \text{on } z = L/2 \quad (\text{A7-4})$$

$$u_y = U_y, \quad \tau_{yz} = \tau_{xy} = 0, \quad \int_{z=0}^{z=L/2} \int_{x=0}^{x=H/2} \tau_{yx} dx dz = 0, \quad \int_{z=0}^{z=L/2} \int_{x=0}^{x=H/2} \tau_{yz} dx dz = 0 \quad \text{on } y = H/2 \quad (\text{A7-5})$$

$$u_x = U_x, \quad \tau_{xz} = \tau_{xy} = 0, \quad \int_{z=0}^{z=L/2} \int_{y=0}^{y=H/2} \tau_{xz} dy dz = 0, \quad \int_{z=0}^{z=L/2} \int_{y=0}^{y=H/2} \tau_{xy} dy dz = 0 \quad \text{on } x = H/2 \quad (\text{A7-6})$$

Where ε_{ave} is the macroscopic strain, U_y and U_x are constant which are determined such that the shear component of traction is free.

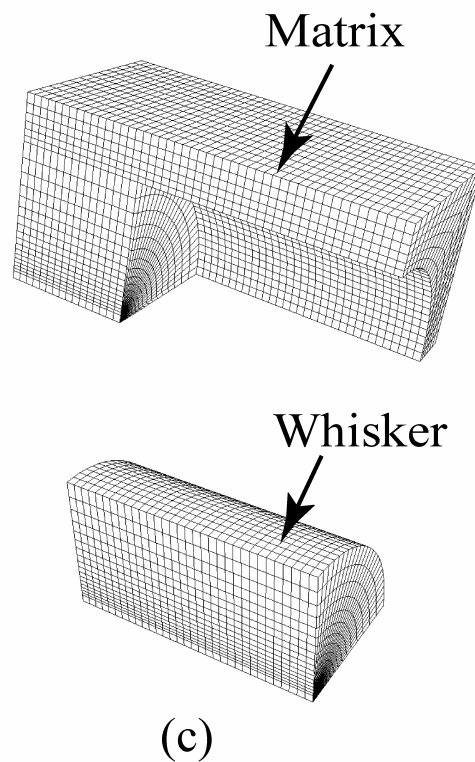
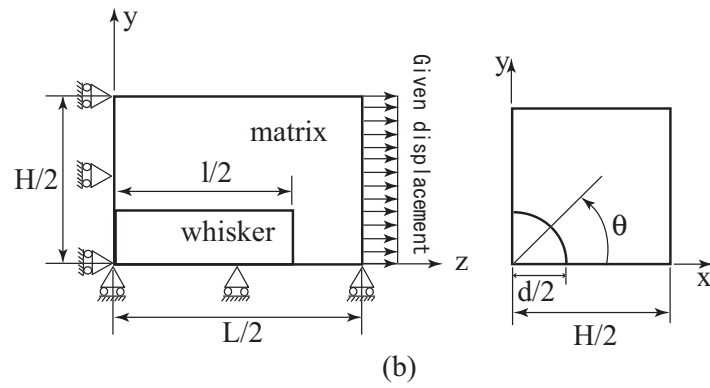
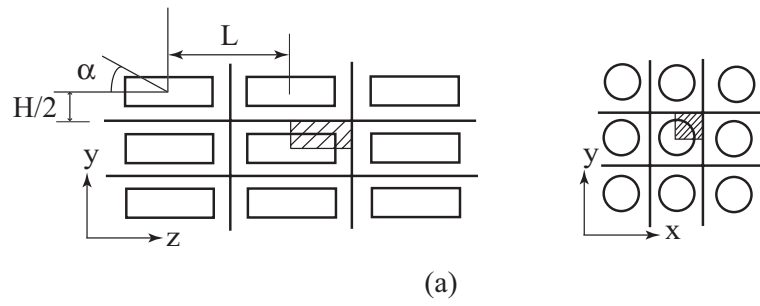


Fig. A7-1 3-D single whisker model representing the whisker reinforced Al alloy
(a) schematic illustration of the periodic fiber arrangement (b) 1/8 model analyzed
based on symmetry and (c) finite-element mesh.

To characterize the whisker orientation effect of hybrid MMC (reinforced by Al_2O_3 whisker and SiC particle), a three-dimensional single whisker and particle unit cell model of cylindrical shape whisker in the periodic boundary condition is developed using finite element method (FEM) to describe the overall behavior of the composite. A schematic illustration and finite-element mesh of the model is shown in Fig. A7-2. 20-nodes quadratic brick element was used in this model. In this model the whisker and particle is embedded in a matrix in three-dimensional packing arrangement. For this model, we assume that the whisker is perfect cylinder of length l and diameter d and the particle is also perfect cylinder of length b and diameter is same as whisker (d).

Size determination of the model was made by following formulae: $\pi(l+b)d^2/(4LH^2) = V_r$ where V_r is the reinforcement volume fraction, L is the longitudinal whisker spacing and H is the transverse whisker spacing. Reinforcement volume fraction is modeled as real microstructure of 30 vol. % reinforcement in an Al alloy matrix. The whisker orientation is represented by the angle α between whisker's long axis and loading direction. Because of the symmetry of the cell, only 1/8 of one unit cell is treated in this analysis. The boundary condition formulation is identical to that in Llorca et al. [3] and Christman et al. [4]. The boundary conditions are given in equation A7-1~A7-6.

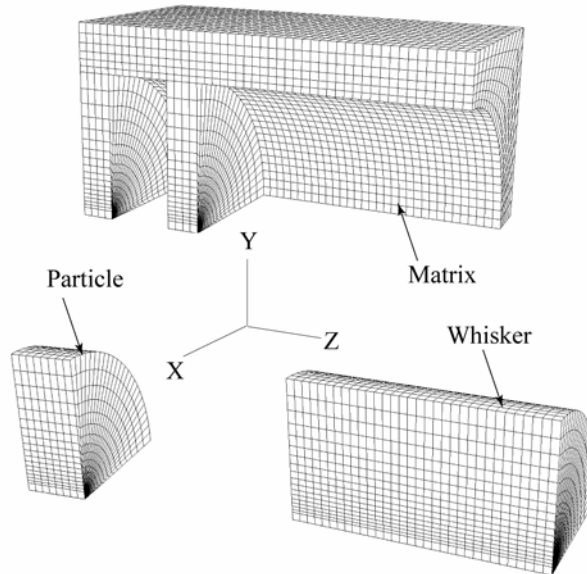
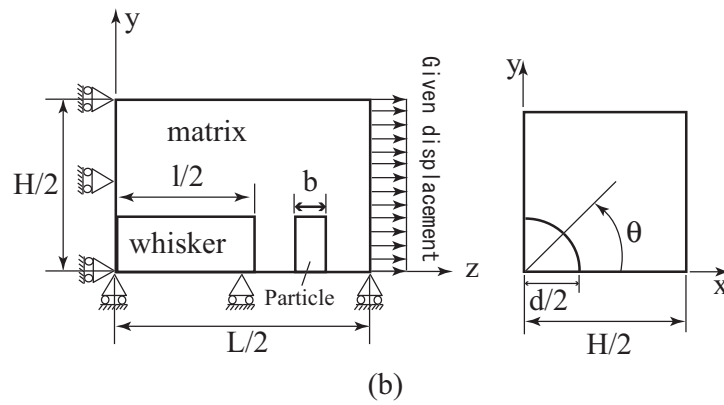
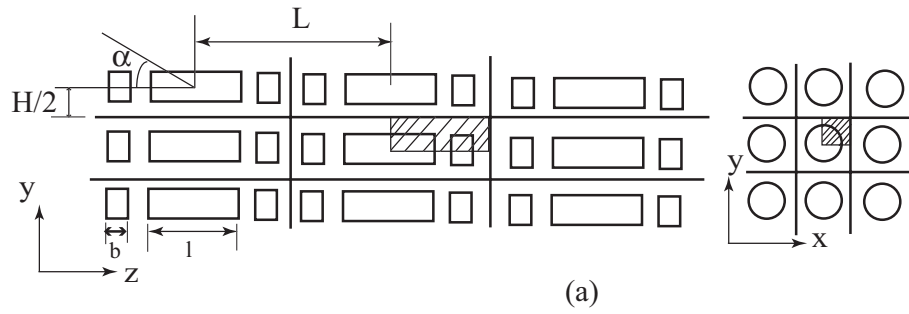


Fig.A7-2 3-D single whisker model representing the hybrid whisker/ particle reinforced Al alloy (a) schematic illustration of the periodic fiber and particle arrangement (b) 1/8 model analyzed based on symmetry and (c) finite-element mesh.

Based on the 3-D single whisker unit cell model shown in Fig. A7-1, stress distribution along z direction for longitudinal loading ($\alpha = 0^\circ$, parallel to the whisker direction) is shown in Fig.A7-3. From this result it can be seen that the high stress is developed in the whisker compared with the stress in the matrix. From the experimental results we found that with respect to the loading direction all parallel oriented whiskers are broken. For longitudinal loading, the prediction results based on the 3-D single whisker unit cell model is found to be in reasonable agreement with experimental observations.

Stress distribution along z direction transverse loading ($\alpha = 90^\circ$, perpendicular to the whisker direction) is shown in Fig. A7-4. From this result it can be seen that the high stress is developed at the edge of interface between whisker and matrix. In the experimental results we find that with respect to the loading direction all perpendicular oriented whiskers are debonded. For transverse loading, the prediction results based on the 3-D single whisker unit cell model is also found to be in reasonable agreement with experimental observations.

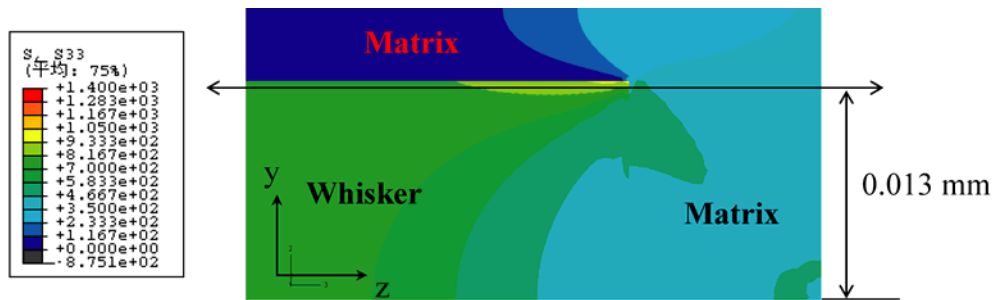
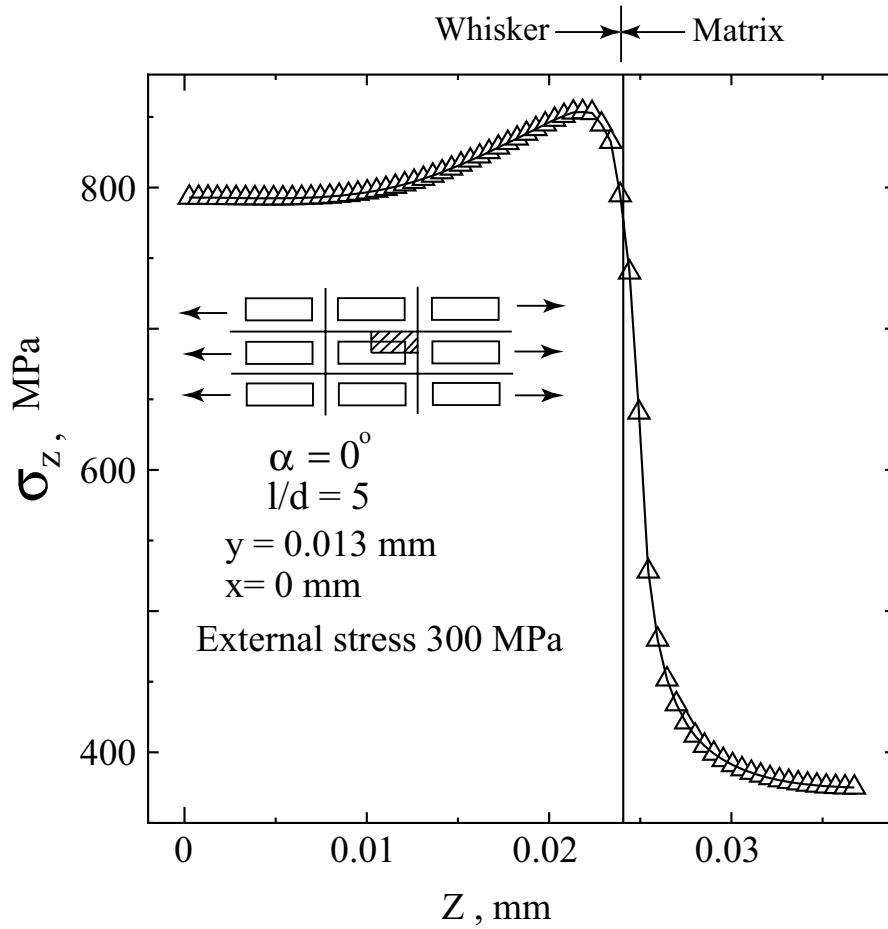


Fig.A7-3 Stress distribution along z direction for longitudinal loading (parallel to the stress direction).

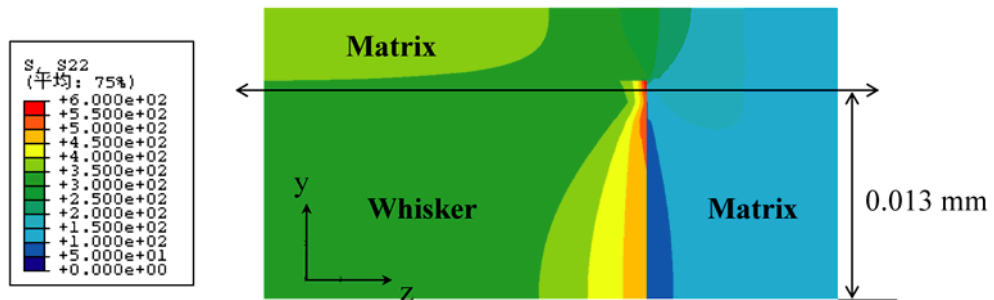
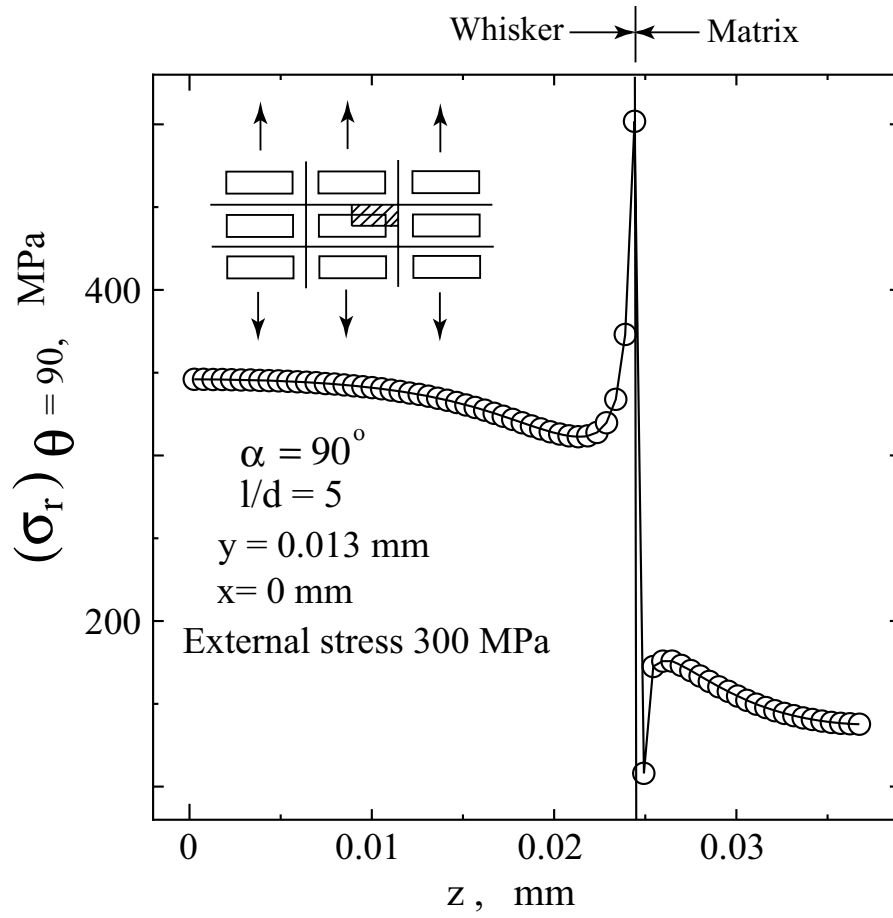


Fig.A7-4 Stress distribution along z direction for transverse loading (perpendicular to the stress direction).

Based on the 3-D single whisker/particle hybrid unit cell model shown in Fig. A7-2, stress distribution along z direction for longitudinal loading ($\alpha = 0^\circ$, parallel to the whisker direction) is shown in Fig.A7-5. From this result it can be seen that the high stress is developed in the whisker compared with the stress in the matrix and particle. Existence of a series particle to a whisker does not give large change in the maximum stress. From the experimental results we found that with respect to the loading direction all parallel oriented whiskers are broken. For longitudinal loading, the prediction results based on the 3-D single whisker/particle hybrid unit cell model is found to be in reasonable agreement with experimental observations.

Stress distribution along z direction transverse loading ($\alpha = 90^\circ$, perpendicular to the whisker direction) is shown in Fig. A7-6. From this result it can be seen that the high stress is developed at the edge of particle/ whisker and particle/matrix interface. In the experimental results we find that with respect to the loading direction all perpendicular oriented whiskers are debonded. Also the fracture surfaces were dominated by the particle debonding as well as particle fracture. For transverse loading, the prediction results based on the 3-D single whisker/particle hybrid unit cell model is also found to be in reasonable agreement with experimental observations.

From the results of stress distribution along z direction transverse loading ($\alpha = 90^\circ$, perpendicular to the whisker direction) in FigA7-7, it can be seen that due to the hybrid effect, the high stress is developed in the particle. This stress causes the particle fracture.

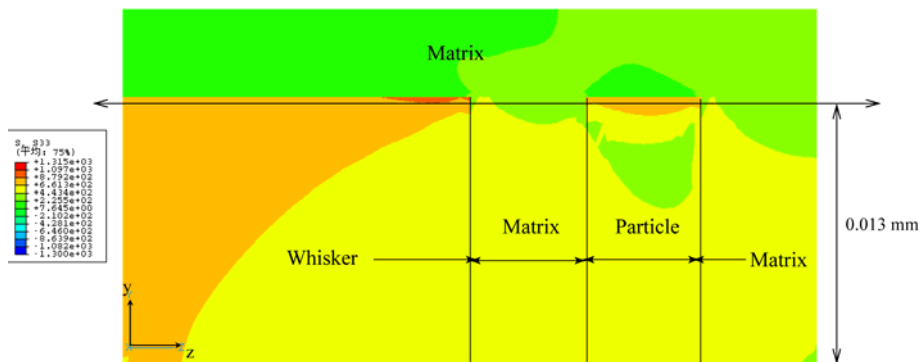
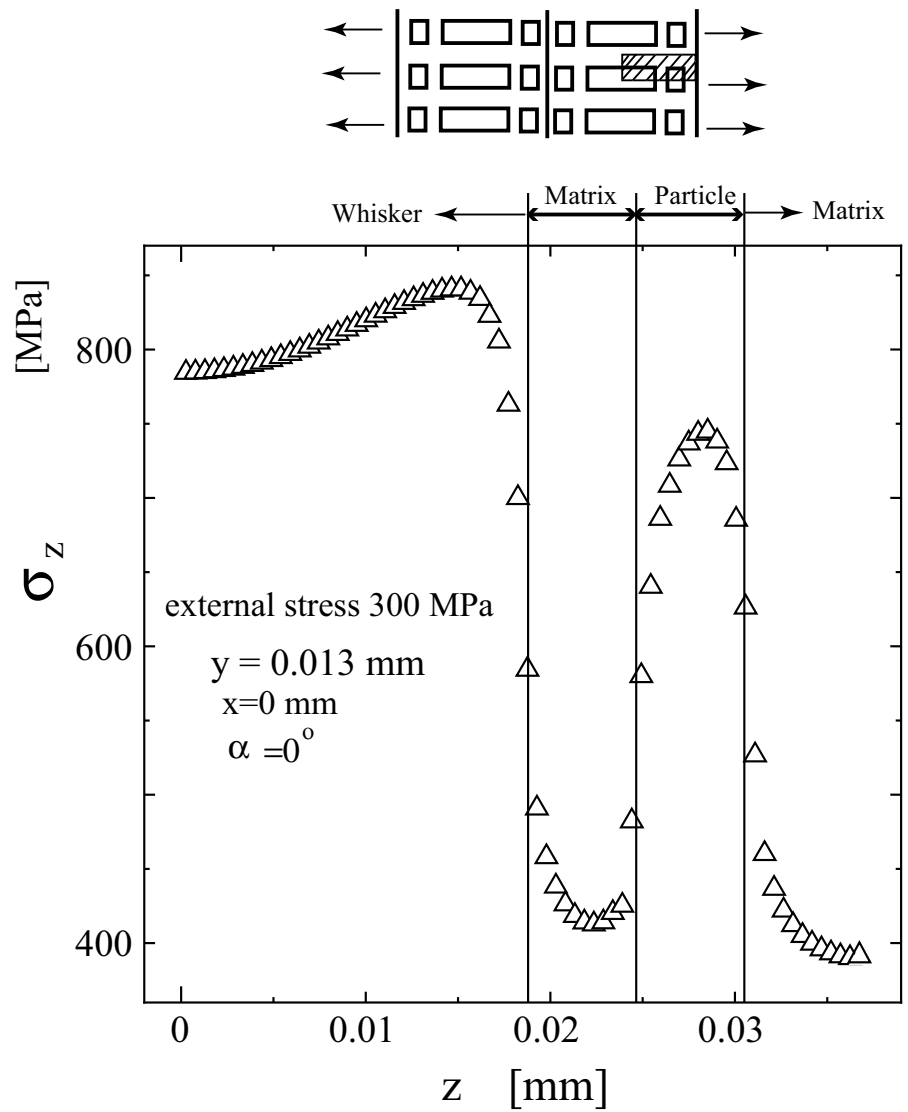


Fig.A7-5 Stress distribution along z direction for longitudinal loading (parallel to the stress direction).

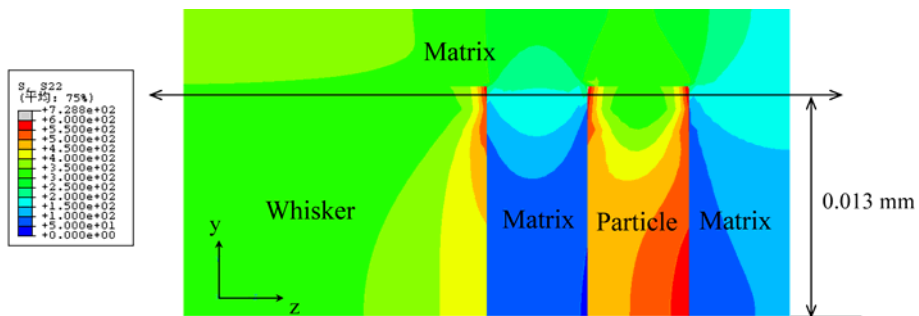
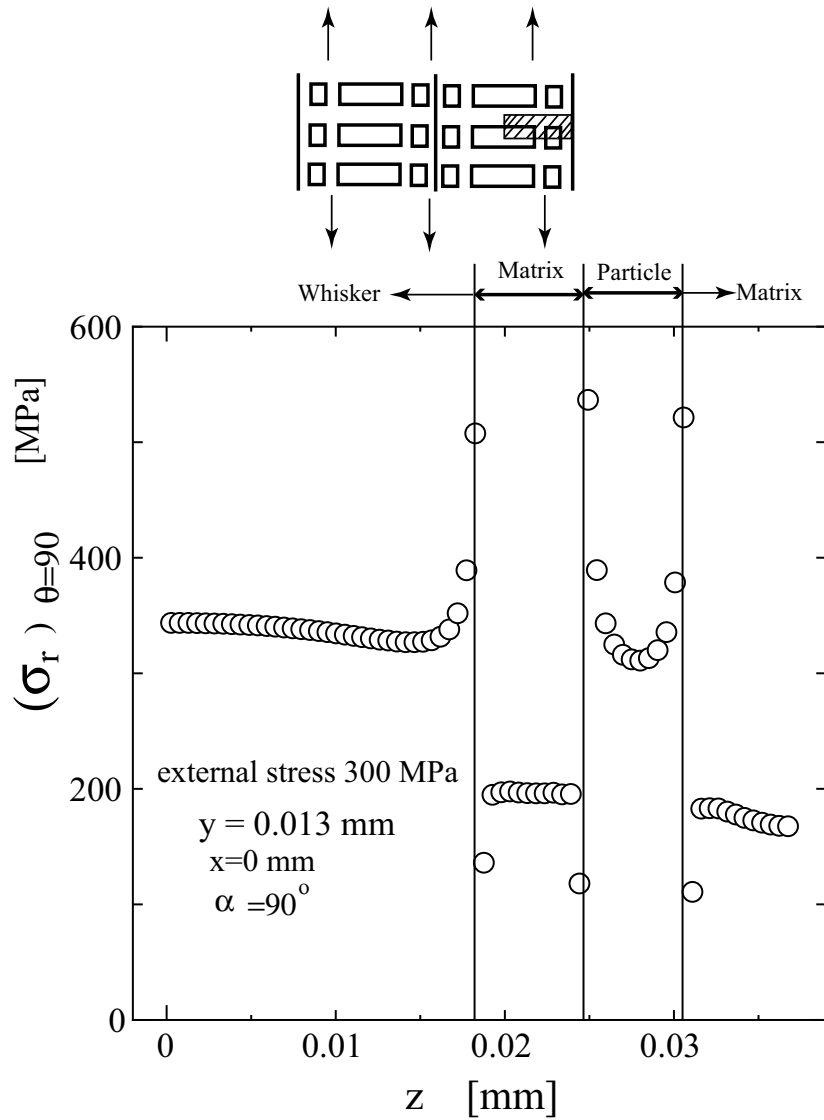


Fig.A7-6 Stress distribution along z direction for transverse loading (perpendicular to the stress direction).

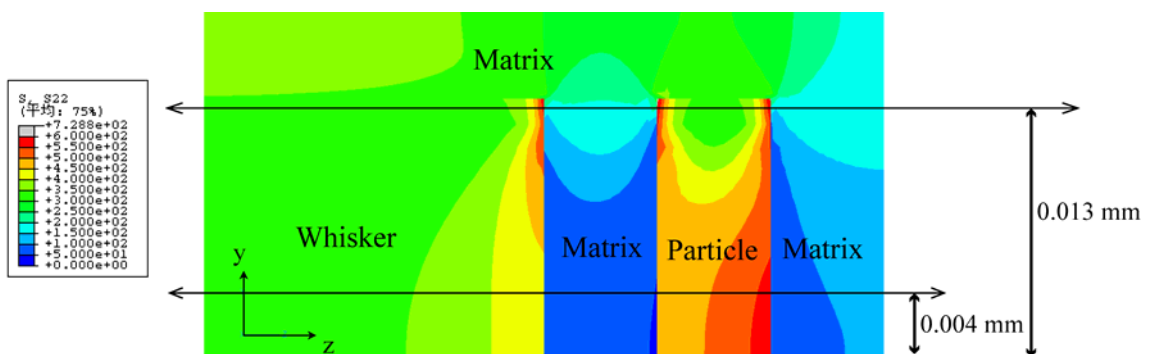
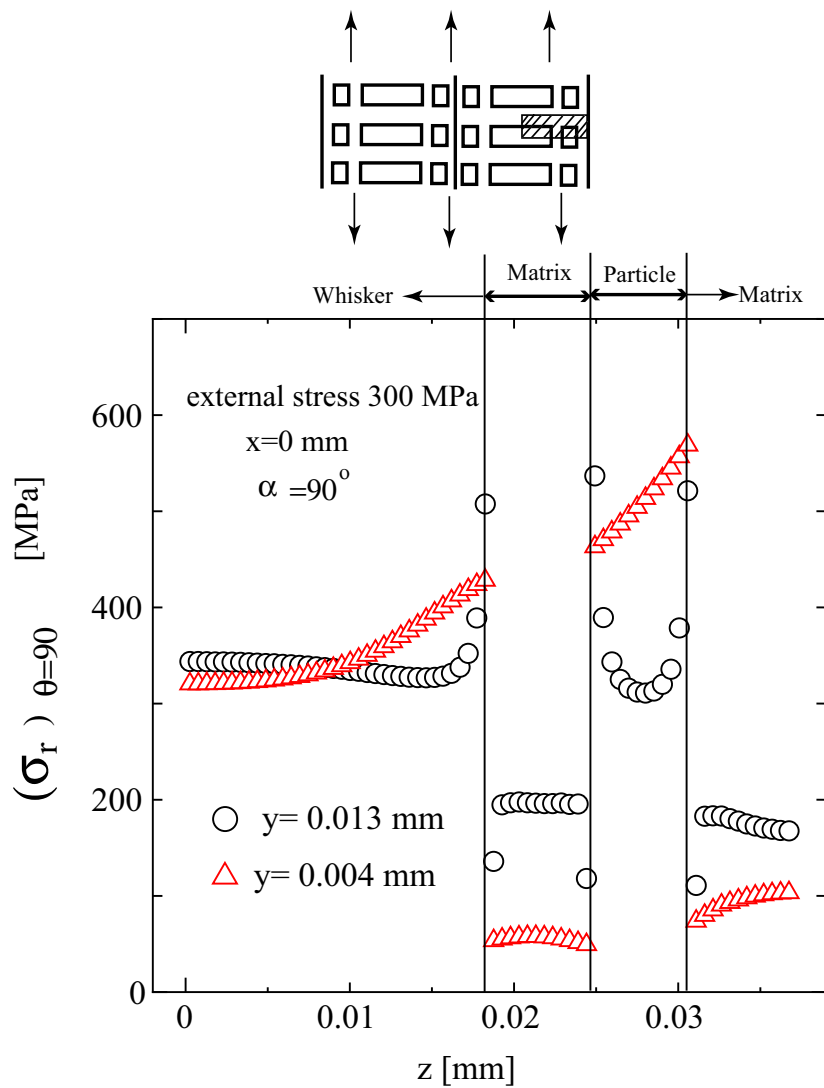


Fig.A7-7 Stress distribution along z direction for transverse loading (perpendicular to the stress direction).

References

- [1] S. L. Kumar, Y. Arai and E. Tsuchida: An analysis on singular fields around the interface edge of ceramic/ metal joints using moiré interferometry techniques. *JSME International Journal*, Vol. 48, No. 4 (2005), pp. 240-245
- [2] AL. Chen, Y. Arai and E. Tsuchida: A numerical study on effect of thermal cycling on monotonic and cyclic response of cast aluminum alloy-SiC particulate composites. *Theoretical Applied Mechanics*, Vol. 53 (2004), pp. 63-73
- [3] L. Llorca, A. Needleman and S. Suresh: An analysis of the effects of matrix void growth on deformation and ductility in metal-ceramic composites. *Acta. Metall. Mater.*, Vol. 39, No. 10 (1991), pp. 2317-2335.
- [4] T. Christman, A. Needleman and S. Suresh: An experimental and numerical study of deformation in metal-ceramic composites. *Acta Materilia.*, Vol. 37, No. 11, pp. 3029-3050, 1989.